IntechOpen

Lubrication

Tribology, Lubricants and Additives

Edited by David W. Johnson

LUBRICATION - TRIBOLOGY, LUBRICANTS AND ADDITIVES

Edited by **David W. Johnson**

Lubrication - Tribology, Lubricants and Additives
http://dx.doi.org/10.5772/intechopen.69833
Edited by David W. Johnson

Contributors

Yanguo Yin, Guotao Zhang, Erween Abd Rahim, Amiril Sahab Abdul Sani, Norfazillah Talib, Majid Soleimani, Leila Dehabadi, Lee Wilson, Lope G. Tabil, Mei Wang, Shojiro Miyake, Eurico Felix Pieretti, Andrea Cecilia Dorion Rodas, Renato Antunes, Maurício David Martins Neves, Jun H. Zhong, Dong Jiang, Ming Hu, Xiaoming Gao, Desheng Wang, Yanlong Fu, Jiayi Sun, Lijun Weng

Notice

First published in London, United Kingdom, 2018 by IntechOpen
eBook (PDF) Published by IntechOpen, 2019
IntechOpen is the global imprint of INTECHOPEN LIMITED, registered in England and Wales, registration number: 11086078, The Shard, 25th floor, 32 London Bridge Street
London, SE19SG – United Kingdom
Printed in Croatia

British Library Cataloguing-in-Publication Data
A catalogue record for this book is available from the British Library

Additional hard and PDF copies can be obtained from orders@intechopen.com

Lubrication - Tribology, Lubricants and Additives
Edited by David W. Johnson

p. cm.

Print ISBN 978-1-78923-128-1

Online ISBN 978-1-78923-129-8

eBook (PDF) ISBN 978-1-83881-434-2

Meet the editor

David W. Johnson is an associate professor and chair of the Chemistry Department at the University of Dayton. He received his PhD degree in Chemistry at Illinois Institute of Technology in 1983 completing his research in inorganic and computational chemistry. He joined the Department of Faculty at the University of Dayton in 1984. After a sabbatical at the Air Force Research Laboratory, he shifted his research area to the chemistry of lubricants and lubrication focusing on the interactions of lubricants and additives with lubricated surfaces in aerospace and refrigeration applications. Much of his recent work has focused on possible breakdown mechanisms of phosphate esters in contact with bearing surfaces at high temperatures. He is an author of more than 25 papers in refereed journals along with several technical reports and book chapters.

Contents

Preface XI

Section 1 Lubricant and Additive Reactivity 1

Chapter 1 **Ab-Initio Modeling of Lubricant Reactions with a Metal Al (111) Surface 3**
Jun Zhong

Chapter 2 **Antioxidants Classification and Applications in Lubricants 23**
Majid Soleimani, Leila Dehabadi, Lee D. Wilson and Lope G. Tabil

Section 2 Lubrication of Materials 43

Chapter 3 **Tribological Interaction of Bio-Based Metalworking Fluids in Machining Process 45**
Erween Abd. Rahim, Amiril Sahab Abdul Sani and Norfazillah Talib

Chapter 4 **Evaluation of the Biotribological Behavior and Cytotoxicity of Laser-Textured ISO 5832-1 Stainless Steel for Use in Orthopedic Implants 65**
Eurico Felix Pieretti, Andrea Cecília Dorión Rodas, Renato Altobelli Antunes and Maurício David Martins das Neves

Chapter 5 **Surface Morphology and Tribological Properties of Nanoscale (Ti, Al, Si, C)N Multilayer Coatings Deposited by Reactive Magnetron Sputtering 77**
Mei Wang and Shojiro Miyake

Chapter 6 **Effects of Different Materials on the Tribological Performance of PVD TiN Films under Starved Lubrication Regime 101**
Dong Jiang, Xiaoming Gao, Ming Hu, Desheng Wang, Yanlong Fu, Jiayi Sun and Lijun Weng

Chapter 7 **Lubrication and Friction of Porous Oil Bearing Materials 113**
Yanguo Yin and Guotao Zhang

Preface

Lubrication is critical in any application where moving parts are involved. As problems faced by the world increase in complexity, lubrication increases in importance while the conditions while lubrication is required under more extreme conditions of speed, temperature, and stress. In addition, the materials to be lubricated have become more exotic and potentially reactive due to the increased stress and temperature requirements. In the near future, lubricants with different compositions will be necessary for various applications, including refrigeration due to the development of more environment-friendly refrigerants and aerospace due to the use of higher-performance alloys for bearings and machining to reduce hazardous waste generation, among others. The extreme conditions make the properties of both the lubricant base stock and the additives more important and have required the development of more exotic bearing materials, including composition, surface treatments, and processing techniques.

This book is divided into two sections: first, the chemistry of some lubricants and lubricant additives are examined. Typical lubricant base stocks do not have ideal lubricating properties for use in many applications, so a series of additives are formulated to improve these properties. The chapters include both experimental and theoretical approaches to the decomposition of the lubricants and additives. Second, the lubrication of a variety of different substances is investigated in order to optimize lubricant properties for certain applications. It has become more apparent that the environmental effects and human health effects of degraded lubricants and additives are also important. Some of these studies are directed toward the development of more environment-friendly materials and lubricants for important applications. This book covers some of the important research in the area of lubricants and lubrication.

David W. Johnson
University of Dayton
Dayton, Ohio, USA

Section 1

Lubricant and Additive Reactivity

Chapter 1

Ab-Initio Modeling of Lubricant Reactions with a Metal Al (111) Surface

Jun Zhong

Additional information is available at the end of the chapter

http://dx.doi.org/10.5772/intechopen.72512

Abstract

In this chapter, to assist the design of aluminum processing, density functional theory is utilized to depict optimal adsorption geometries on an Al (111) surface for two commonly used boundary-layer lubricant additives: vinyl-phosphonic and acetic acids, i.e., tri-bridged, bi-bridged, and uni-dentate coordinations of these adsorbates are examined to determine the optimal binding sites on the surface. During these static analyses, charge density of states for molecular oxygen ions reacting with Al ions in the surface is applied to revealing the evolution essentials of molecular binding strength on surface. In addition, ab-initio molecular dynamics based upon density functional theory is employed to probe dynamic decomposition pathways on the Al (111) surface for two other important boundary-layer lubricant additives: butanoic acid and butanol alcohol. These decomposition pathways may occur upon molecular collisions with the surface, leading to formation of molecular pieces adhering on surface. Simulations are found to be in qualitative accord with existing experimental observations.

Keywords: density functional theory, ab-initio molecular dynamics, vinyl-phosphonic acid, acetic acid, butanoic acid, butanol alcohol, Al (111) surface

1. Introduction

Lubricant formulations used to control friction and wear in metallic forming processes typically contain mixtures of molecular additives in the base oil. Common lubricant additives in the metal-rolling processes consist of one or more aliphatic alcohols, acids or esters such as vinyl-phosphonic acid, acetic acid, butanoic acid and butanol alcohol etc. which have hydroxyl (OH) or carboxyl (O═C─OH) functional group [named oxygen-rich base (O-base)] to behave like a cationic anchor with electron-rich charges [1–3]. Initially, these molecules are

thought to anchor onto metal (e.g., hydroxide-alumina) surfaces through their O-bases. And then, such O-bases are believed to decompose on fresh (pure aluminum) surfaces occurring in the actual rolling work. As a result, these adsorbed and decomposed molecular pieces will contribute to the boundary thin-film lubrication and protection, i.e., their residual fragments (e.g., molecular chain tails) adhered on fresh surfaces with several molecular layers thick may serve as corrosion inhibitors of surface.

For adsorbate examples, **Figure 1** shows an illustration of two molecular structures: a vinyl-phosphonic acid [VPA, $H_3C_2P(O)(OH)_2$] with a tri-podal O-base [2(OH)─P═O] plus a vinyl-hydrocarbon tail [4] as shown in **Figure 1(a)**, and an acetic acid [EA, $H_3C_2(O)(OH)$] with an alkyl-chain plus a bi-podal O-base [O═C─OH] as shown in **Figure 1(b)**.

In **Figure 1(a)**, a study of the inelastic tunneling spectroscopy (IETS) for a VPA adsorption on a hydroxide-Al_2O_3 (0001) surface implied that the vinyl-tail on VPA did not participate in bonding to the oxide surface [5], but left itself accessible to react with other general lubricant molecules, which may serve as a molecular cap on the surface to inhibit migrations of corrosive species into the oxide surface. This reaction usually resulted in a tri-dentate coordination for the VPA on surface through a tri-podal O-base even if such a tri-dentate coordination was not unique on surface [6]. Crowell et al. utilized the electron energy loss spectroscopy (EELS) to observe an EA adsorption on an Al (111) surface starting at a very low temperature of 120 K [7]. They observed that a symmetrically bi-bridged geometry of main piece decomposed from the EA was more likely to bond to the surface than other configurations. In brief, both of above studies found that O-bases on acid molecules may usually bond to aluminum/alumina surfaces and oxidize them prior to other twigs, and then had molecular residual fragments (molecular chain tails) form thin-film inhibitors on the surfaces.

In addition, Underhill and Timsit [8] applied the X-ray photoelectron spectroscopy (XPS) to the study of dynamic decomposition pathways for 1-butanol and propanoic acid through molecular collisions with a clean Al (111) surface. At room temperature (e.g., 300 K), their results suggested that acid molecules break up on the surface, leading to attachments of aliphatic chains via their O-bases on surface. Alternatively, aliphatic alcohols were found to react with Al ions in the surface via their O-bases alone. At elevated temperatures (about 400 K), both acid and alcohol were found to dissociate on the clean surface, leading to attachments of aliphatic chains via their end C ions and pieces of decomposed O-base on surface, to form molecular boundary thin-films of surface. However, such the dynamic decomposition has received minimal attention in the literature.

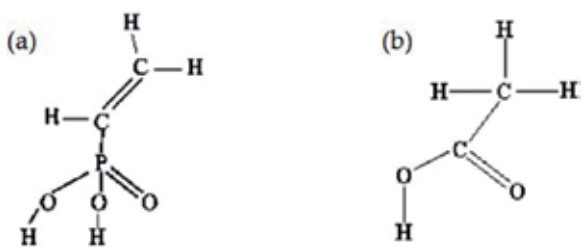

Figure 1. Two acid molecules: (a) a VPA molecule; (b) an EA molecule.

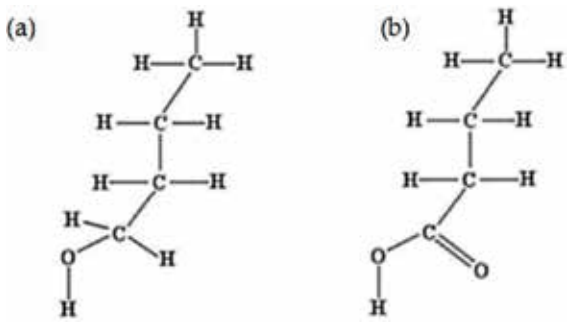

Figure 2. Schematics of (a) a butanol molecule; (b) a butanoic molecule.

In **Figure 2**, two lubricant additives, butanol alcohol [$H_3C{-}(CH_2)_2{-}H_2C{-}(OH)$] and butanoic acid [$H_3C{-}(CH_2)_2{-}C(O)(OH)$], are shown schematically: the alcohol in **Figure 2(a)** has a C—OH functional group; while the acid in **Figure 2(b)** has an O═C—OH functional group which is very similar to the EA as shown in **Figure 1(b)**.

In this chapter, we carry out series of density functional (DFT) analyses on how two commonly used boundary-layer lubricant additives, VPA and EA, bond statically to a clean (pure) Al (111) surface in their optimal geometries. During the actual rolling (forming) processes to hydroxide-alumina surfaces, since top textures (layers) of the surfaces are usually peeled off so that fresh (pure) aluminum surfaces (below top layers) with nascent islands can be subsequently exposed in the air, without loss of generality, such the DFT static outputs may help powerfully determine the favorably bonding mechanisms of additives to the highly reactive islands on fresh surfaces, so as to make clear the formation of protective thin-film on alumina surfaces. Then next, we examine dynamic decomposition pathways on the clean Al (111) surface using ab-initio molecular dynamics (AIMD) for two other important aliphatic boundary-layer lubricant additives: butanol alcohol and butanoic acid, to determine their thermal mechanisms of monolayer formation on the surface. During the AIMD simulation, each molecule is orientated to collide with the clean surface through its reactive O-base. Initial approaching speeds of molecules toward the surface are taken from the actual Al-rolling process. Decomposition pieces of additive molecules on the Al (111) surface are explored in details throughout the whole simulation. Simulation outputs are qualitatively compared with experimental observations using the EELS and the XPS for similar molecules [7, 8], which may reveal some unknown decomposed configurations in a previous DFT static study [9].

2. Configurations of adsorbates and adsorbents

2.1. Adsorbate configurations

Figure 3 shows a side view of a VPA structure, along with isosurfaces of charge density with the electron (e^-) localization function (ELF) representing the probability of finding a second e^- with the same spin in the neighboring region of the first (reference) e^- within [0, 1]. In other

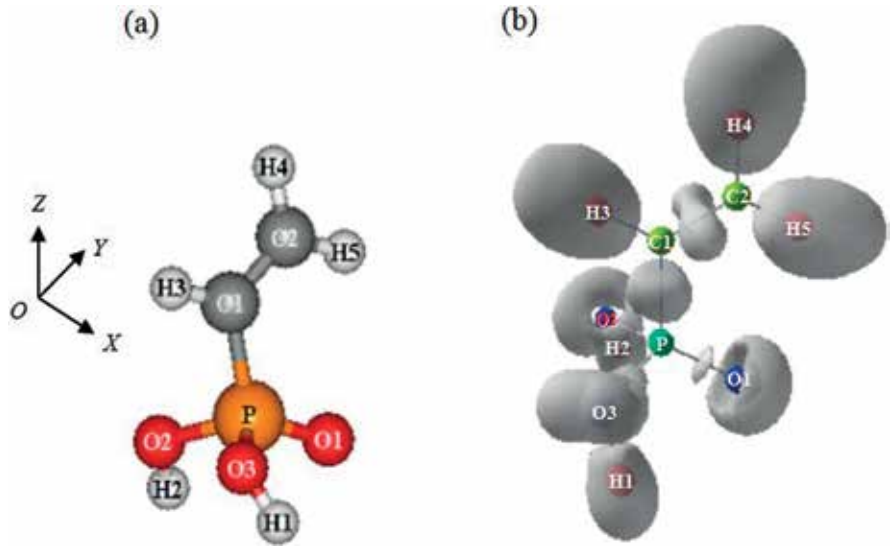

Figure 3. Side view of a VPA structure: (a) a vinyl-group and a tri-podal based P—O bonds on the VPA; (b) isosurfaces of charge density at the ELF = 0.81 for the VPA.

words, a high ELF value means a highly localized behavior for the first (reference) e^- [10–13]. According to this definition, high ELF values are typically associated with covalent bonds, e^- lone pairs, or inert cores [14]. In **Figure 3(b)**, ELF = 0.81 is the best visual difference of isosurfaces for each of atomic bonds according to comments in ref. [15]. The VASP (Vienna Ab-initio Simulation Package) calculations for the VPA indicated that two e^- lone pairs aggregated to O2 (and O3) nearby (a circle-lunar lobe) because of its *aniso-sp*^{3} hybrid bonding to H2 and P neighbors. However, O1 formed a weak double bond with P and had slightly more e^- lone pairs (a hemisphere lobe) than O2 and O3, see **Figure 5(a)**. In **Figure 3(a)**, such a VPA

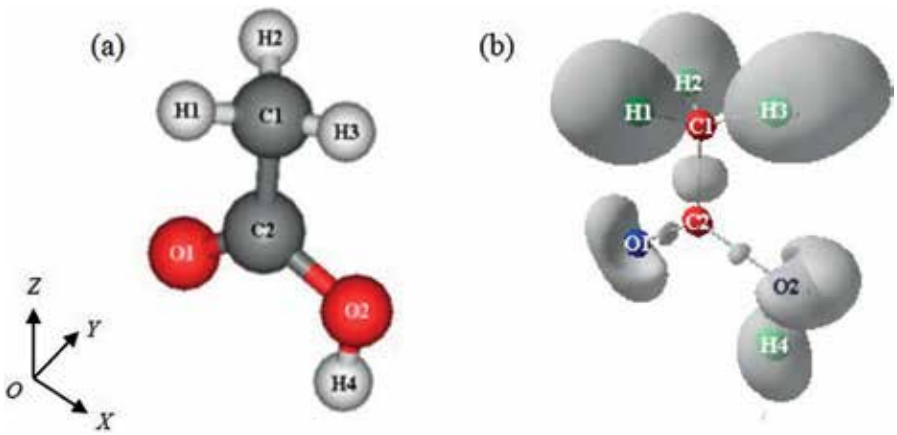

Figure 4. Side view of an EA structure: (a) a methyl group and a bi-podal-based C—O bonds on the EA; (b) isosurfaces of charge density at the ELF = 0.67 for the EA.

http://dx.doi.org/10.5772/intechopen.72512

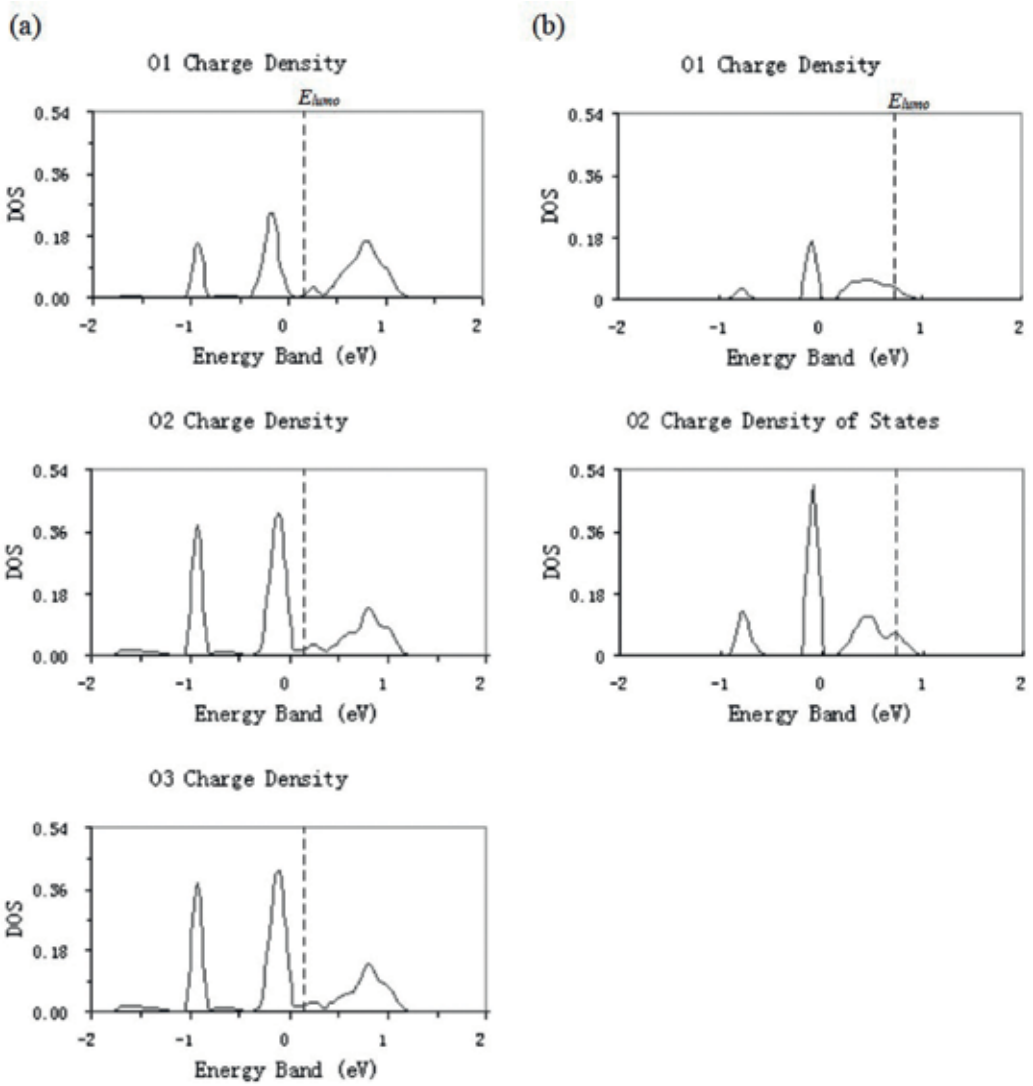

Figure 5. Charge density of states (DOS) for O ions on (a) the VPA and (b) the EA.

conformation was the most favorably energetic for the vinyl-group coplanar with the P═O1 double bond, and was consistent with that predicted in ref. [15]. Also, C1═C2 double bond showed an *aniso-sp*^{2} hybrid bonding type.

Figure 4 shows a side view of an EA structure, along with isosurfaces of charge density at the ELF = 0.67 to provide the best visual difference for each of atomic bonds. VASP analyses for the EA indicated that two e^- lone pairs aggregated to O2 nearby (a hemisphere lobe) because of its *aniso-sp*^{3} hybrid bonding to H4 and C2 neighbors. However, a strong C2═O1 double bond (an *aniso-sp*^{2} hybrid type) resulted in a lower charge density in e^- lone pairs around O1 (a cashew type) than around O2, see **Figure 5(b)**.

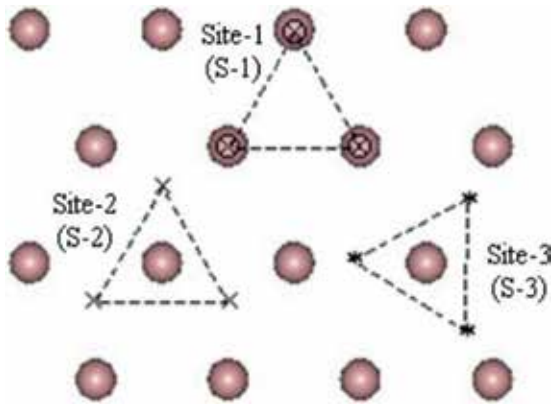

Figure 6. Three most favorable adsorption sites in top layer of Al (111) surface slab.

Figure 5 shows distributions of charge density of states (DOS) for three O ions on the VPA and two O ions on the EA, respectively. In **Figure 5**, the E_{lumo} represented the energy level corresponding to the lowest unoccupied molecular orbital, i.e., above the E_{lumo} the DOS for O ions represented unoccupied states. In **Figure 5**, more portions of the DOS for O ions on the VPA appeared in orbitals above the E_{lumo} than those on the EA, implying that VPA may be more reactive with the Al surface than EA by feat of their O ions.

2.2. Adsorbent configurations

Since Al (111) surface has the lowest surface energy among all surface geometries in aluminum bulk, it is likely to expose in the air during the actual rolling process. So here it is selected as an adsorption slab surface (adsorbent) to react with above adsorbates. **Figure 6** shows three distinguishable adsorption sites in the top layer of Al (111) surface slab. We refer to them as site-1, -2, and -3, respectively. Among these sites, site-1 (S-1) had corners at three Al ions; site-2 (S-2) had corners at three cave points (cross signs); and site-3 (S-3) had corners at three saddle points (ice-star signs). According to past experiences [14], these three sites were more likely to react with adsorbates than others because they allowed O-bases on adsorbates to bond to surface stronger than other ones.

3. Simulation methodologies and procedures

3.1. Static calculations

These calculations were based upon the DFT [16–18] using the Vienna Ab-initio Simulation Package (VASP). At first, all calculations were performed using the Projector-Augmented Wave (PAW) pseudopotentials [19]. The GGA created by Perdew and co-workers [20, 21] was employed for evaluating the exchange-correlation energy. This methodology was similar to a previous study of optimizing the VPA adsorption geometries on an α-Al_2O_3 (0001) surface

[15]. Prior to these calculations, lattice constant, bulk modulus and cohesive energy for a pure aluminum bulk by fitting data of energy versus volume to the Murnaghan Eq. [22] was calculated. A regular Monkhorst-Pack grid [23] of 17 × 17 × 17 was chosen as the best *k*-point sampling, so that the total energy of system was converged within 1–2 meV/atom. The computed lattice constant, a_0'= 4.05(3) Å, see ref. [9].

Then next, calculations of acid adsorptions on the Al (111) surface slab were conducted in a supercell with a periodic four-layer $3a_0$'× $3a_0$'units (16 Al ions per layer) in XY directions. A plane-wave cutoff energy, 400 eV, which was primarily required by the "hardest ions (C and O)", was chosen. A regular Monkhorst-Pack grid of a 5×5×1 *k*-point sampling was selected for this orthogonal supercell with three definite orientations: $a[1\bar{1}0] = 2\sqrt{2}a_0$' along the X axis, $b[11\bar{2}] = \sqrt{6}a_0$' along the Y axis, and *c* [111] = 26.0 Å along the Z axis, plus a vacuum distance of 10.0 Å in *c* direction and with one bottom layer of the Al (111) slab fixed along *c* direction in the supercell. The atomic geometry was optimized through minimizing the Hellman-Feyman forces using a conjugate gradient algorithm [11], until the total force on each ion reduced to 0.05 eV/Å or less.

3.2. Dynamic simulations

In this study, all ab-initio molecular dynamics (AIMD) simulations were also based upon the DFT as implemented in the VASP. A Vanderbilt-type ultrasoft pseudopotentials (USP) were utilized for elemental constituents by means of the GGA [24]. In real practice, the GGA usually yielded inaccurate reaction barriers [25–27], while a semilocal-BLYP and hybrid-B3LYP functionals seemed to predict adsorption energies accurately and distinguish adsorption sites correctly. However, for the study of dynamic decomposition, we believed that the GGA was also a reasonable compromise since a highly colliding velocity acting on molecules toward the Al surface slab would likely overwhelm any barrier to the decomposition.

During the AIMD simulation, first of all, lattice constant (a_0) of pure Al bulk was calculated using the NPT ensemble, which thermally equilibrated one $2a_0 \times 2a_0 \times 2a_0$ unit cell at a room temperature (300 K) plus an ambient pressure of 1.0 bar for about 1500 time steps, a simulation time step of 0.001 ps was selected. A regular gamma-centered grid of 5 × 5 × 5 was chosen as the best *k*-point sampling for the unit cell. Total energy of the system was converged within 1–2 meV/atom. A plane-wave cutoff energy, 400 eV, as dictated by the hardest oxygen pseudopotential, was adopted in all simulations. The computed lattice constant, a_0 = 4.05(7) Å, was favorably fitting to other calculations and experimental observations [28].

Besides, for modeling interactions between additive molecules and an Al (111) slab, a Monkhorst-Pack grid of 5 × 5 × 1 was selected for the best *k*-point sampling. A supercell with the entire Al (111) slab consisted of four Al layers (36 ions per layer) of 144 ions. This orthorhombic geometry had three definite orientations: $a[1\bar{1}0] = \frac{3}{2}\sqrt{6}a_0$ along the X axis, $b[11\bar{2}] = 3\sqrt{2}a_0$ along the Y axis, and *c* [111] = 40.0 Å along the Z axis plus a vacuum distance of 24.0 Å in the *c* direction to preclude interactions with periodic images. The bottom layer of the Al (111) slab was fixed along the *c* direction to prevent the whole slab motion during impacts of additive molecules onto the Al slab surface.

In addition, each of isolated molecules was optimized in a same vacuum supercell as used for the Al (111) slab. And then, it was equilibrated at 300 K for about 1500 time steps by re-scaling thermal velocities at each time step [29], the time step = 0.001 ps. Simultaneously, the Al (111) slab were equilibrated in its supercell by the same technique as each isolated molecule. Then next, each isolated molecule was transferred into the simulation supercell containing the Al (111) slab, respectively.

After thermal equilibration, all AIMD simulations for interactions between additive molecules and the Al (111) slab were carried out through a constant energy method (NVE) without controlling temperature of system [29]. In real processing works, when steel rollers converged to form bite regions in the metal rolling of Al alloys, pressure gradients in bite regions would draw lubricant additives into conjunction. At this time, translational speeds acting on a single molecule can be estimated to reach as high as 2500 m/s due to kinematics at the tool/Al interface [30]. Hence, a serial approaching velocities, $V_{d'}$ based upon this situation, were adopted in the AIMD simulations. Then next, each additive molecule started accelerating toward the Al (111) slab surface once it met a net attraction from the surface. To save computational cost, initial vertical spacing between each additive molecule and Al ions in the surface was set to 2.30 Å, which was slightly larger than Al—O bond length (1.86–1.97 Å) as indicated in ref. [31].

4. Results and discussions

4.1. Static calculations

To better understand adsorption mechanisms of VPA and EA on Al (111) surface, several combined adsorbate/slab systems were selected for the investigation. The adsorption enthalpy (the binding energy or the binding strength), $\Delta H_{ads}^{(m)}$, was defined as the difference between the total energy of the combined adsorbate plus slab (adsorbent), and the total energy of the separated adsorbate and, the separated slab, which was given by

$$\Delta H_{ads}^{(m)} = E(\text{adsorbate \& slab}) - [E(\text{adsorbate}) + E(\text{slab})] \quad (1)$$

where the superscript (m) indicated one reaction type. A negative $\Delta H_{ads}^{(m)}$ value corresponded to a favorable adsorption on surface, while a positive one represented an unlikely reaction on surface.

Preliminary investigation of the VPA adsorption on Al (111) surface indicated that, its standing geometries at S-2 and S-3 always shifted to S-1 on the surface when using the energy minimization. Similar results can be obtained for the EA adsorption at S-2 and S-3 on Al (111) surface. Therefore, S-1 was regarded as the most favorable adsorption site for these adsorbates. According to this, we would only focus on the S-1 for the VPA and the EA adsorptions on Al (111) surface.

4.1.1. Uni-dentate configurations

Figure 7 shows side views of VPA and EA adsorptions on Al(111) surface in their own uni-dentate coordination with one of their oxygen ions and one H ion (dissociated from this oxygen ion) bonding onto the surface, respectively. Molecular binding sites on the surface were both at S-1.

In **Figure 7**, Al—H and Al—O single bonds were formed on Al (111) surface to sustain the adsorbates. Adsorption enthalpies corresponding to **Figure 7(a)**, **(b)**, $\Delta H_{ads}^{(VPS,EA)}$ = −0.89 and −0.51 eV, respectively. Moreover, VASP calculations indicated that each of adsorption enthalpies would bring additional negative values: −0.26 eV, due to subsequent formation of gaseous H_2 molecule by means of H ions desorbed from Al (111) surface. Therefore, if ignoring zero point energy corrections, the formation of gaseous H_2 molecule in these final adsorptions were more favorable to those individual H ions adsorbing onto the surface, so molecular main pieces would be left onto the surface alone in adsorption end, see **Figure 8**.

Figure 8 shows isosurfaces of charge density for vinyl-phosphonate and acetate on Al (111) surface in their own uni-dentate coordination, respectively. A value of the ELF = 0.67 was chosen because it may provide the best visual difference in charge density on C—O and P—O bonds. In **Figure 8(b)**, a small lobe can be observed on C2—O2 bond, while P—O3 bond in **Figure 8(a)** had no such a character. This meant that O_2 ion on C2—O2 bond was more covalent, while O3 ion on P—O3 bond was more ionic. This was expected because P was less electronegative than C (2.1 vs. 2.5), see ref. [32]. Therefore, during these two adsorptions, portions of charge density for O3 on vinyl-phosphonate in **Figure 8(a)** would move more toward the reacting Al ion in surface than that for O2 on acetate in **Figure 8(b)**. Qualitatively, this may occur reasonably because more unoccupied e^- states for O3 than those for O2 seemed to make the final binding state of VPA stabler than that of EA on the surface.

Quantitatively, **Figure 9(a)** shows the modified charge density of states (DOS) for O3 on vinyl-phosphonate as shown in **Figure 8(a)**, corresponding to e^- states (around the E_{lumo}) in **Figure 5(a)**. Comparing this DOS with that in **Figure 5(a)** for O3 on VPA, it may find that many of unoccupied e^- states evolved into occupied ones (below the E_F, the Fermi level on energy band) after VPA adsorption on surface. Similarly, **Figure 9(b)** shows the modified DOS for O2 on acetate as shown in **Figure 8(b)**, corresponding to e^- states (around the E_{lumo}) in **Figure 5(b)**. Comparing O3 on VPA with O2 on EA, we concluded that the DOS for O3 would shift more below the E_F than that for O2 after molecular adsorptions, which made the binding energy of VPA larger than that of EA.

In the following subsections, similar trends of the DOS curves in **Figure 9** can also be observed for O ions on molecular main piece reacting with Al (111) surface in bi-bridged (VPA and EA) and tri-bridged (VPA) coordinations. According to these results, we believed that the VPA should bind stronger than the equivalent EA on Al (111) surface because of its larger number of unoccupied e^- states available for bonding to the surface.

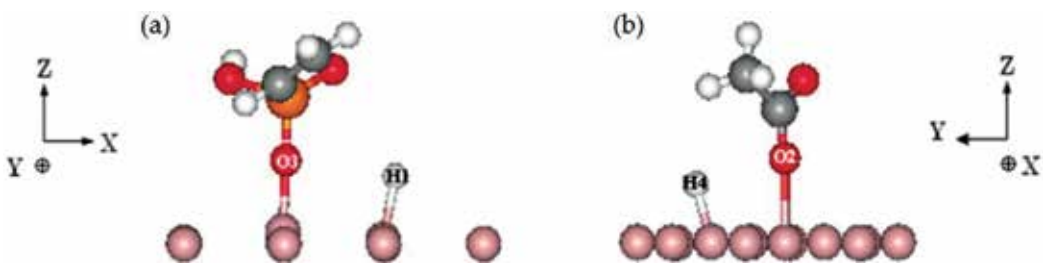

Figure 7. Side views of (a) VPA and (b) EA adsorptions on Al (111) surface in uni-dentate coordination.

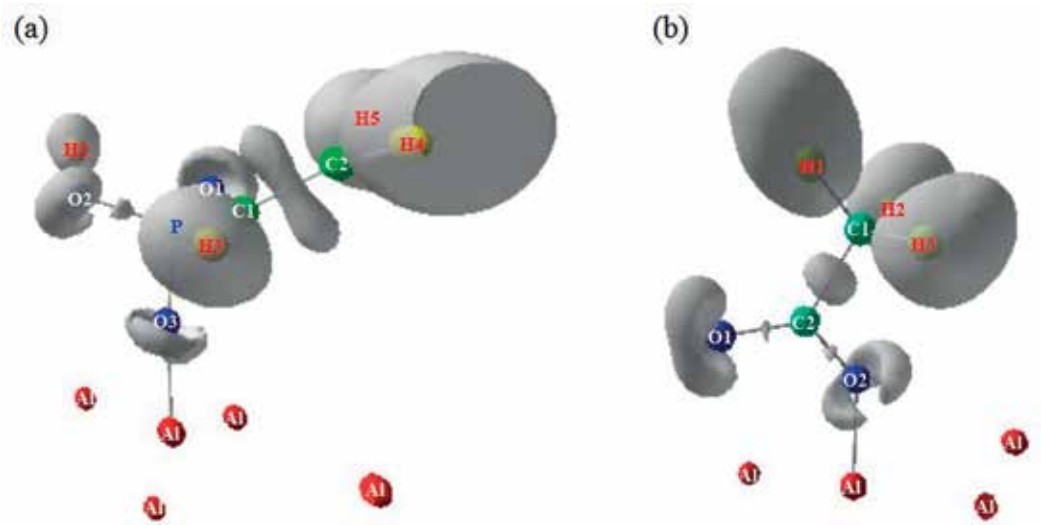

Figure 8. Isosurfaces of charge density at the ELF = 0.67 for (a) VPA and for (b) EA adsorptions on Al (111) surface in their own uni-dentate coordination.

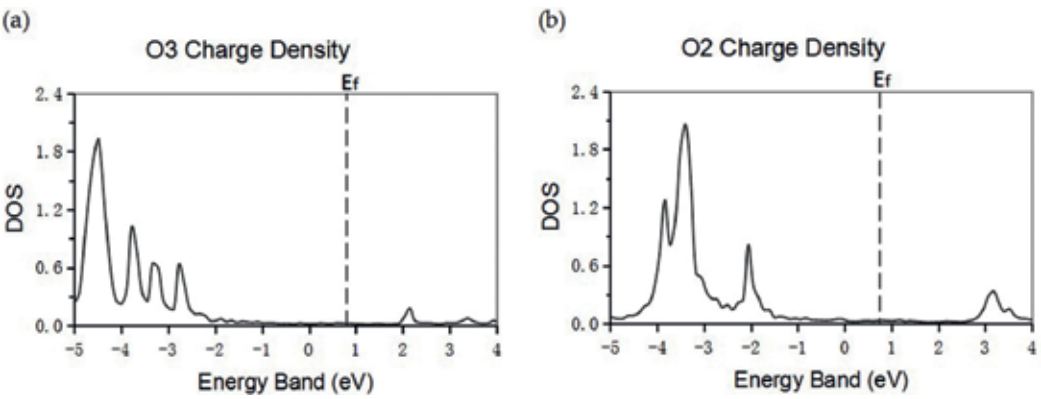

Figure 9. The modified DOS for (a) O3 ion on vinyl-phosphonate and (b) O2 ion on acetate.

4.1.2. Bi-bridged configurations

Figure 10 shows side views of vinyl-phosphonate and acetate adsorptions on Al (111) surface in their own bi-bridged coordination, respectively, with H ions liberating from molecular main piece and bonding to the surface. In these two adsorptions, adsorption enthalpies corresponding to **Figure 10(a)**, **(b)**, $\Delta H_{ads}^{(VPA,EA)} = -1.32$ and -1.52 eV, respectively. Moreover, subsequent formation of gaseous H_2 molecule by means of H ions desorbed from Al (111) surface would bring additional negative values for these enthalpies: −0.51 and −0.26 eV, respectively, indicating that both vinyl-phosphonate and acetate bonding to Al (111) surface alone in their own bi-bridged coordination, respectively, would be more favorable in final adsorptions.

http://dx.doi.org/10.5772/intechopen.72512

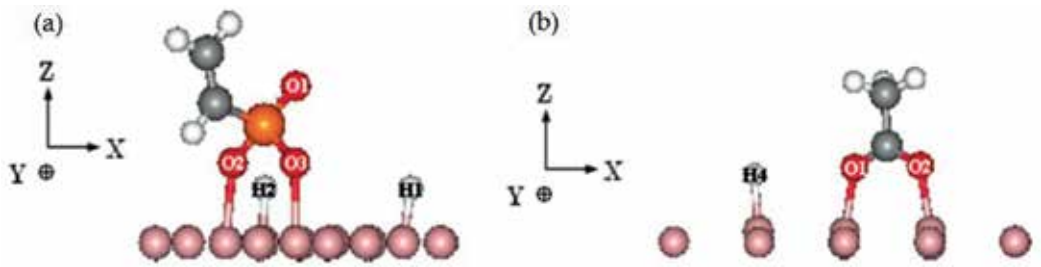

Figure 10. Side views of (a) vinyl-phosphonate and (b) acetate adsorptions on Al (111) surface in bi-bridged coordination, respectively.

4.1.3. Tri-bridged configurations

Figure 11 shows a side view of VPA adsorption on Al (111) surface in tri-bridged coordination. In **Figure 11**, 2 H ions liberated from the VPA main piece through the condensing reaction and were adsorbed on the surface. Adsorption enthalpy corresponding to **Figure 11**, $\Delta H_{ads}^{(VPA)} = -2.61$ eV. Moreover, subsequent formation of gaseous H_2 molecule by means of H ions desorbed from Al (111) surface would bring additional negative values for this enthalpy: −0.51 eV, indicating that vinyl-phosphonate bonding to Al (111) surface alone in its own tri-bridged coordination, would be more favorable in final adsorption.

4.1.4. Other adsorption geometries

When rotating initial configurations of adsorbates by some clockwise angels (e.g., 120° or 180° etc) toward Al (111) surface rather than their functional groups facing the surface, i.e., with the CH_3 end directly pointing toward the surface, the binding energies of adsorbates on the surface would indicate positive values, meaning that such kinds of reacting geometries were unfavorable in the adsorption.

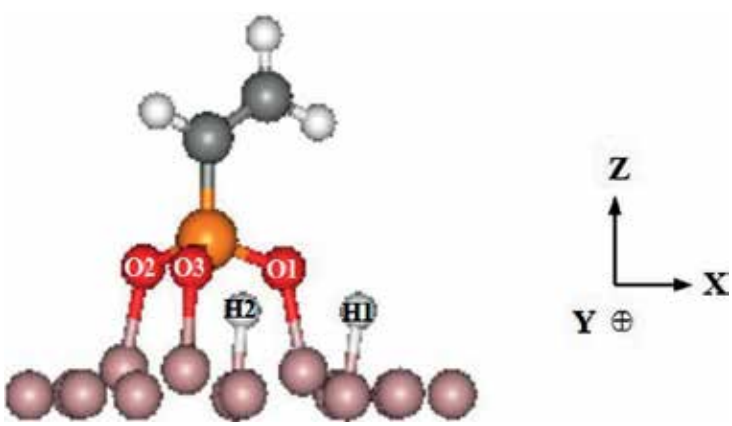

Figure 11. A side view of vinyl-phosphonate adsorption on Al (111) surface in tri-bridged coordination.

4.1.5. Conclusions

In summary, if ignoring entropy contributions, for the VPA, the best favorable adsorption geometries on Al (111) surface were in the order: tri-bridged coordination > bi-bridged coordination > uni-dentate coordination. While for the EA, the best adsorption geometries on Al (111) surface were in the order: bi-bridged coordination > uni-dentate coordination.

In addition, comparing these two adsorption types, in each of above adsorption geometries, the binding state of VPA on Al (111) surface was always stronger than that of equivalent EA on the surface. The main reason could be due to a more highly reactive 2(O)─P═O functional group with the surface than an O─C═O functional one. H ions liberating from molecular main pieces and adsorbing onto the surface, also influenced all of the binding states in above. However, the formation of gaseous H_2 molecules by means of H ions desorbed from the surface was more favorable in adsorption ends.

4.2. Dynamic simulations

In this section, dynamic decomposition pathways for two selected aliphatic boundary-layer lubricant additives: butanoic acid and butanol alcohol on Al (111) surface, are discussed using ab-initio molecular dynamics.

Corresponding to **Figure 2**, **Figure 12** shows isosurfaces of charge density at the ELF = 0.93 for these two molecules. In **Figure 12(a)**, O2 had two e^- lone pairs (a circular-lunar lobe) because of its *aniso-sp*^{3} hybrid bonding to C and H neighbors; O1 formed a strong double bond with C, leading to lower charge density (a semi-lunar lobe) than around O2; Both O1 and O2 behaved more reactive with the clean Al (111) surface than other ions on butanoic acid, which were very similar to those in **Figure 4(b)**. In **Figure 12(b)**, O2 also had two e^- lone pairs (a circular-lunar lobe) because of its *aniso-sp*^{3} hybrid bonding to C and H neighbors; O2 showed more reactive with the clean Al (111) surface than other ions on butanol alcohol. In a word, the ELF analyses indicated that functional groups O═C─OH and C─OH on these two molecules were electron-rich, and hence were more likely to react with the Al surface than other C─H and C─C twigs.

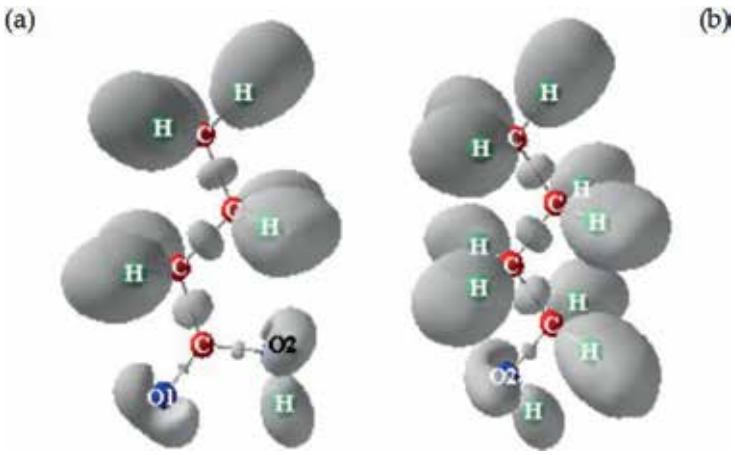

Figure 12. Side views of isosurfaces of charge density at the ELF = 0.67 for (a) butanoic acid and for (b) butanol alcohol.

Figure 13 shows initial geometries of butanoic acid and butanol alcohol interactions with Al (111) surface slab in four models. In each model, an additive molecule was positioned with its carbon backbone directly above the center of the equilibrated Al (111) surface, molecular orientations along [111] direction were shown in **Figure 13(a)–(d)**, respectively. In **Figure 13**, the first three models were for butanoic acid reactions with Al (111) slab surface: In model-1 (M−1), V_d = −15.0 Å/ps (1500 m/s) and the O ion on O═C bond was set at one 2.30 Å spacing above the Al (111) slab surface. In model-2 (M−2), V_d = −15.0 Å/ps and the OH group was positioned at one 2.30 Å spacing above the Al (111) slab surface. In model-3 (M−3), V_d = −20.0 Å/ps and all components in O═C─OH functional group were positioned directly at one 2.30 Å spacing above the Al (111) slab surface. The last model was for butanol alcohol reaction with the Al (111) slab: In model-4 (M−4), V_d = −20.0 Å/ps and the OH group was positioned at one 2.30 Å spacing above the Al (111) slab surface.

4.2.1. Dynamic decomposition pathways for butanoic acid on Al (111) slab surface

Figure 14 shows decomposition pathways for M−1, M−2 and M−3 models starting at 300 K. In **Figure 14(a)** for the M−1, at 50 simulation time steps, the O ion in O═C group on butanoic acid molecule began anchoring to the surface in a bi-dentate coordination. However, the OH group did not appear to interact with the surface at this time. At 90 time steps, the O ion in O═C group had dissociated from molecular main piece and was adsorbed onto the surface, with the residual molecular main piece anchoring to the surface through its alkyl-chain. At 200 time steps, the OH group had dissociated from molecular main piece and began interacting with the surface through its O ion. At 310 time steps, the OH group fully dissociated and was adsorbed onto the surface in a uni-dentate coordination. The residual alkyl-chain finally anchored to the surface in a tetra-coordination via its carboxyl C ion, with the O ion (dissociated from the O═C group) adsorbing on the surface in tri-dentate coordination. Note that the temperature of this system increased from 300 to 970 K throughout the whole simulation.

In **Figure 14(b)** for the M−2, at 40 time steps, the OH group interacted with Al (111) surface, resulting in dissociation of one H ion from molecular main piece. Main piece of butanoic acid interacted with the surface in a bi-bridged coordination through its O ions. At 130 time steps,

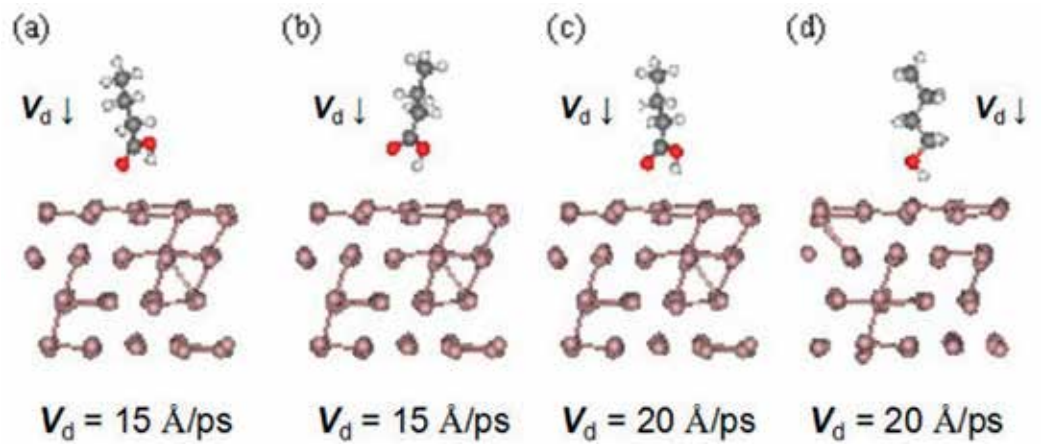

Figure 13. Four initial geometries of butanoic acid and butanol alcohol interactions with Al (111) slab: (a) M−1; (b) M−2; (c) M−3; (d) M−4.

this main piece remained anchoring to the surface. However at 200 time steps, this coordination was becoming uni-dentate as the main piece rebounded the surface under its consistent collisions, and with an Al ion pulled upward by one of O ions in it. At 310 time steps, the fragment in a bi-dentate configuration resembled a soap, i.e., a product of "R—COOM (here "R— "represented the alkyl-chain and "M" was a metal ion in the surface)" was formed in simulation [33]. Soap formation with fatty acids had been observed in the Al forming process where nominal pressures were in the vicinity of 2.5 times the material flow strength [3, 34]. The temperature of this system increased from 300 to 960 K throughout the whole simulation.

In **Figure 14(c)** for the M–3, at 60 time steps, the O ion in O═C group had dissociated and was subsequently adsorbed in a tri-dentate configuration on Al (111) surface. The same was true for the OH group. The residual alkyl-chain formed bi-dentate and tri-dentate configurations in the order at 100, 150, and 310 time steps throughout the whole simulation. One H ion dissociated from the adsorbed OH group and migrated about the surface. The temperature of this system increased from 300 to 1330 K throughout the whole simulation.

Figure 15 shows the initial evolution of potential energy computed for each of three models in **Figure 14**. In each case, butanoic acid molecule usually began interacting with the surface within 30–50 time steps. The potential energy of each system increased during this time interval so as to overcome the barrier to the adsorption. This energy then decreased as the surface defused molecular consistent impacts and decomposition. Beyond the dip point, the energy increased once again as molecular fragment and its decomposed components in functional

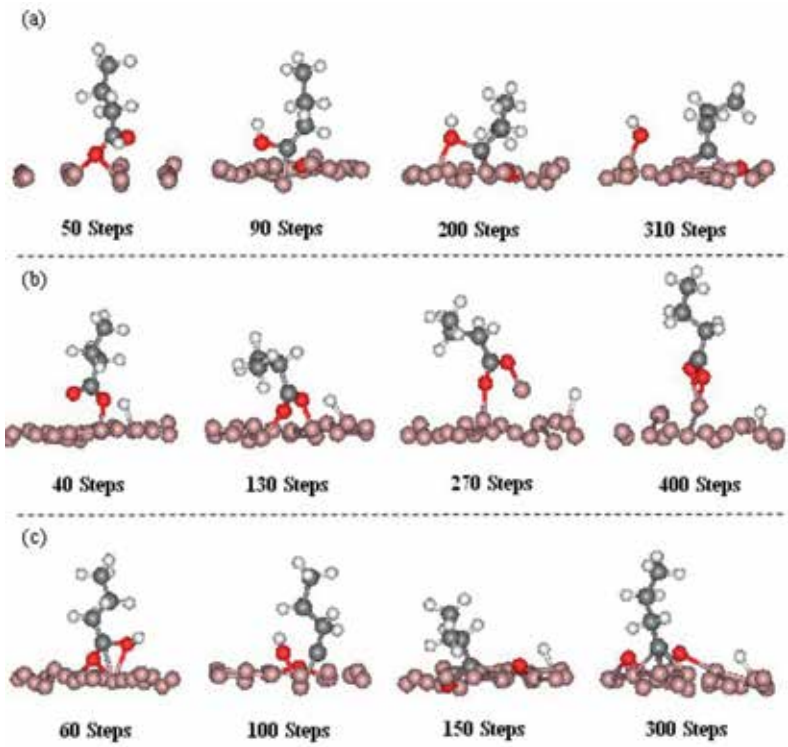

Figure 14. Three models of decomposition pathways starting at 300 K: (a) M–1; (b) M–2 and (c) M–3.

http://dx.doi.org/10.5772/intechopen.72512

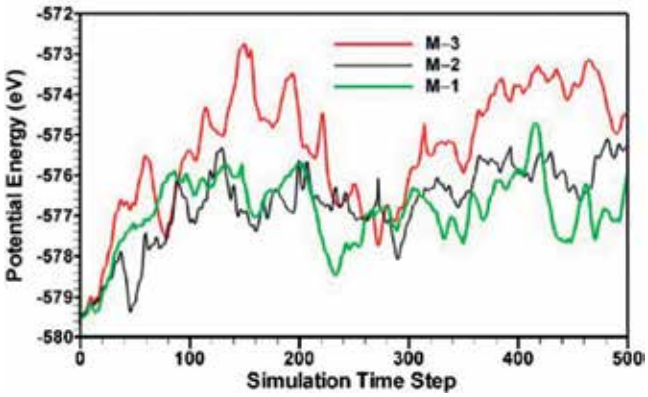

Figure 15. Potential energies of M−1, M−2 and M−3 vs. time steps for butanoic acid decomposition on Al (111) surface.

group re-arranged themselves on the surface. The sharp peaks on M−1 and M−3 curves indicated larger and more rapid exchanges between potential and kinetic energies than were observed in M−2 during the decomposition.

Figure 16 shows potential energies of three models during the first 350 time steps of thermal annealing after their distributions of 500 time steps as shown in **Figure 15**. In **Figure 15**, over this 350 time steps, each curve decreased and ultimately approached an asymptotic value after about 250 time steps. After 350 time steps, the potential energy of M−3 was slightly lower than M−1, but M−2 still had the highest energy level. In addition, our DFT energy minimization found that M−3 was the most stable configuration followed by M−1 and M−2.

4.2.2. Dynamic decomposition pathways for butanol alcohol on Al (111) surface

Figure 17 shows dynamic decomposition pathways for butanol alcohol on Al (111) surface, M–4, starting at 300 K. In **Figure 17**, at 40 time steps, 1 H ion dissociated from the OH group and interacted with an Al ion in the surface. At 100 time steps, molecular fragment was adsorbed on the surface plus a lone H ion moved below the surface. At 250 time steps, molecular fragment

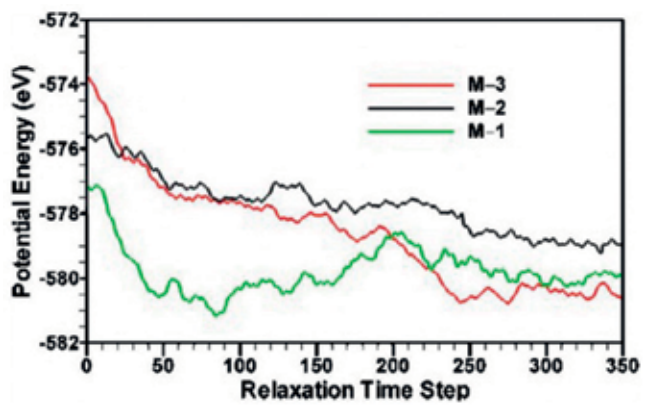

Figure 16. An effect of further annealing at 500 K on potential energies of M−1, M−2 and M−3 for butanoic acid decomposition on Al (111) surface.

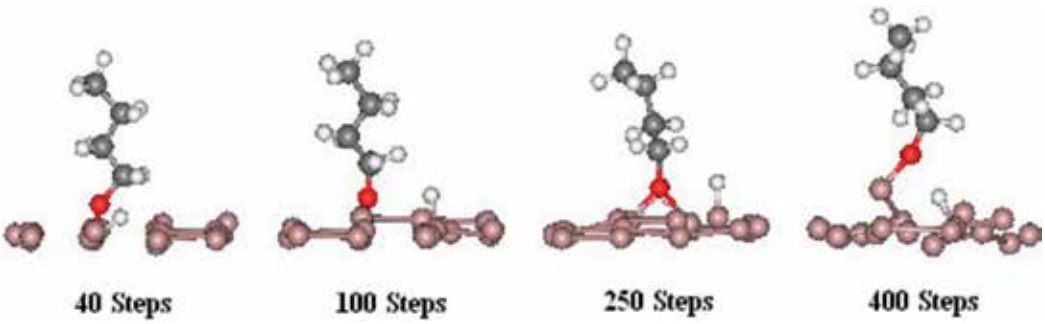

Figure 17. Dynamic decomposition pathways for M–4 starting at 300 K.

evolved its adsorption geometry to a bi-dentate configuration. At 400 time steps, molecular fragment showed up a uni-dentate configuration. Interestingly, during this decomposition, neither bi-dentate nor tri-dentate configuration depicted in above decomposed pieces of butanoic acid were observed in butanol alcohol configurations. Additional AIMD simulations for a butanol alcohol molecule slightly rotated relative to the Al (111) slab also confirmed this observation, see discussions in Section 4.2.3. According to this, we concluded that the decomposition pathway for butanol alcohol just occurred to oxidize the surface by means of its dissociated OH group to form an alcoholate on the surface if other additives were not involved in this reaction.

Figure 18 shows the distribution of potential energy for M–4 starting at 300 K. Here a sharp peak around 40 time steps represented the dissociation of an H ion from molecular main piece. The dip in the curve near 220 time steps was due to the re-arrangement of the decomposed pieces on the surface.

4.2.3. Other decomposition pathways

Other several AIMD simulations were carried out on decomposition pathways with above additive molecules rotating their initial configurations by 180° clockwise (group-1) and 90° counterclockwise (group-2) toward Al (111) surface rather than their functional groups

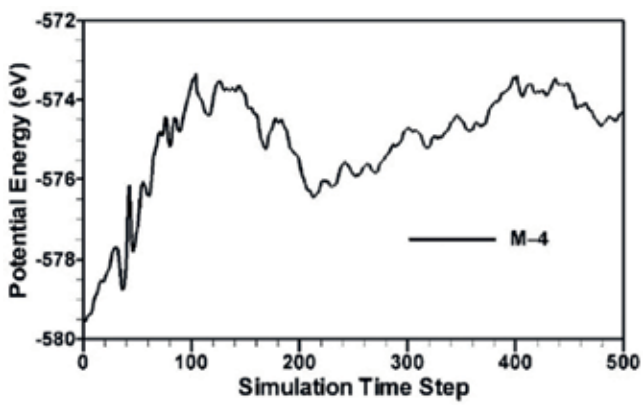

Figure 18. Distribution of potential energy vs. time steps for M–4 starting at 300 K.

facing the surface, respectively. For group-1 with the CH_3 end pointing toward the surface, it initially bounced off the surface without decomposing, but intermediately rotated its functional groups toward the surface when it bounced back the surface. And then, it carried on decomposition pathways discussed in above Sections. For group-2 with the carbon backbones aligning with the surface, it initially bounced off the surface without decomposing, but immediately rotated its functional groups toward the surface when it bounced back the surface. And then it carried on decomposition pathways discussed in above Sections.

Comprehensively, the final thermal equilibration at 500 K for the decomposed species of butanoic acid and butanol alcohol on Al (111) surface indicated that (1) for butanol alcohol decomposed pieces in M-4: a butanol alcoholate was adsorbed on the surface in a uni-dentate coordination with the dissociated H ion adsorbed onto the surface; (2) for butanoic acid decomposed pieces in M−1, M−2 and M−3: residual alkyl-chains usually anchored to the surface in tri-dentate coordination via their carboxyl C ions, with the OH group and dissociated H and O ions interacting with the surface, which were consistent with experimental observations using the X-ray photoelectron spectroscopy (XPS) at temperatures from 300 to 750 K [8].

4.2.4. Conclusions

Simulations of ab-initio molecular dynamics starting at room temperature (300 K) for the decomposed intermediates of aliphatic butanoic acid and butanol alcohol on clean Al (111) surface, indicated that, (1) Initial decomposition pieces of these additive molecules involved attachments of residual alkyl-chains to Al ions in the surface via their oxygen ions; (2) In further decomposition reactions, the remaining alkyl-chains would anchor to the surface via its end C ion, with the complete liberation of oxygen ions or OH group from the carboxyl (O═C─OH) group to oxidize the surface; (3) The remaining alkyl-chains did not participated in reactions with the surface, but may serve as molecular caps to inhibit migrations of corrosive species into the oxide surface, and let these chains accessible react with other general lubricants in base oil, which may form effective boundary thin-films on the surface.

5. Summary

In this chapter, an ab-initio modeling of lubricant reactions with a metal Al (111) surface are comprehensively discussed using density functional theory (DFT) and ab-initio molecular dynamics (AIMD) based upon the DFT, to illuminate some reasonable reaction outputs in this lubrication field. Some main points from discussions may include, without any loss of generality:

1. If ignoring entropy contributions, for the VPA, the best favorable reaction geometries on Al (111) surface were in the order: tri-bridged coordination > bi-bridged coordination > uni-dentate coordination. While for the EA, the best reaction geometries on Al (111) surface were in the order: bi-bridged coordination > uni-dentate coordination.
2. Comparing these two adsorption types, in each of above adsorption geometries, the binding state of VPA on Al (111) surface was always stronger than that for equivalent EA on the surface. The main reason could be due to a more highly reactive functional group of 2(O)─P═O with the surface than that of O─C═O. H ions liberating from molecular main

pieces and adsorbing on the surface, also influenced all the binding states in above. However, the formation of gaseous H_2 molecules by means of H ions desorbed from the surface was more favorable in adsorption ends.

3. Simulations of ab-initio molecular dynamics starting at room temperature (300 K) for the decomposed intermediates of aliphatic butanoic acid and butanol alcohol on clean Al (111) surface, indicated that, (1) Initial decomposition pieces of these molecules involved attachments of residual alkyl-chains to Al ions via their oxygen ions; (2) In further decomposition reactions, the remaining alkyl-chains may anchor to the surface via their end C ions, with complete liberation of oxygen ions on OH groups from carboxyl (O═C─OH) groups to oxidize the surface; (3) The remaining alkyl-chains did not participate in reactions with the surface, but may serve as molecular caps to inhibit migrations of corrosive species into the oxide surface. And, these chains could be accessible to react with other general lubricants in base oil to form effective boundary thin-films on the surface.

Acknowledgements

This work was supported by the National Science Foundation (Grant no.: DMR9619353), USA; the Hebei Province Science and Technology Support Program (Grant no.: 15961006D), the Hebei Province Science and Technology Research Program for Colleges and Universities (Grant no.: QN2016206), and the Start-up Fund of Doctoral Research at North China Institute of Aerospace Engineering (Grant no.: BKY201405), China.

Author details

Jun Zhong

Address all correspondence to: settings83@hotmail.com

North China Institute of Aerospace Engineering, Langfang, China

References

[1] Totten G, Liang H. Surface Modification and Mechanisms: Friction, Stress and Reaction Engineering. New York: CRC Press; 2004. p. 765. ISBN # 0-8247-4872-7

[2] Sutcliffe M, Combarieu R, Montmitonnet P. Tribology of plane strain compression tests on aluminium strip using ToF-SIMS analysis of transfer films. Wear. 2003;**254**:65-79. DOI: 10.1016/S0043-1648(02)00295-8

[3] Opalka SM, Hector LG Jr, Schmid S, Reich RA. Boundary additive effect on abrasive wear during single asperity plowing of a 3004 aluminum alloy. Journal of Tribology 1999; **121**:384-393. DOI: 10.1115/1.2833951

[4] Coast R, Pikus M, Henriksen PN, Nitowski GA. A vibrational spectroscopic comparison of vinyl-triethoxysilane and vinyl-phosphonic acid adsorbed on oxidized

aluminum. Journal of Adhesion Science and Technology. 1996;(2):101-121. DOI: 10.1163/156856196X00805

[5] Ramsier RD, Henriksen PN, Gent AN. Adsorption of phosphorus acids on alumina. Surface Science. 1988;**203**:72-88. DOI: 10.1016/0039-6028(88)90195-1

[6] Chen JG, Crowell JE, Yates JT Jr. An EELS and TPD study of the adsorption and decomposition of acetic acid on the Al (111) surface. Surface Science 1986;**172**:733-753. DOI: 10.1016/0039-6028(86)90509-1

[7] Crowell JE, Chen JG, Yates JT Jr. The adsorption and decomposition of carboxylic acids on Al (111). Journal of Electron Spectroscopy and Related Phenomena 1986;**39**:97-106. DOI: 10.1016/0368-2048(86)85037-X

[8] Underhill R, Timsit RS. Interaction of aliphatic acids and alcohols with aluminum surfaces. Journal of Vacancy Science and Technology A. 1992;**10**:2767-2774. DOI: 10.1116/1.577908

[9] Zhong J, Adams JB. Adsorption and decomposition pathways of vinyl phosphonic and ethanoic acids on the Al (111) surface: A density functional analysis. Journal of Physical Chemistry C. 2007;**111**:7366-7375. DOI: 10.1021/jp0667487

[10] Available from: Website: http://environmentalchemistry.com/yogi/periodic/crystal.html

[11] Kresse G. VASP the GUIDE. http://cms.mpi.univie.ac.at/vasp/vasp/vasp.html

[12] Kresse G, Hafner J. Norm-conserving and ultrasoft pseudopotentials for first-row and transition elements. Journal of Physics: Condensed Matter. 1994;**6**:8245-8258. DOI: 10.1088/0953-8984/6/40/015

[13] Kresse G, Furthmüller J. Efficient iterative schemes for ab initio total-energy calculations using a plane-wave basis set. Physical Review B. 1996;**54**:11169-11186. DOI: 10.1103/PhysRevB.54.11169

[14] Jiang Y, Adams JB. First principle calculations of benzotriazole adsorption onto clean Cu (111). Surface Science. 2003;**529**:428-442. DOI: 10.1016/S0039-6028(03)00277-2

[15] Hector LG Jr, Adams JB, Siegel DJ. Investigation of vinyl phosphonic acid/hydroxylated α-Al_2O_3 (0001) reaction enthalpies. Surface Science 2001;**494**:1-20. DOI: 10.1016/S0039-6028(01)01387-5

[16] Hohenberg P, Kohn W. Inhomogeneous electron gas. Physical Review. 1964;**136**:B864-B871. DOI: 10.1103/PhysRev.136.B864

[17] Kohn W, Sham LJ. Self-consistent equations including exchange and correlation effects. Physical Review. 1965;**140**:A1133-A1138. DOI: 10.1103/PhysRev.140.A1133

[18] Jones RO, Gunnarsson O. The density functional formalism, its applications and prospects. Reviews of Modern Physics. 1989;**61**:689-746. DOI: 10.1103/RevModPhys.61.689

[19] Blöchl PE. Projector augmented-wave method. Physical Review B. 1994;**50**:17953-17979. DOI: 10.1103/PhysRevB.50.17953

[20] Perdew JP, Wang Y. Accurate and simple density functional for the electronic exchange energy: Generalized gradient approximation. Physical Review B. 1986;**33**:8800(R)-8802(R). DOI: 10.1103/PhysRevB.33.8800. Erratum: DOI: 10.1103/PhysRevB.40.3399

[21] Perdew JP, Chevary JA, Fiolhais C. Atoms, molecules, solids, and surfaces: Applications of the generalized gradient approximation for exchange and correlation. Physical Review B. 1992;**46**:6671-6687. DOI: 10.1103/PhysRevB.46.6671

[22] Murnaghan FD. The compressibility of media under extreme pressures. Proceedings of the National Academy of Sciences of the United States of America. 1944;**30**:244-247. DOI: http://www.pnas.org/content/30/9/244.full.pdf

[23] Monkhorst HJ, Pack JD. Special points for brillouin-zone integrations. Physical Review B. 1976;**13**:5188-5192. DOI: 10.1103/PhysRevB.13.5188

[24] Vanderbilt D. Soft self-consistent pseudopotentials in a generalized eigenvalue formalism. Physical Review B. 1990;**41**:7892(R)-7895(R). DOI: 10.1103/PhysRevB.41.7892

[25] Kroes GJ, Baerends EJ, Mowrey RC. Six-dimensional quantum dynamics of dissociative chemisorption of (v = 0, j = 0) H_2 on Cu (100). Physical Review Letters. 1997;**78**:3583-3586. DOI: 10.1103/PhysRevLett.78.3583. Erratum: DOI: 10.1103/PhysRevLett.81.4781

[26] Tuma C, Sauer J. Treating dispersion effects in extended systems by hybrid MP2: DFT calculations–protonation of isobutene in zeolite ferrierite. Physical Chemistry Chemical Physics. 2006;**8**:3955-3965. DOI: 10.1039/B608262A

[27] Nieto P, Pijper E, Barredo D, Laurent G, Olsen RA, Baerends EJ, Kroes GJ, Farıas D. Reactive and nonreactive scattering of H_2 from a metal surface is electronically adiabatic. Science. 2006;**312**:86-89. DOI: 10.1126/science.112305

[28] Zhong J, Hector LG Jr, Adams JB. Dynamic decomposition of aliphatic molecules on Al (111) from ab initio molecular dynamics. Physical Review B. 2009;**79**:125419. DOI: 10.1103/PhysRevB.79.125419

[29] Heermann DW. Computer Simulation Method in Theoretical Physics. 2nd ed. Berlin: Springer-Verlag; 1990. p. 145. ISBN-13: 978-3540522102

[30] Kojima S, Yokoyama A, Komatsu M, Kiritani M. High-speed deformation of aluminum by cold rolling. Materials Science and Engineering A. 2003;**350**:81-85. DOI: 10.1016/S0921-5093(02)00698-6

[31] Jayatilaka D, Grimwood D. Electron localization functions obtained from X-ray constrained Hartree-Fock wavefunctions for molecular crystals of ammonia, urea and alloxan. Acta Crystallography Section A - Foundations and Advances. 2004;**A60**:111-119. DOI: 10.1107/S0108767303029350

[32] Pauling LC. The Nature of the Chemical Bond. 3rd ed. New York: Cornell University Press; 1960. p. 664. ISBN-10: 0801403332

[33] Rao KB, Jena P, Burkart S, Gantefor G, Seifert G. AlH_3 and Al_2H_6: Magic clusters with unmagical properties. Physical Review Letters. 2001;**86**:692-695. DOI: 10.1103/PhysRevLett.86.692

[34] Totten GE. Handbook of Lubrication and Tribology: Volume 1 Application and Maintenance. 2nd ed. New York: CRC Press; 2006. p. 1224. ISBN: 9780849320958 - CAT # 2095

Chapter 2

Antioxidants Classification and Applications in Lubricants

Majid Soleimani, Leila Dehabadi, Lee D. Wilson and Lope G. Tabil

Additional information is available at the end of the chapter

http://dx.doi.org/10.5772/intechopen.72621

Abstract

Oxidation is a chemical reaction that occurs in lubricants upon exposure to an oxidizing agent such as oxygen and can be catalyzed by copper and iron. Antioxidants are a group of chemicals that can be used in the formulation of lubricants to stop or reduce the rate of oxidation. Based on the mechanism of action, antioxidants are categorized as primary antioxidants (radical scavengers), secondary antioxidants (Peroxide decomposers), and metal deactivators (complex-forming or chelating agents). Selection of the antioxidants in a formulation is a critical decision that depends on the base oil, application and other ingredients in the formulations. Presence of some other ingredients in the product with antagonistic behavior may suppress the role of antioxidants; however, optimal application of antioxidants with synergistic behavior would increase the stabilization impact of the ingredients on the base oil.

Keywords: lubricant, bio-lubricant, antioxidant, oxidation, stability, synergism

1. Introduction

Oxidation is an unwanted process which results in degradation of lubricants (containing hydrocarbons C_{20}-C_{70}) and generation of degradation products. Oxidation can start with the presence of oxidative agents such as oxygen to form a wide range of oxidation products with higher or lower molecular weight relative to the original oil depending on the progress of the process. Generation of lacquer and varnish, viscosity increase, sludge and deposit formation, and corrosion are some important consequences of oxidation. Copper and iron in metal parts, and harsh conditions such high pressure, high temperature, high friction and high metal concentration are factors that accelerate lubricant oxidation. In combustion engines, the generated heat from combustion process would be high enough to oxidize the lubricating oil unless antioxidants present in the formulation inhibit the progress of oxidation and the formation of degradation products.

Antioxidants are a group of additives that have the potential of prohibiting oxidation of base oil in the lubricants and the inhibition of oil breakdown and thickening [1, 2].

2. Mechanism of lubricants oxidation

Oxidation is a multi-step process mainly consisting of three stages: (a) initiation; (b) chain propagation; and (c) termination. In the initiation stage, an external factor (oxidizing agent) causes generation of a free organic radical (R·) or an unpaired electron as part of the lubricant (RH) indicated below:

$$RH \rightarrow R\cdot + H\cdot \tag{1}$$

In the propagation stage, the free radical released during initiation stage is a highly reactive species with the potential of reacting with oxygen to form a peroxide radical. The peroxide radical is another reactive component with the potential of reacting with the lubricant or other components in the lubricant that can result in further decomposition of the lubricant and its components as follows:

$$R. + O_2 \rightarrow ROO\cdot \tag{2}$$

$$ROO\cdot + RH \rightarrow ROOH + R\cdot \tag{3}$$

Branching occurs as:

$$ROOH \rightarrow RO\cdot + \cdot OH \tag{4}$$

$$RO\cdot + RH + O_2 \rightarrow ROH + ROO\cdot \tag{5}$$

$$\cdot OH + RH + O_2 \rightarrow H_2O + ROO\cdot \tag{6}$$

In the termination stage, the radical species generated during initial and propagation stages of oxidation would combine and form a stable organic compound and the free radicals are removed from the lubricating agent. The termination stage can be effective in attenuation or ending the oxidation process if no more radicals are generated during the initiation stage.

$$R. + R. \rightarrow R - R \tag{7}$$

$$R. + ROO. \rightarrow ROOR \tag{8}$$

Altogether, two types of products can be produced during oxidation, namely oil soluble products (such as peroxides, alcohols, acids, esters, aldehydes, and ketones), and oil insoluble products with high molecular weight.

3. Measuring oxidative resistance

The chemical and physical properties of materials can be altered by oxidation. For instance, an increase in the acidity of the samples containing fats and oils can result in corrosion and

rusting. The lubricating properties of such systems can be affected by increasing the viscosity. Oxidation stability testing is essential, as follows: i) development of new products, ii) evaluation of potential new additives and iii) assessment of storage stability [3]. For the purpose of enabling development of valuable new products, it is important to assess the performance of various antioxidants in a lubricant to determine the required treatment-rate and the cost [4].

ASTM D-6186 is a standard method used to measure the performance of an antioxidant in a lubricating substance. In addition, pressurized differential scanning calorimetry (PDSC) is a suitable tool for measuring the oxidative stability. Accordingly, PDSC provides estimates of oxidative stability by detecting exothermic release of heat identified as auto-oxidation. Auto-oxidation is a process by which the antioxidant capacity of the lubricating system goes into the oxidative chain reaction when the effective ingredients are consumed. For example, the effectiveness of two antioxidants was compared using the PDSC test where each antioxidant was added at 2% level to treat the base oil. The results of oxidation induction time (OIT) for both samples heated at 135° for 7 days are shown in **Figure 1**. Many researchers rely on high-pressure differential scanning calorimetry (HPDSC) as an appropriate tool, especially for small samples, where bulk solution effects are minimized and it is facile to detect the interchange of the sample with its atmospheric oxygen. One of the main advantages of this tool is the repeatability of the test procedure with a reasonable reaction time [4–6].

Oxygen pressure vessel method or ASTM D942 (OPVOT) test performance can determine various antioxidants optimum treatment rate to make the most cost-effective formulation in a very short period of time [4]. Lubricants are formulated from a range of base fluids, either mineral or synthetic oils, in which chemical additives are dissolved. The base oil formulation and the nature of the chemical additives will affect on the physical and chemical properties of the lubricant [1]. The life span of the product can be changed using chemical additives for development of lubricants for specific applications. Gas chromatography (GC) and ESI are two significant methods which are used for the analysis of additives related to the additive age,

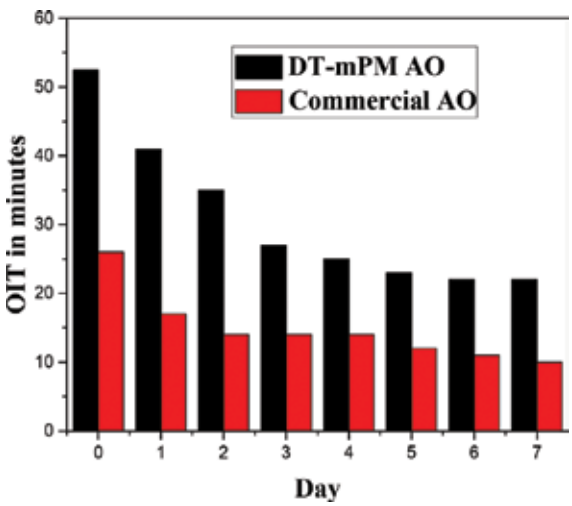

Figure 1. An alternative antioxidant known as DT-mPM displays a greater performance than a commercial antioxidant using PDSC study; AO: alpha-olefin [4].

composition and degradation of the lubricant [7–10]. Antioxidants are among the most important group of additives, that are normally composed of sterically hindered phenols or aromatic amines [1, 2]. The presence of oxygen and high temperatures within a tribological environment can be important factors for rapid oxidation of lubricants. The quantitative analysis of lubricant antioxidant additives in complex and native base oil matrices has been studied using ESI-MS and MALDI-MS [11, 12]. The rotating pressure vessel oxidation test (ASTM-D2272) is the most common method which can measure the RUL (Remaining Useful Life) of the oil's ability to resist oxidation.

Antioxidants are one of the most suitable additives to extend the lifetime of lubricants. Furthermore, antioxidants prevent the oxidative degradation of the lubricant oil thickening and the formation of sludge. Aromatic amines (e.g. dialkylated diphenylamine) and sterically hindered phenols (e.g. 2,6-di-*tert*-butylphenol) are two common antioxidants which are useful in lubricants stabilization to gain synergistic effects [3, 13]. A better understanding of the chemistry of antioxidants and their degradation mechanisms at the molecular level is crucial for developing more efficient lubricants. Lubricants based on mineral oils, are very complex mixtures; therefore, an analytical method with high sensitivity and selectivity to separate the components, and to characterize and quantify antioxidants and their degradation products has been established [14].

4. Activity and classification of antioxidants

Antioxidants are a series of compounds with the capability of controlling oxidation, and consequently preventing oil from breakdown and thickening (increasing viscosity), and helping better performance and longer life of an engine. Natural antioxidants are the chemical compounds that originally present in the mineral oil known as polycycloaromatics and sulfur and nitrogen heterocyclics, or with bio-oil, triglycerides and in biological systems known as tocopherol, astaxanthin, zeaxanthin, lutein, flavonoids, lycopene, etc. In the mineral oil refining process, severe conditions applied in the process strips the base oil of its natural antioxidants [1, 2]. Therefore, the lack of these important group of chemicals should be compensated by supplementation of the base oil using appropriate groups of additives. Three types of antioxidants are generally available, namely, radical scavengers (primary antioxidants), peroxide decomposers (secondary antioxidants), and metal passivators/deactivators [15].

Radical scavengers such as phenolic antioxidants, aromatic amines, and sulfur and phosphorus compounds that stop chain propagation by blocking or reacting with free radicals generated in the initiation stage of oxidation. Blocking of the radicals by the scavengers occurs through donation of hydrogen atoms that react with alkyl or peroxy radicals, leading to the formation of quinones or quinine imines [1, 2, 15].

Peroxide decomposers such as organosulfur (e.g. dialkyl sulfides and dithiocarbamates) and organophosphorus (e.g. triaryl phosphites and trialkyl phosphites) compounds have the conversion potential of hydroperoxides to non-radical derivatives such as alcohols [1, 2, 15].

Metal deactivators such as benzotriazole and N-salicylidene ethylamine acting as surface film-forming compounds or stable complex-forming agents (chelating agent) function by reducing

catalytic effect of metal ions on oxidation. Chelating agents function by trapping metal ions in their structure in the form of stable complexes to reduce the catalytic oxidation activity of the metal ions. Film-forming agents by covering the surface of the metals do not let them enter into the oil phase, and/or these agents may restrict the access of the corrosive species into the metal surface resulting in a reduced corrosive impact of the corrosive agents [1, 2, 15].

Due to the synergistic effect of the antioxidants, combinations of different types of antioxidants are used in lubricant formulations. This synergistic impact of the antioxidants has been proven in several research studies. For example, the results from a study by Davis and Thompson (1996) indicated that alkali metal carboxylic acids and substituted phenols would work as synergists for arylamine antioxidants in ester-based synthetics lubricants. Their results showed that the oil was stable and sludge free when tested at high temperatures at lab scale [16]. In another study by Sharma et al. [17], a synergistic effect was reported where zinc dialkyledithiocarbamate antioxidant was used with an anti-wear additive namely antimony dithiocarbamates in a soybean oil-based lubricant using a pressure differential scanning calorimetry (PDSC) and a rotary bomb oxidation test (RBOT) [17].

Different classifications are available for antioxidants. Based on the source, they can be classified as: (a) natural antioxidants, and (b) synthetic antioxidants. Based on the solubility, they are classified as: (a) oil-soluble antioxidants, and (b) water soluble antioxidants. Based on the mechanism of action: (a) primary antioxidants (radical scavengers), (b) secondary antioxidants (Peroxide decomposers), and (c) metal deactivators. Oil-soluble organic antioxidants are an important group for (hydrocarbon) lubricating oils that can be categorized as discussed in the following subsections.

4.1. Hindered phenolic compounds

Hindered phenols are a group of (primary) antioxidants that function by scavenging mechanism through hydrogen donation in which the target molecules are peroxy radical intermediates. They are active over a wide range of temperature and they can provide a long-term stability of the lubricant with minimizing viscosity change and discoloration. Synergistic effect may result using a combination of hindered phenols and secondary antioxidants such as thioethers and phosphites. The sterically hindered phenols (I) with 2 and 6 positions on the ring substituted by tertiary alkyl groups (such as butyl) are very active antioxidants reacting with the peroxy radical intermediates (**Figure 2**). The product of the first reaction (II) is also reactive functioning as the scavenger of the peroxy radicals [15, 18].

The maximal activity of hindered phenolic antioxidants is attainable when both 2 and 6 positions of the aromatic ring are occupied by tertiary butyl groups; with one substituent replaced by methyl instead of tertiary butyl, the relative antioxidant activity may drop by 37.5% as shown in **Table 1** [18].

4.2. Aromatic amine compounds

This class of antioxidants is more active than the hindered phenols and are available in a wide range of molecular weights and forms. However, aromatic amines contribute more in discoloring

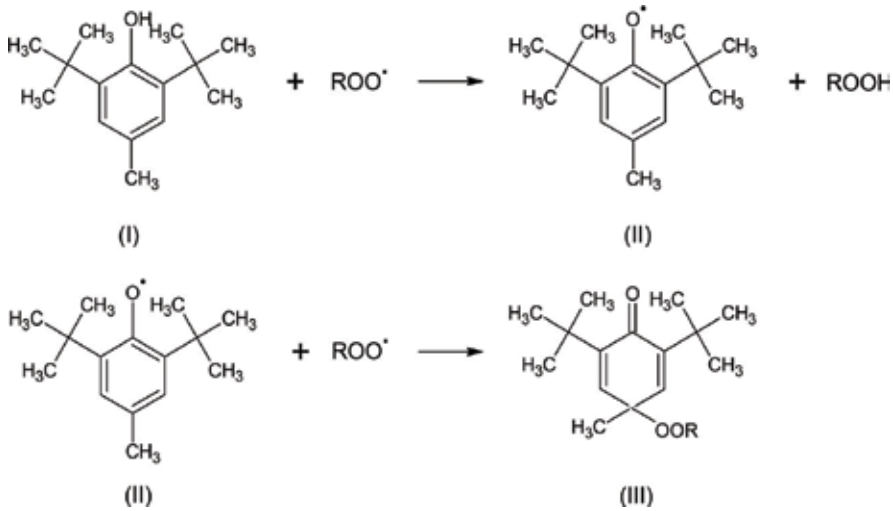

Figure 2. Mechanism of reaction of hindered phenols with peroxy radical.

Phenol structure	Relative antioxidant activity
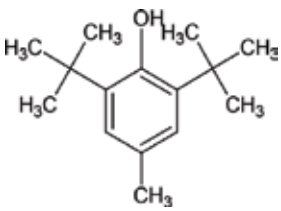	100.0
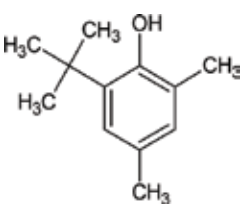	62.5

Table 1. Relative antioxidant activity of phenolic antioxidants affected by the alkyl substituents at the ortho positions [1, 18].

the final product (formulated lubricant) compared to the hindered phenols, especially at higher temperatures or exposure to light [19]. As active hydrogen donors, they can easily transfer the hydrogen atom on nitrogen to peroxy radicals [20, 21]. The typical group in this class of antioxidants are called alkylated diphenyl amines that are substituted amine antioxidants synthesized by the reaction between diphenylamine and alkylating agents. This group of antioxidants are used in lubricants as well as synthetic polymers and rubber vulcanizates [22]. The mechanism of action of aromatic amines can simply be presented as follows **Figure 3**:

http://dx.doi.org/10.5772/intechopen.72621

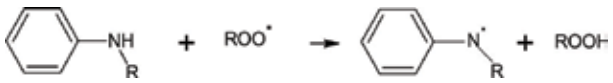

Figure 3. Mechanism of action of aromatic amines on peroxy radicals [resketched from 1, 2, 19].

The mechanism of the sequential reaction of the alkylated diphenylamine under low temperatures (<120°C) is shown in **Figure 4** [1, 23]. At the end of this reactions resulting in the elimination of four peroxy radicals, two compounds are generated, namely; 1,4-benzoquinone and an alkylated nitrosobenzene.

Comparing a diphenylamine molecule with sterically hindered monophenols, the former has the scavenging potential of four peroxy radicals, while the sterically hindered monophenols have the potential of elimination of 2 equivalents of peroxy radicals.

At higher temperatures (>120°C), after reaction of the antioxidant with the peroxy radical and formation of the nitroxyl radical in the second step, this compound would have the potential of reacting with (scavenging) a secondary alkyl radical leading to the regeneration of the original alkylated diphenylamine (**Figure 5**). It has been proven that the performance of the antioxidants based on diphenylamine depends on the substituents in the para position such that stoichiometric efficiencies of over 12 radicals per molecule have been reported in this regeneration process [1, 24].

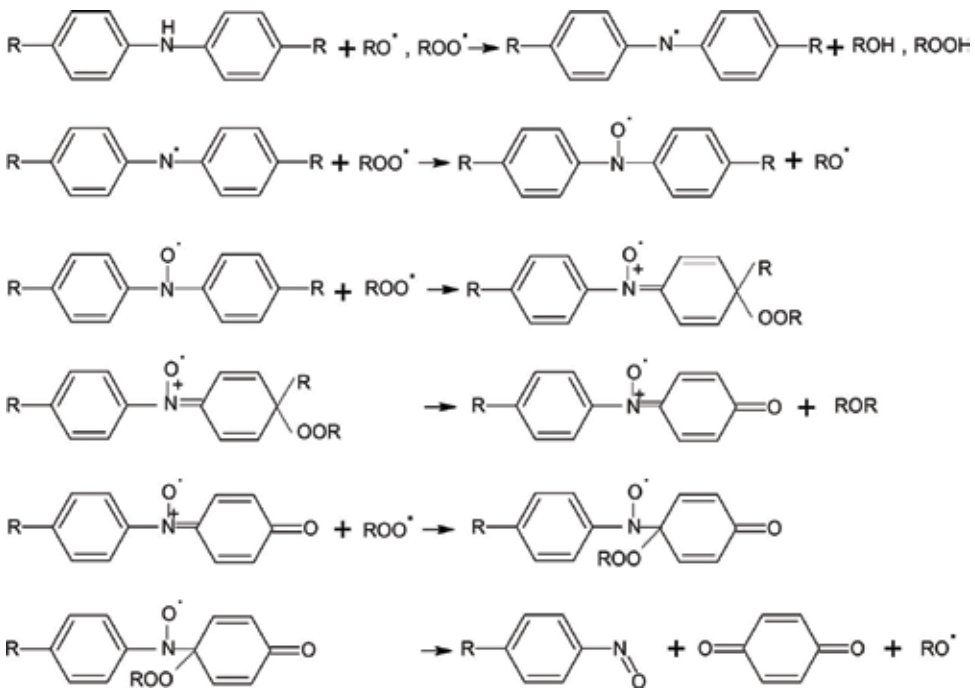

Figure 4. Mechanism of sequential reaction of alkylated diphenyl amine with peroxy radical at low temperatures (<120°C) [resketched from 1 and 2].

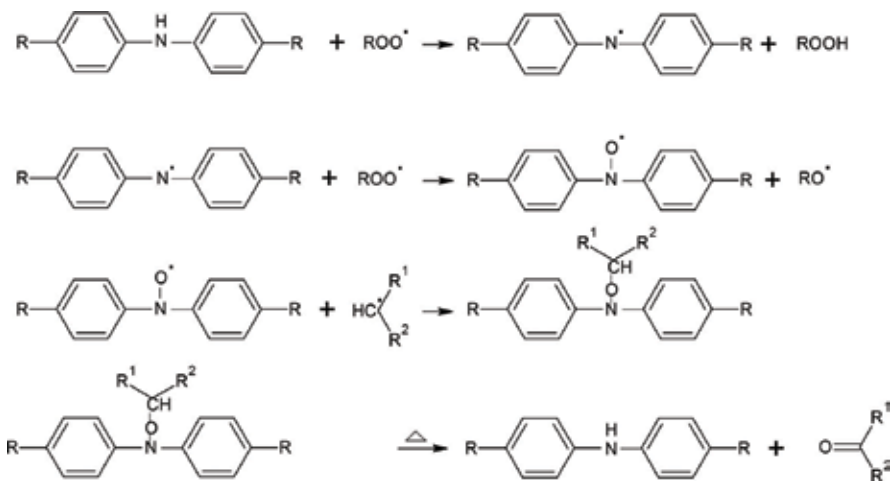

Figure 5. Mechanism of reaction of alkylated diphenyl amine with peroxy radical at high temperatures (>120°C) [resketched from 1].

The performance of aromatic amines on NO_x emissions from soybean biodiesel powered DI diesel engine has been investigated [25]. The results indicated that at 75% load for B100 fuel enriched with DPPD (N,N′-diphenyl-1,4-phenylenediamine) and NPPD (N-phenyl-1,4-phenylenediamine) as effective antioxidants, reductions of 28.36 and 20.96% were obtained with NO emissions, respectively. For B20, less reduction of NO was achieved with DPPD and NPPD additions compared to B100. The effectiveness of the both antioxidants in B100 and B20 fuels was proved for NO emissions.

In another study by Hess et al. [26], incorporation of antioxidants including butylated hydroxyanisol and butylated hydroxytoluene at 1000 ppm concentration in B20 resulted in the reduction of NO_x gases in a single-cylinder engine as shown in **Table 2** [26]. According to

Fuel	Change in NO_x from B20 combustion (%)
B20 + 2-ethylhexyl nitrate	−4.5 ± 1.0
B20 + 2,2′-methylenebis(6-tert-butyl-4-methylphenol)	+0.2 ± 1.0
B20 + citric acid	−0.7 ± 0.5
B20 + α-tocopherol	+0.3 ± 0.2
B20 + ascorbic acid 6-palmitate	−1.3 ± 0.9
B20 + tert-butyl hydroquinone	−0.3 ± 1.6
B20 + propyl gallate	−0.4 ± 2.8
B20 + diphenylamine	+0.7 ± 1.3
B20 + butylated hydroxytoluene (BHT)	−2.9 ± 1.5
B20 + butylated hydroxyanisole (BHA)	−4.4 ± 1.0

Table 2. The influence of additives on NO_x emission during combustion [26].

http://dx.doi.org/10.5772/intechopen.72621

the results, the two aforementioned antioxidants were more helpful than other antioxidants but less effective than 2-ethylhexyl nitrate (EHN) which is an accepted NO_X-lowering agent.

A study was carried out by Mukul et al. [27] to evaluate the importance of chemistry of antioxidants on the oxidative stability and thermo-oxidative properties of gear oil. They conducted the experiments on 4 oil blends, namely AO I (no antioxidant added), AO II (with an amine antioxidant (Irganox L57) added), AO III (with a phenolic antioxidant (Irganox L135) added, and AO IV (with both Irganox L57 and Irganox L135 added). In the high-pressure differential scanning calorimetry (PDSC) test at 160°C, the following order obtained for oxidation induction temperature (OIT) of the oil blends:

$$\text{AO II} > \text{AO IV} > \text{AO III} > \text{AO I} \tag{9}$$

A similar trend was also obtained for rotating pressure vessel oxidation test (RPVOT) results for the oil blends tested confirming a good correlation between the two test methods. However, a reverse trend of results for the oxidation level (%) of the aforementioned oil blends was achieved. According to the results, amine antioxidant resulted in a better performance compared to the phenolic antioxidant and synergism of the antioxidants did not have a significant role in delaying the oxidation reactions. The higher performance of amine antioxidant compared with the phenolic antioxidant on the thermo-stability of the lubricant could be its catalytic manner of reaction and regeneration over several cycles of scavenging and breaking of chain reactions of oxidation.

Thermal stability of polyol ester lubricant was affected by different types of antioxidants as reported by Mousavi et al. [28]. Among the systems studied, Phenyl-R-naphthylamine (PAN) showed a remarkable improvement on the thermal stability of the base oil (**Figures 6** and **7**) indicating less acid and less HMW products generation in this oil blend at high temperature (220°C). The greater area in **Figure 7** is the representation of the generation of high-molecular weight products (HMW) due to oxidation and polymerization reactions.

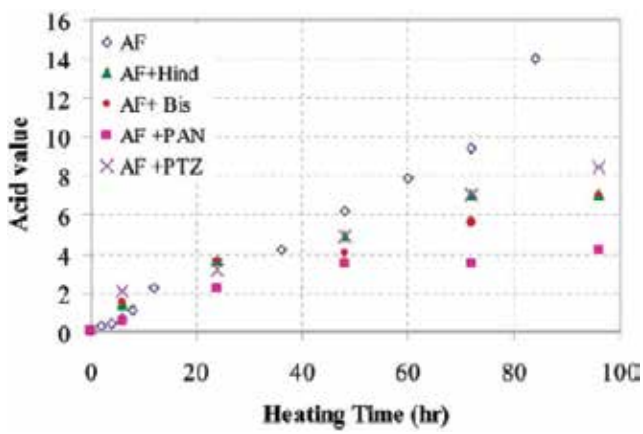

Figure 6. Acid values of original oil (AF) and inhibited oil (using different antioxidants) heated at 220°C over time. Reprinted with permission from [28].

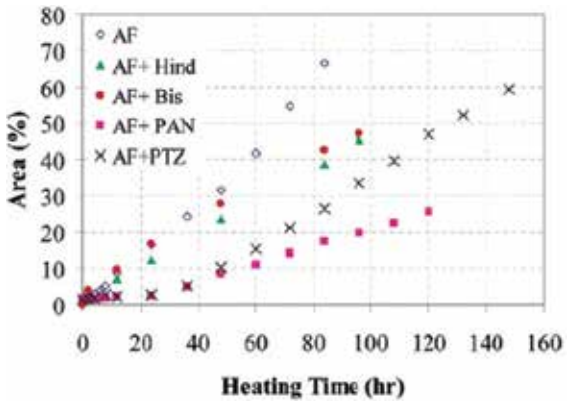

Figure 7. Peak area (%) obtained with gel permeation chromatography (GPC) for high molecular weight (HMW) chemicals generated at 220°C through oxidation/polymerization reactions. Reprinted with permission from [28].

4.3. Organosulfur compounds

Organosulfur compounds function as hydroperoxide decomposers by converting them into non-radical products. Acid-catalyzed decomposition is the most important mechanism of eliminating hydroperoxides in the lubricating system with acid catalysts sourced from organosulfur compounds, as reported by Hawkins and Sautter [29].

Compounds such as dialkyl sulfides (R-S-R) would react with hydroperoxide molecules converting them to sulfoxides as shown in **Figure 8**:

In the next step, assuming R is an alkyl, sulfoxide molecule can be converted (by heat) to sulfenic acid (RSOH) which is a very reactive acid, as outlined in **Figure 9**:

Since sulfenic acid is an unstable material, especially in the presence of hydroperoxide, it can be easily transformed to sulfinic acid decomposition occurs that can function as an acid catalyst in the decomposition of hydroperoxides at low temperature. At higher temperatures, sulfinic acid decomposition occurs by thermolysis and is converted to SO_2 that functions as the catalyst for hydroperoxide decomposition (**Figure 10**).

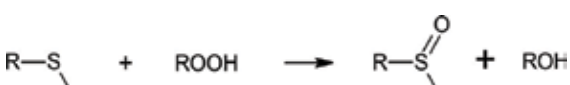

Figure 8. Conversion of hydroperoxides to dialkyl sulfoxide by dialkyl sulfide.

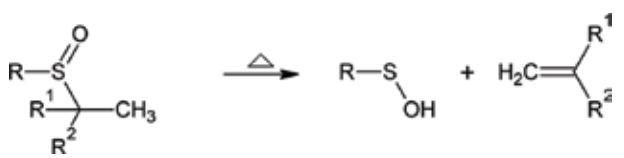

Figure 9. Generation of sulfenic acid from sulfoxide molecule.

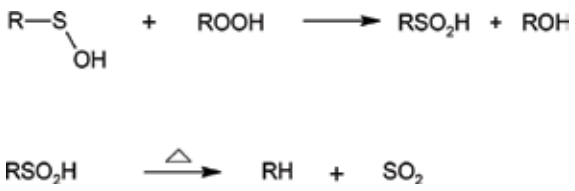

Figure 10. Conversion processes of sulfenic acid by hydroperoxide, and sulfinic acid by heat.

According to Bridgewater and Sexton [30], sulfur dioxide functions as a powerful Lewis acid such that one equivalent can decompose up to 20,000 equivalents of cumene hydroperoxide, i.e., 5–60 $\times$ 10^{-6} mol/l of the sulfur compound decomposed over 50% of the 0.2 mol/l of cumene hydroperoxide in a 6-h period [30].

In addition to the sulfur-based acids mentioned above, sulfacids (RSO_xH) are also considered organosulfur antioxidants with a mechanism of reaction with peroxy radicals (**Figure 11**) and functioning as a primary antioxidant as below:

4.4. Organophosphorus compounds

Among organophosphorus compounds, phosphites are the main group of compounds that are used in the formulation of lubricants to overcome the oxidation reactions. They have the potential of reacting with hydroperoxides, peroxy and alkoxy radicals (**Figure 12**). Therefore, they can be effective on the stability of color and physical and rheological properties of the lubricant. In the reaction with hydroperoxide or peroxy radical, phosphite is oxidized to the corresponding phosphate, while the hydroperoxide and peroxy radical are reduced to a less reactive alcohol and alkoxy radical, respectively [1, 2].

If phosphite possesses a phenoxy group in its structure, it would eliminate peroxy and alkoxy radicals through reaction with them and also the generated phenoxy radical from this reaction would be a stable radical with the potential of elimination peroxy radicals (**Figure 13**). Stability of the generated phenoxy radicals due to their steric hindrance by the two alkyl groups on the ortho positions of the aromatic ring makes them appropriate antioxidant candidates in moist systems of lubrication [1, 2].

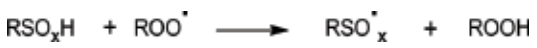

Figure 11. Reaction of sulfacids with peroxy radicals [resketched from [1, 2].

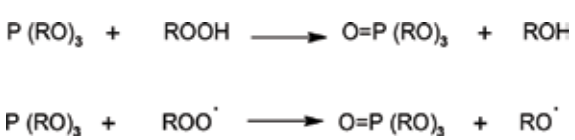

Figure 12. Reactions of phosphite with hydroperoxide and peroxy radicals [resketched from 1, 2].

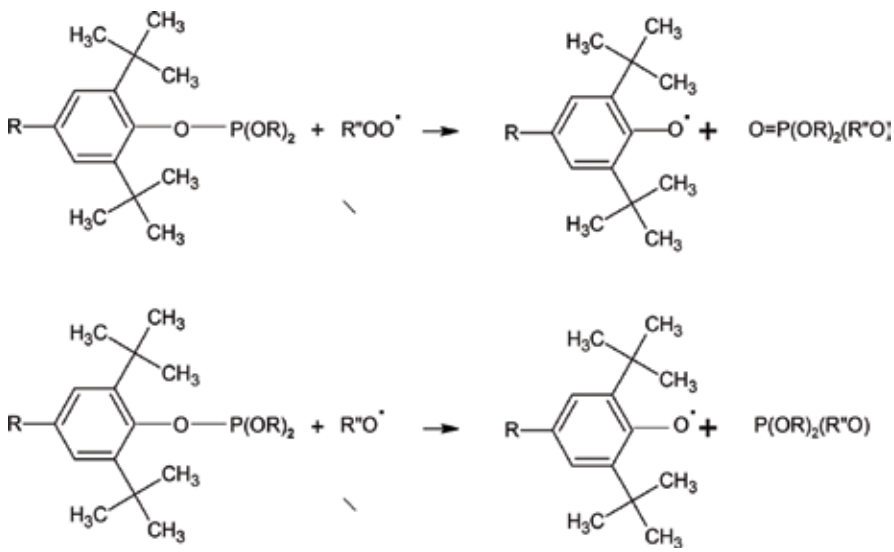

Figure 13. Reactions of phosphite (possessing phenoxy) with alkoxy and peroxy radicals [resketched from 2].

4.5. Sulfur-phosphorus compounds

Antioxidants with both sulfur and phosphorus elements are more efficient and effective than those with either sulfur or phosphorus. Metal dialkyldithiophosphates are a group of antioxidants in this class that have been widely used and have been synthesized by the reaction between phosphorus pentasulfide and alcohols (such as aliphatic, cyclic and phenolic, lauryl, octyl, methyl cyclohexyl, etc.) to produce dithio-phosphoric acids followed by a neutralization process using a metal compounds (such as zinc, barium, calcium and molybdenum compounds or oxides). Zinc dialkyldithiophosphate (ZDDP) is one of the well known compounds in this group that have been used as an effective antioxidant and anti-wear component in the lubricant industry for several years [2].

4.6. Organo-zinc compounds (Zn dithiophosphate ZDTP/ZDP)

ZDTP/ZDP work as antioxidant and anti-wear agents protecting metals against corrosion in the lubricants formula. Therefore, they are considered multifunctional additives in engine oils and hydraulic fluids. The alcoholic group used in the structure of the compound is an important factor on the performance of the product, i.e. primary and secondary ZDTPs (with aliphatic alcohols) provide better results in terms of oxidation inhibition and wear protection compared to aryl ZDTP. The overall performance of ZDTPs would be affected by the presence of other additives in the formulation of the lubricating product [31–33].

In a typical antioxidant mechanism activity of ZDTP, an acid-catalyzed ionic decomposition of hydroperoxide may occur. First, ZDTP and hydroperoxide can form a basic ZDTP and then through some sequential reactions, hydroperoxides are decomposed. A typical example of the reaction between ZDTP and hydroperoxides outlined in [1] **Figures 14** and **15**:

ZDTP may also directly react with peroxy radicals leading to active inhibitors as shown below:

http://dx.doi.org/10.5772/intechopen.72621

Figure 14. A typical reaction of ZNTP with hydroperoxides.

Figure 15. Reaction mechanism of ZDTP with peroxy radical.

The final radical $(RO)_2PS_2^{\cdot}$ also has the potential of reacting with hydroperoxide and generating hydrogenated acid form of this compound with the functionality of an inhibitor.

4.7. Organo-copper compounds

Copper as a transition metal has been considered an oxidation promoter which may cause damage in the lubricant or lubricating systems; however, copper salts that are soluble in oil are reported to function as antioxidants [34, 35]. Limitation of loading copper within 100 to 200 ppm to obtain the optimal control of oxidation and wear is a drawback for copper-based antioxidants. Over this range, the performance of the anti-wear components in the lubricants would drop due to the reverse impact of copper. Organo-copper antioxidants are effective in ester and mineral oil lubricants at temperatures below 250°C.

Organo-copper compounds including copper naphthenates, oleates, stearates, and polyisobutylene succinic anhydrides have been reported to be synergistic with multi-ring aromatic compounds in controlling high-temperature deposit formation in synthetic base stocks [2].

According to some other studies, inclusion of oil-soluble compounds of copper in the range of 5 to 500 ppm resulted in improved performance of the automotive crankcase lubricants in terms of anti-wear, antioxidant performance and corrosion resistance [36].

4.8. Organo-molybdenum compounds

Molybdenum dithiocarbamate has been reported to function as an antioxidant and anti-wear component in the lubricants. However, it would lose its protective properties by time due to dropping its concentration below the critical level of activity [37]. The synergistic application of Molybdenum dialkyldithiocarbamate (MoDDC) with arylamines was tested to improve the durability and low friction performance of MoDDC over time. The DSC (differential scanning calorimetric) results have indicated that the oxidation and induction temperatures for a poly-α-olefin (PAO) lubricant would increase by the addition of MoDDC to the formulation. Also, MoDDC would have an antioxidative synergism with alkylated diphenylamine antioxidants (arylamines) such as octyl- and butyl-containing diphenylamine compounds.

5. Antioxidants/additives synergism and antagonism

Synergistic mixtures of antioxidants from different groups or classes are generally applied in the formulation of commercial lubricants to provide better stability toward oxidation. In

lubricating systems that involve a synergistic mechanism, free radical scavengers are the major antioxidant component, while the hydroperoxide decomposers function as auxiliary components for the free radicals [38]. It was reported that the oil-soluble organic molybdenum (organic molybdenum complex (MC)) and arylamine antioxidant (dioctyldiphenylamine (DODPA)) would have an excellent antioxidant synergism in an oil system (poly-alphaolefin synthetic lubricant (PAO)) as shown in the DSC thermogram (**Figure 16**). The OIT was increased from 221.4°C with DODPA as the sole antioxidant to 229.7°C with the combination of DODPA and MC as the synergistic antioxidants. Also, a lower acid generation and lower kinematic viscosities were observed after oxidation-corrosion test for the lubricant with antioxidant, especially in the lubricant with both DODPA and MC due to their synergistic impact (**Table 3**). As a consequence, a lower deposit occurs when both antioxidants are in the system (**Figure 17**) compared with the lubricants that contain DODPA solely.

In another study by Hu et al. [39] where a molybdate ester (ME) and dioctyldiphenylamine (DODPA) were used as antioxidants, a synergistic effect was reported between the two antioxidants.

Synergistic behavior of sulfonated calcium carbonate and an ashless antioxidant (N-phenyl-α-naphthylamine (T531)) in hydrogenated oil was investigated and the results suggested that anti-wear and antioxidant effect were synergistically improved in the system [40].

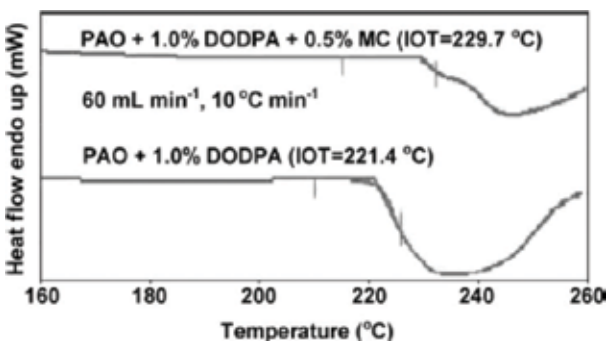

Figure 16. DSC thermograms of PAO oxidation in the presence of DODPA with or without MC [38]. Reprinted by permission of the Society of Tribologists and Lubrication Engineers, www.stle.org.

Lubricant	ΔTAN	ΔKV (%)
Polyalphaolefin (PAO)	8.2	216
PAO + 0.5% MC	5.6	180
PAO + 1.0% DODPA	3.6	36.8
PAO + 1.0% DODPA +0.5% MC	2.1	15.3

ΔTAN: change in the total acid number; ΔKV: change in the kinematic viscosity.

Table 3. The change in total acid number and viscosity after 24 h in oxidation-corrosion test [38].

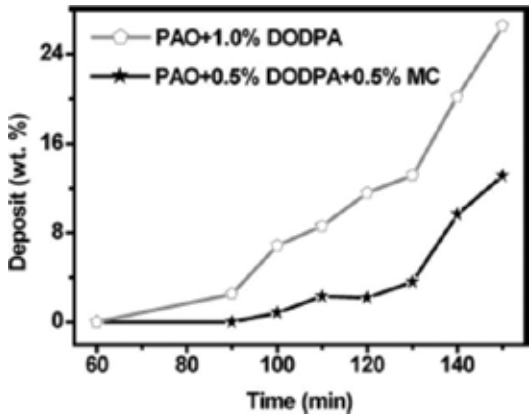

Figure 17. Deposit formation in PAO in the presence of DODPA with or without MC [38]. Reprinted by permission of the Society of Tribologists and Lubrication Engineers, www.stle.org.

In contrast to synergism, the presence of mixtures of antioxidants with other additives may have antagonistic behavior. Therefore, the combinations of the antioxidants along with other lube additives in a lubricating fluid need to be optimized to prohibit or minimize antagonism. It has been shown that anti-wear and antioxidant properties of ZDDPs have been adversely affected by some additives such as detergents and dispersants (sulfonates, phenates and salicylates). This undesired effect can be due to the competition of detergents and dispersants with ZDDPs by surface adsorption or restricted interaction of this component with the metal or the fluid phase [41].

6. Bio-based antioxidants and lubricants

Triglycerides from plant sources have been used as biolubricants with limited applications due to their low thermal and oxidative stability. As well, triglycerides have low volatility, high lubricity, low toxicity and good viscosity-temperature properties as their key advantages. Therefore, different antioxidants such as tocopherols, propyl gallate (PG), ascorbyl palmitate (AP), and some synthetic antioxidants (butylated hydroxyanisole (BHA), butylated hydroxytoluene (BHT), mono-*tert*-butylhydroquinone (TBHQ), or 4,4′-methylenebis(2,6-di-*tert*-butylphenol) (MBP)) have been used to improve their resistance to the oxidative agents. In recent years, a great number efforts have been made to develop sustainable bio-lubricants and additives wit the preference of non-toxicity, multi-functionality and compatibility to the present systems. Cellulose fatty esters have been developed as the lubricant additive, mainly for antioxidant applications. It has been modified to cellulose ferulate, cellulose lipoate and α-tocopherulate for antioxidant functionality [42, 43].

In a study by Singh et al. [44], cellulose laurate was synthesized for use as an effective biolubricant. The results indicated that the lubrication performance would increase with the degree of substitution (DS) in cellulose molecule and by increasing the concentration of cellulose laurate in the base oil which was *n*-butyl palmitate/stearate.

In another study [45], a multi-function additive as detergent/dispersant/antioxidant/anti-wear was developed from L-histidine (HDS) for bio-lubricant applications. Two types additives namely, Ca-HDS-L and Ca-HDS-M were synthesized by esterification with lauroyl chloride and myristoyl chloride, respectively. Using the products in a polyol base oil indicated that Ca-HDS-L worked as a better detergent and dispersant, but Ca-HDS-M functioned as a more effective antioxidant. The oxidative properties obtained by the two additives (ca. 1–3 g/l addition to the oil) are presented in **Table 4**.

Lubricant	TAN (soluble)	Total sludge (%)	Total oxidation products (%)
Polyol	2.019	32.454	34.416
Polyol +1000 ppm Ca-HDS-L	1.598	0.497	3.530
Polyol +2000 ppm Ca-HDS-L	1.514	0.022	1.300
Polyol +3000 ppm Ca-HDS-L	1.402	0.013	1.579
Polyol +1000 ppm Ca-HDS-M	0.476	0.065	2.423
Polyol +2000 ppm Ca-HDS-M	1.514	0.076	1.282
Polyol +3000 ppm Ca-HDS-M	1.458	0.021	1.183

Table 4. The effect of multi-function additives (Ca-HDS-L and Ca-HDS-M) on quality properties of a polyol lubricant in universal oxidation test (IP 306); TAN: Total acid number [45].

7. Future of antioxidants

Competent and creative research is still needed in the study of oil antioxidants. Some important questions as why one type of antioxidant is efficient in one kind of oil and inefficient in another is often puzzling. Lubricants can affect the environment to various extents; thus, the development of new environmentally friendly lubricant formulations is required. Moreover, new types of antioxidants are still being developed and further improvement in the design of high temperature antioxidants is required. Furthermore, several key issues in the field of lubrication and their relation to recent improvements are revealed as follows: corrosive properties of oily additives, shear strength and durability of high pressure agents, internal cohesion and viscosity of organic liquids, improvements in the viscosity index scale, and synthetic oils and their improvement [14].

In the future, along with improvement in lubricants performance, the service change lifetime also is intended to be extended. Polybutenes play a key role for control the viscosity in an extensive range of automotive and industrial lubricants. The disadvantages of using low-viscosity polybutenes are due to restrictions in volatility and oxidation resistance limit for base oil applications. ZnDTPs, hindered phenols, alkylated diphenylamines, organomolybdenum compounds and dithiocarbamates are antioxidants that are used for the protection of lubricants against oxidation. On the other hand, future antioxidants should be developed with consideration related the to environmental and emissions concerns, improved fuel/energy efficiency, higher performance standards, and new base stocks [1].

Author details

Majid Soleimani[1]*, Leila Dehabadi[2], Lee D. Wilson[2] and Lope G. Tabil[1]

*Address all correspondence to: mas233@mail.usask.ca

1 Department of Chemical and Biological Engineering, University of Saskatchewan, Saskatoon, SK, Canada

2 Department of Chemistry, University of Saskatchewan, Saskatoon, SK, Canada

References

[1] Mortier RM, Fox MF, Orszulik S. Chemistry and Technology of Lubricants. 3rd ed. Springer; 2010

[2] Rudnick LR. Lubricant additives: Chemistry and applications. CRC Press. 2009

[3] Nolan SJ, Savin R. The evaluation of oxidation resistance of lubricating greases using the rapid small scale oxidation test (RSSOT). ELGI Paper. 2016:1-10

[4] Canter N. Antioxidants: Key additives enable lubricants to operate under more severe conditions. Tribology & Lubrication. 2016:10-21

[5] http://www.machinerylubrication.com/Read/989/fluid-degradation-causes [Accessed: 16.09.2017]

[6] Aguilar GA, Stunkel B, Donnelly SG. Antioxidant synergist for lubricating compositions. US. Patent 2007127836, November 8, 2007

[7] Hoffmann BR, Knorr W, Walther A, Lehmann WA. Determination of zinc O,O'-dialkyl dithiophosphate lubricant additives via the corresponding methyl and p-nitrobenzylic ester derivatives using GC-MS, GC-NPD and HPLC-MS. Fresenius Journal of Analytical Chemistry. 1997;**357**:688-694

[8] Bernabei M, Seclì R, Bocchinfuso G. Determination of additives in synthetic base oils for gas turbine engines. Journal of Microcolumn Separations. 2000;**12**:585-592

[9] Becchi M, Perret F, Carraze B, Beziau JF, Michel JP. Structural determination of zinc dithiophosphates in lubricating oils by gas chromatography–mass spectrometry with electron impact and electron-capture negative ion chemical ionization. Journal of Chromatography A. 2001;**905**:207-222

[10] Eide I, Zahlsen K, Kummernes H, Neverdal G. Identification and quantification of surfactants in oil using the novel method for chemical firgerprinting based on electrospray mass spectrometry and chemometrics. Energy & Fuels. 2006;**20**:1161-1164

[11] Alberici RM, Simas RC, Abdelnur PV, Eberlin MN, de Souza V, de Sa GF, Daroda RJ. A highly effective antioxidant and artificial marker for biodiesel. Energy & Fuels. 2010;**24**: 6522-6526

[12] Kassler A, Pittenauer E, Doerrb N, Allmaiera G. CID of singly charged antioxidants applied in lubricants by means of a 3D ion trap and a linear ion trap-Orbitrap mass spectrometer. Journal of Mass Spectrometry. 2011;**46**:517-528

[13] Costa CD, Reynolds JC, Whitmarsh S, Lynch T, Creaser CS. The quantitative surface analysis of an antioxidant additive in a lubricant oil matrix by desorption electrospray ionization mass spectrometry. Rapid Communications in Mass Spectrometry. 2013;**27**: 2420-2424

[14] Zisman WA. Present problems and future trends in lubrication. Industrial and Engineering Chemistry. 1953;**45**:1406-1414

[15] Kuo CH. Tribology—Lubricants and Lubrication. InTech; 2011

[16] Davis TG, Thompson JW. Synergistic antioxidants for synthetic lubricants. Industrial & Engineering Chemistry. 1996;**5**:76-80

[17] Sharma BK, Perez JM, Erhan SZ. Soybean oil-based lubricants: A search for synergistic antioxidants. Energy & Fuels. 2007;**21**:2408-2414

[18] Wasson JI, Smith WM. Effect of alkyl substitution on antioxidant properties of phenols. Industrial & Engineering Chemistry. 1953;**45**:197-200

[19] Website. http://adhesives.specialchem.com/selection-guide/antioxidants-for-adhesives/primary-antioxidants#amines [Accessed: 16.09.2017]

[20] Nishiyama T, Yamaguchi T, Fukui T, Tomii K. Chain-breaking fused heterocyclic antioxidants: Antioxidant activities of phenothiazines compared to related compounds. Polymer Degradation and Stability. 1999;**64**:33-38

[21] Lucarini M, Pedrielli P, Pedulli GF, Cabiddu S, Fattuoni C. Bond dissociation energies of OH bonds in substituted phenols from equilibration studies. Journal of Organic Chemistry. 1996;**61**:9259-9263

[22] Gatto VJ, Elnagar HY, Moehle WE, Schneller ER. Redesigning alkylated diphenylamine antioxidants for modern lubricants. Lubrication Science. 2007;**19**:25-40

[23] Berger H, Bolsman TAB, Brower DM. Catalytic inhibition of hydrocarbons autoxidation by secondary amines and nitroxides. In: G. Scott, editor. Developments in Polymer Stabilisation. London: Elsevier Applied Science Publishers; 1983. 1-27

[24] Jensen RK, Korcek S, Mahoney LR, Zinbo M. Liquid–phase autoxidation of organic compounds at elevated temperatures 1. The stirred flow reactor technique and analysis of primary products from n-hexadecane autoxidation at 120–180°C. Journal of the American Chemical Society. 1979;**101**:7574-7584

[25] Varatharajan K, Cheralathan M. Effect of aromatic amine antioxidants on NOx emissions from a soybean biodiesel powered DI diesel engine. Fuel Processing Technology. 2013; **106**:526-532

[26] Hess MA, Haas MJ, Foglia TA, Marmer WN. Effect of antioxidant addition on NOx emissions from biodiesel. Energy & Fuels. 2005;**19**:1749-1754

[27] Mukul RJ, Sawant R, Paulmer RDA, Ganguli D, Vasudev G. Evaluation of thermo-oxidative characteristics of gear oils by different techniques: Effect of antioxidant chemistry. Thermochimica Acta. 2005;**435**:172-175

[28] Mousavi P, Wang D, Grant CS, Oxenham W, Hauser PJ. Effects of antioxidants on the thermal degradation of a polyol ester lubricant using GPC. Indusrial & Engineering Chemistry Research. 2006;**45**:15-22

[29] Hawkins WL, Sautter H. Synergistic antioxidant combinations. Mechanism of stabilization with organo-sulfur compounds. Journal of Polymer Science Part A. 1963;**1**:3499-3509

[30] Bridgewater AJ, Sexton MD. Mechanism of antioxidant action: Reactions of alkyl and aryl sulphides with hydroperoxides. Journal Of The Chemical Society, Perkin Transactions. 1978;**2**:530

[31] Habeeb JJ, Stover WH. The role of hydroperoxides in engine oil and the effect of zinc dialkylthiophosphates. ASLE. Transactions. 1987;**30**:419-426

[32] Roper GW, Bell JC. Review and Evaluation of Lubricated Wear in Simulated Valve Train Contact Conditions SAE 952473. Warrendale, PA: Society of Automotive Engineers; 1995

[33] Bec S, Tonck A, Georges JM, Coy RC, Bell JC, Roper GW. Relationship between mechanical properties and structures of zinc dithiophosphate anti-wear films. Proceedings of The Royal Society of London A. 1999;**455**:4181-4203

[34] Colclough T. Lubricating Oil Oxidation and Stabilization. In: G. Scott, editor. Atmospheric Oxidation and Antioxidants. Elsevier Science Publishers; 1993

[35] Klaus EE, Duda JL, Wang JC. Study of copper salts as high-temperature oxidation inhibitors. Tribology Transactions. 1992;**35**:316-324

[36] Richardson HW. Handbook of Copper Compounds and Applications. CRC Press; 1997

[37] Hu J, Hu Y, Qiu Z, Sun Y. Evaluation on Synergistic Antioxidation of Molybdenum dialkyldithiocarbamate with Arylamine Antioxidant. SAE Technical Paper 2007–01-4135; 2007

[38] JQ H, Wei XX, Cai GL, Liu CC, Fu Y, Zong ZM, Yao JB. Study demonstrating enhanced oxidation stability when arylamine antioxidants are combined with organic molybdenum complexes. Tribology Transactions. 2007;**50**:205-210

[39] JQ H, Wei XY, Yao JB, Han L, Zong ZM. Evaluation of molybdate ester as a synergist for arylamine antioxidant in lubricants. Tribology International. 2006;**39**:1469-1473

[40] Zhongyi H, Liping X, Sheng H, Aixi C, Jianwei Q, Xisheng F. Tribological and antioxidation synergistic effect study of sulfonate-modified nano calcium carbonate. PLoS One. 2013;**8**:1-7

[41] Pereira G, Lachenwitzer A, Kasrai M, Bancroft GM, Norton PR, Abrecht M, Gilbert PUPA, Regier T, Blyth RIR, Thompson J. Chemical and mechanical analysis of tribofilms from fully formulated oils part 1—Films on 52100 steel. Tribology. 2007;**1**:48-61

[42] Trombino S, Cassano R, Bloise E, Muzzalupo R, Leta S, Puoci F, Picci N. Design and synthesis of cellulose derivatives with antioxidant activity. Macromolecular Bioscience. 2008;**8**:86-95

[43] Trombino S, Cassano R, Bloise E, Muzzalupo R, Tavano L, Picci N. Synthesis and antioxidant activity evaluation of a novel cellulose hydrogel containing trans-ferulic acid. Carbohydrate Polymers. 2009;**75**:184-188

[44] Singh RK, Sharma OP, Singh AK. Evaluation of cellulose laurate esters for application as green biolubricant additives. Industrial Engineering & Chemistry Research. 2014;**53**: 10276-10284

[45] Singh RK, Kukrety A, Thakre GD, Atray N, Ray SS. Development of new ecofriendly detergent/dispersant/antioxidant/antiwear additives from L-histidine for biolubricant applications. RSC Advances. 2015;**5**:37649-37656

Section 2

Lubrication of Materials

Chapter 3

Tribological Interaction of Bio-Based Metalworking Fluids in Machining Process

Erween Abd. Rahim, Amiril Sahab Abdul Sani and Norfazillah Talib

Additional information is available at the end of the chapter

http://dx.doi.org/10.5772/intechopen.72511

Abstract

Metalworking fluids were applied during the machining process to lubricate and cool the machine tool in order to reduce wear, friction, and heat generated. The increasing attention to the environment and health impacts leads to the formulation of eco-friendly metalworking fluids derived from vegetable oils (Jatropha and palm oils) to substitute the use of mineral-based oil. The present work focuses on the performance of refined bio-based metalworking fluids during tapping torque and orthogonal cutting processes. Bio-based metalworking fluids were formulated using 0.05 wt.% of hexagonal boron nitride (hBN) and 1 wt.% of phosphonium-based ionic liquid $[P_{66614}][(^{i}C_{8})_{2}PO_{2}]$ in a modified Jatropha and palm olein oils and were examined for their rheological properties in comparison with a commercially obtained synthetic ester (SE)-based cutting fluid. The tapping torque performance of the refined bio-based metalworking fluids was evaluated for their torque and efficiency. In addition, the performance of these bio-based metalworking fluids on orthogonal cutting parameters such as cutting force, cutting temperature, chip thickness, tool-chip contact length, and specific cutting energy was highlighted. The results obtained revealed that the rheological properties of the newly formulated bio-based metalworking fluids were improved. From the tapping torque and orthogonal cutting performances, it was proven that the modified palm and Jatropha oils possess good anti-wear and anti-friction behavior compared to SE. In conclusion, the newly formulated bio-based metalworking fluids are suitable for the use as a new advanced renewable metalworking fluid for machining processes that correspond to the energy-saving benefits and environmental concerns.

Keywords: boron nitride, environmentally adapted metalworking fluid, ionic liquid, renewable sources, sustainable machining

1. Introduction

Sustainability has become an important element to be considered in the manufacturing industry. Sustainable manufacturing has led machining industries to replace petroleum-based lubricants with bio-derived lubricants. Normally, the conventional lubricants consist of the combination of petroleum-based lubricant and additives that are toxic to the environment and difficult to be disposed of after the consumption [1]. The widespread use of petroleum-based lubricant may cause a negative effect to human such as dermatitis, acne, asthma, and a variety of cancers [2]. Hence, lubricants from vegetable oils are favorable as a sustainable alternative to the conventional petroleum-based oil. Vegetable-based lubricant offers significant environmental benefits with respect to resource renewability, biodegradability, as well as providing satisfactory performance in a wide array of applications [3].

In the machining process, metalworking fluids (MWFs) are typically used to separate tool-workpiece interface. MWFs provide lubrication, reduce the friction and wear, cool, and protect metal surfaces against corrosion. Tribology process occurs at the contact area between tool and workpiece, which related to friction, lubrication, and wear of interacting surfaces in a relative motion. Tribology process can be classified as physical, physical-chemical (adsorption), or chemical in nature (tribochemistry) [4]. The absence of MWFs will result in acceleration of tool wear, residual stress, dimensional error, and poor surface finish [5]. Previous researchers have identified that MWFs made of canola/rapeseed, palm, and sunflower oils provided greater lubricating properties and showed comparable performance with currently used petroleum-based MWFs regarding cutting force, cutting temperature, surface finish, tool wear, and tribological behavior [6–8]. Vegetable-based MWFs have high viscosity and viscosity index that significantly influenced the machining performances that provide effective lubricating properties on the tool-chip contact surfaces [8]. Vegetable-based MWFs formed a thin film between tool and workpiece that offers good boundary lubrication condition with a low coefficient of friction [9].

Normally, MWFs contain a combination of base oil and additives. There are various functions of additives being used to enhance the MWFs performance such as antiwear, antifriction, extreme-pressure, antioxidant, and anticorrosion [10]. The addition of additives in base oil could give either beneficial or detrimental effect on the tribological behavior depending on the types of additive, particle size, and concentration. Hence, to have a better understanding on the lubrication and tribology, modified vegetable oils (modified Jatropha oil and modified RBD palm olein) were added with various types of additives (hexagonal boron nitride and phosphonium-based ionic liquid). The effects of various formulations of modified vegetable oils were examined through rheological properties, tapping torque, and orthogonal cutting performances.

1.1. Green solid additive

The green solid particles such as hexagonal boron nitride (hBN), aluminum oxide (Al_2O_3), molybdenum disulfide (MoS_2), carbon nanotube (CNT), and nano-diamond were added in various neat MWFs to increase thermophysical properties and generate a protective film on the contact surfaces [11]. These solid particle additives composed of environmentally benign

lamellar powders that have low interlayer friction, ability to form protective boundary layers, and accommodate relative surface velocities [12].

Zhang et al. [13] examined the effect of vegetable-based oils (soybean oil, palm oil, and rapeseed oil) as base lubricants containing nanometer-sized particles as additives and hence, the name nanofluids, during minimum quantity lubrication (MQL) grinding of 45 steel workpiece in comparison with liquid paraffin. The results indicated that palm oil-based nanofluids mixed with MoS_2 nanoparticles produce the best lubricating property in the nanoparticle jet MQL condition due to the high saturated fatty acid and high film-forming property of the carboxyl groups in palm oil. They noted that high viscosity of nanofluids induced good lubricating effect but significantly reduced heat transfer performance. The combination of green solid particles in vegetable oil provided a strong absorption capability and high film strength which enhanced the lubricating property and heat transfer performance. Li et al. [14] performed an experiment on minimum-quantity lubricant cooling (MQLC) grinding of a Ni-based alloy. Palm-based oil was added with different volume fractions of carbon nanotube (CNT) nanoparticles in between 0.5 and 4%. The results found that the volume fraction of 2% of CNT nanoparticles in palm-based oil had achieved the optimal lubrication and heat transfer performance. They initiated that thermal conductivity and viscosity of nanofluids significantly influence the heat transfer properties. Nam et al. [15] conducted an experiment on MQL micro-drilling with the addition of nano-diamond particles in paraffin and vegetable-based oils. The experimental results show that 2 vol. % of nano-diamond particles in the vegetable-based oil significantly reduce the magnitudes of average drilling torques and thrust forces.

At present, the potential of hBN particle as an additive in MWF has been discovered. This solid additive acts as a viscosity, friction, and wear modifiers in many polar and nonpolar oils. Nguyen et al. [16] conducted an experiment on the 3-axis vertical milling center and the lubricant was supplied through MQL method. The results showed that 0.5 wt. % of hBN particles concentration in vegetable-based oil (Unist-Coolube 2210) reduced flank and central wear. A paper by Abdullah et al. [17] has studied the effect of hBN and Al_2O_3 in diesel engine oil by mixing 0.5 vol. % of the solid particles in SAE 15 W40 with the particle size of 70 nm. The results showed that the viscosity index of nano-oil with hBN was improved by 3% compared to nano-oil without additive and nano-oil of Al_2O_3. This finding was due the lower thermal expansion coefficient of hBN (1×10^{-6}/°C). The hBN particles were completely dispersed in the SAE 15 W40 oil and maintained the lubrication properties of the base oil. Furthermore, Talib et al. [18] conducted an experiment on four-ball tribology test of modified Jatropha oil with hBN particles as an application for MQL oil. The modified Jatropha oils were added with the various concentration of hBN particles between 0.05 and 0.5 wt. %. The results revealed that the addition of 0.05 wt. % of hBN particles in the modified Jatropha oil had exhibited excellent tribological performances of the four-ball tribology test in terms of low coefficient of friction, small wear scar diameter, smooth surface roughness, and low volume of wear rate. They indicated that the presence of 0.05 wt. % hBN particles tended to reduce the friction that occurred on the sliding surfaces. The lubrication effect of the MQL oil changed from sliding friction to rolling friction due to the presence of the small amount of hBN particles, which led to the reduction of friction and wear.

1.2. Ionic liquids

Ionic liquids are chemical compounds composed of cations and anions that have melting points lower than 100°C. The cations are usually organic compounds such as nitrogen or phosphorus, and the anions are the weakly coordinating compounds like bis(trifluoromethylsulfonyl)imide or hexafluorophosphate [19–21]. For many years since the first ionic liquid (IL) was reported in 1982, the research and development of ILs have been rapidly evolving in the research works and in various industrial applications [19, 21–24]. IL lubricants are found in lubricant industries as neat lubricant or lubricant additives for various mechanical lubrication purposes [20, 25, 26].

ILs exhibit remarkable properties such as nonflammable, nonvolatile, low melting point, high thermal stability, highly miscible with organic compound, and better intrinsic properties [27, 28]. Use of ILs as lubricant additives may eliminate further requirements of using detergents, defoamers, antioxidants, or even antiwear and antifriction additives in enhancing the performance of the conventional lubricant in current additive formulation processes [27–29]. Thanks to the abovementioned advanced characteristics of ILs, they have been proven to not only improve the tribological properties (friction and wear) [28–30] of different polar and nonpolar base oils, but also enhanced their physicochemical properties (viscosity, thermal and oxidative stability, pour point) [20, 31].

Pham et al. in 2014 examined the effect of two imidazolium-based ILs ([EMIM] [TFSI] & [BMIM] [I]) as neat lubricants in micro end milling [32]. They suggested the potential use of these ILs as green lubricants that exhibit extremely low volatile organic compounds as well as for the use in MQL systems. A study by Davis et al. in 2015 uses water-based lubricant with an additive of a 0.5 wt. % of [BMIM-PF_6] IL when cutting titanium round bars using MQL system [33]. They found out that the lubricant mixture has effectively reduced the tool wear by 60% when compared to dry cutting and 15% more than MQL without the IL. Goindi et al. [34] have recently proposed the use of imidazolium-based ILs with two different anions in minute quantity being mixed in a canola vegetable oil during orthogonal milling of a plain medium carbon steel via MQL method. They reported that the small quantities of the two imidazolium-based ILs ($[BMIM]^+$ with $[PF_6]^-$ & $[BF_4]^-$) have significantly affected the tribological conditions of the milling process by reducing the peak and mean machining forces in finish as well as rough machining conditions.

Somers et al. [35] tested the application of various imidazolium-, phosphonium-, and pyrrolidinium-based ILs as lubricant additives in different polar and nonpolar base oils including vegetable oil, polyolesters, mineral oil, and polyalphaolefin and found that the miscibility of ILs in these base oils depends highly on the molecular structures of the ILs used. High miscibility in both polar and nonpolar base oils is apparent for ILs that comprise quaternary structures with relatively long hydrocarbon chains of the cations and anions [20, 30]. Several recent studies have confirmed this finding and provided reports on their tribological investigations using lubricant mixtures on different material sliding pairs [36–39].

To date, tailor-made ILs investigated for the application as lubricants and/or lubricant additives have known to play an important role in enhancing tribological interactions between sliding materials. The application of IL-based MQL machining may be explored for other nontoxic, fully miscible, and biocompatible ILs as neat as well as lubricant additives in various base oils

for different metalworking applications [20]. Halogen-containing anions such as [PF6] or [BF4] contain rich fluorine compound that is moisture-sensitive [20, 40]. They can cause corrosion on the steel surface under humid conditions, thus may release toxic and corrosive hydrogen halides to the environment. In this work, a biocompatible with low-toxic level of phosphonium-based IL, trihexyl (tetradecyl) phosphonium bis (2,4,4-trimethylpentyl) phosphinate, [P66614] [(iC8)2PO2] (PIL) was investigated as an oil-miscible IL in polar base vegetable-based lubricants. The application of 1 wt. % of PIL is anticipated to be adequately sufficient in improving the lubrication performance of the base oil when used on the metal sliding surfaces [30, 31].

2. Methodology

2.1. Lubricant preparation

The crude vegetable oils were modified to enhance certain limitations such as low thermal and oxidative stability due to unsaturation in oil molecule. There are various methods of modification that have been identified by Shashidhara and Jayaram [41] which included reformulation of additives, chemical modification, and genetic modification of oilseed. Prior to this experiment, fatty acid methyl esters (FAMEs) from Jatropha oil and RBD palm olein were chemically modified through transesterification process to develop modified Jatropha oil (MJO) and modified RBD palm olein (MRPO) [18, 31]. They are the product of the transesterification process (ester) between FAMEs from the vegetable oils with a polyol of trimethylolpropane (TMP) and better known as the TMP triester. After the transesterification process, the absence of hydrogen atom at carbon-β in the structure of the ester oil has enhanced the thermal and oxidative stability [42]. Both MJO and MRPO were mixed with two different types of additives; hexagonal boron nitride (hBN) and phosphonium-based ionic liquid (PIL). A small amount of 0.05 wt. % of hBN particles were blended in the base oils using a magnetic follower at a temperature of 60°C for 30 min. Meanwhile, 1 wt. % of PIL was heated at 70°C to reduce its viscosity prior to the mixing procedure with the base oils. Next, the preheated PIL was poured into the base oil and heated at 60°C and stirred rigorously by using the magnetic follower for 30 min. The modified oils were compared with a commercial synthetic ester (SE, Unicut Jinen MQL) as a reference oil.

2.2. Rheological properties

The rheological properties were determined through kinematic viscosity (ASTM D445) and viscosity index, VI (ASTMD2270). The kinematic viscosity was measured using a viscometer at 40 and 100°C. It was calculated from the ratio of dynamic viscosity over density at the same temperature. The correlation between viscosity and temperature was further associated with VI. The testing was repeated for three times and the average value was recorded.

2.3. Tapping torque test

Tapping torque tests (ASTM D5619) were carried out on a CNC machine, installed with a tapping torque set up, as shown in **Figure 1**. The tests were conducted using AISI 1215 cylindrical low carbon steels at the machining speed of 400 rpm as shown in **Table 1**. The workpieces

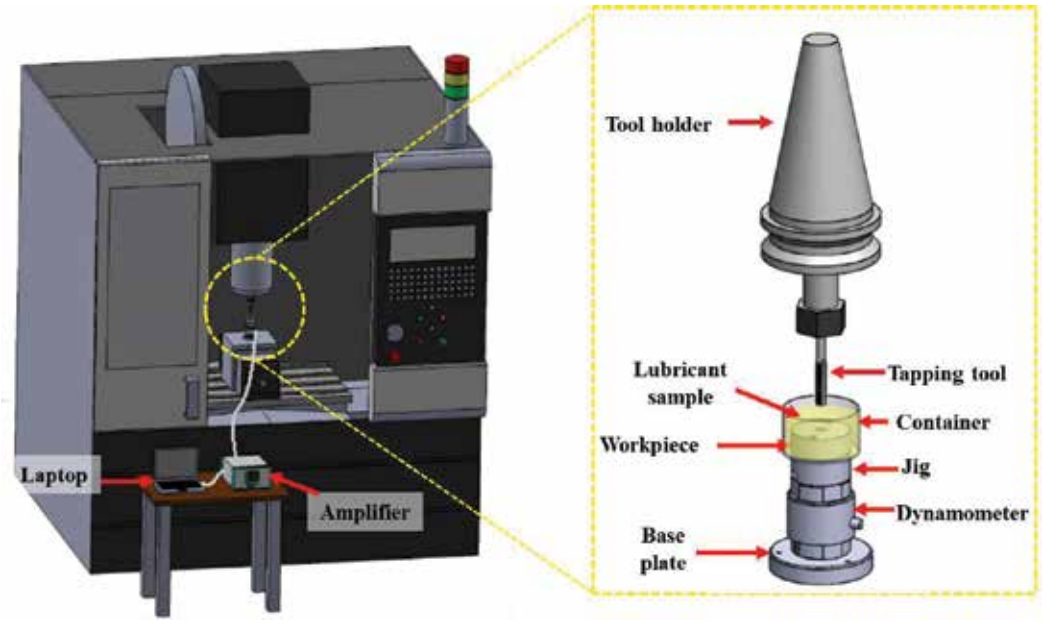

Figure 1. Tapping torque set-up [18].

were predrilled with 5 mm diameter drill bit size. Tapping was performed using an uncoated high-speed steel tapping tool with the size of M6x1.0. The workpiece attached on the jig was later mounted on a dynamometer, Kistler 9345A. The dynamometer was amplified via a multichannel amplifier, Kistler 5070. Approximately, 20 ml of the lubricant sample was poured into the container to lubricate the tools during the tapping process. The result of the torque was recorded using the Dynoware software. Each tapping process was repeated five times for each lubricant sample, prior to averaging the torque values. The efficiency of tapping torque was calculated according to Eq. (1).

$$\text{Efficiency (\%)} = \frac{\text{Average torque of reference oil}}{\text{Average torque of lubricant sample}} \quad (1)$$

Description	Value
Spindle speed (rpm)	400
Feed rate, f_r(mm/rev)	1
Hole depth (mm)	12 (through hole)
Tapping tool	High speed steel, M6
Lubricant volume (ml)	30
Workpiece material	AISI 1215 steel
Workpiece dimension (mm)	Ø37×12

Table 1. Tapping torque test parameter.

2.4. Orthogonal cutting

Orthogonal turning process was conducted on an NC lathe machine (Alpha Harrison 400) to cut a steel disk of AISI 1045 plain medium carbon steel. The tool used was a square shape insert with a positive rake angle of 5°, clearance angle of 11°, and a model number of SPGN120308. The tool insert was fixed on a modified tool holder of CSDPN 2525 M12 in a way that the chip will flow freely without any hindrance on the rake surface of the cutting insert during the chip formation process. The steel disk has an initial diameter and width of 150 and 2 mm respectively. The complete cutting parameter is shown in **Table 2**.

The cutting tool was fixed on a dynamometer, Kistler 9275BA in order to measure the cutting forces. The forces measured were amplified by using the Kistler 5070 amplifier and were recorded on a PC for data analysis. The lubricants were supplied via an MQL system directly to the cutting edge at the tool-workpiece interfaces. The air supply pressure was fixed at 4 bar and the flow rate was set at 0.16 l/hr. The MQL nozzle with an outlet diameter of 2.5 mm was located at a distance of 8 mm between the nozzle outlet and the tool-workpiece interfaces and inclined at 45° to the cutting edge plane. The maximum cutting temperature was captured by using an infrared thermal camera (FLIR T640) within a temperature range of 0–1000°C. The camera was located parallel to the axial direction of the lathe machine facing toward the cutting zone. The schematic diagram of the complete setup assembly on the lathe machine is shown in **Figure 2**.

Each cutting test was conducted twice using each of the lubricant sample and new cutting edge to reduce measurement error during the results analysis. At the end of each cutting operation, the cutting forces were recorded and the chips were collected for cutting force evaluation and chip thickness measurement analysis respectively. The cutting force was determined in the Z-axis during the chip formation process. At least 10 chips were measured for their thickness by using a digital micrometer. The specific cutting energy, U, was calculated using Eq. (2), where F_c is the cutting force, w is the cutting depth, and t_o is the undeformed chip thickness [43].

$$U = \frac{F_c}{t_o \cdot w} \tag{2}$$

Description	Value
Cutting speed, v_c (m/min)	350
Feed, f (mm/rev)	0.12
Cutting depth, w (mm)	2
Disk diameter (mm)	150
Disk thickness, d (mm)	2
MQL lubricants	SE; MJO + hBN0.05%; MJO + PIL1; MRPO + hBN0.05%; MRPO + PIL1%
MQL supply pressure (MPa)	0.4
MQL flow rate (l/hr)	0.16
Nozzle inner diameter (mm)	2.5
Nozzle distance (mm)	8

Table 2. Cutting parameter of the orthogonal lathe machining.

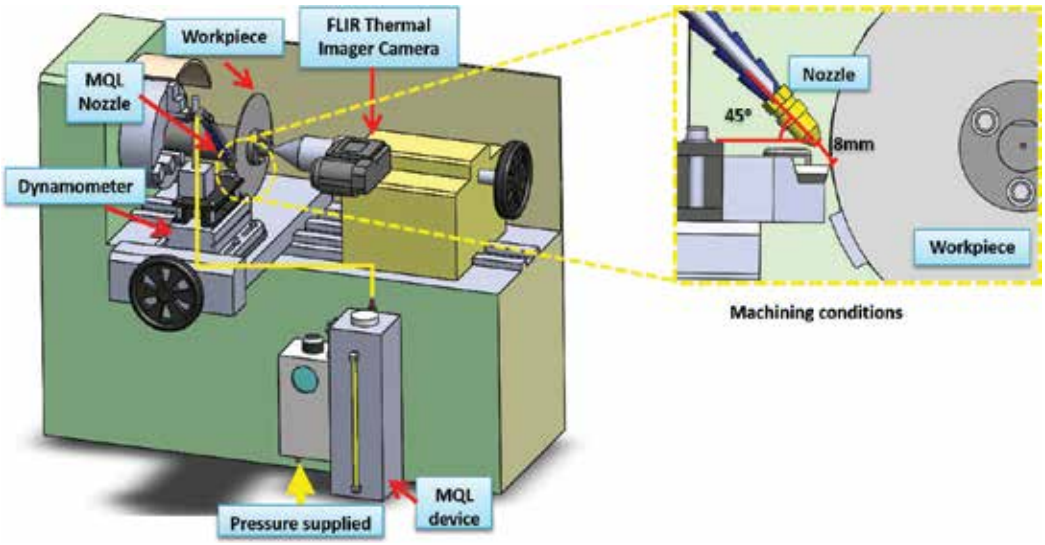

Figure 2. Orthogonal lathe cutting set-up.

Finally, the sliding region on the tool insert's rake face was analyzed under an optical microscope and the tool-chip contact length was measured for data analysis. Scanning electron microscope (SEM) was used to further analyze the surface morphology of the sliding regions.

3. Results and discussions

3.1. Rheological properties

Figure 3 displays the kinematic viscosity values and the calculated viscosity index (VI). The kinematic viscosity of the reference oil (SE) at 40 and 100°C are 21.5 and 5.6 mm^2/s, respectively. It can be seen that MRPO + hBN0.05% shows the highest kinematic viscosity values of 22.2 mm^2/s at 40°C and 6.35 mm^2/s at 100°C. The addition of hBN particles in MRPO-based oil improves the viscosity values due to lower thermal expansion coefficient of hBN particles (1×10^{-6}/°C), thus enhanced the thermal stability [17]. Meanwhile, MRPO + PIL1% recorded the kinematic viscosity values of 22.21 mm^2/s at 40°C and 6.25 mm^2/s at 100°C. Both MRPO-based oils demonstrated the highest kinematic viscosity value compared to MJO-based oils and SE due to the high saturation of fatty acids in the MRPO-based oil. MRPO-based oil contains high composition of saturated fatty acid (palmitic acid, $C_{15}H_{31}COOH$) at 50–70% [44]. Meanwhile, both MJO-based oils had the lowest kinematic viscosity values at both temperatures. This can be explained by the presence of unsaturated fatty acids (oleic acid, $C_{17}H_{33}COOH$ and linoleic acid, $C_{17}H_{31}COOH$) in MJO-based oil [45]. Moreover, MRPO + PIL1% demonstrates the highest VI value of 259 which was 17% higher than SE. The high VI is desirable as it indicates little changes in viscosity across a wide range of operating temperature. Both MJO-based oils had the lowest VI values which had 5% reduction compared to SE.

http://dx.doi.org/10.5772/intechopen.72511

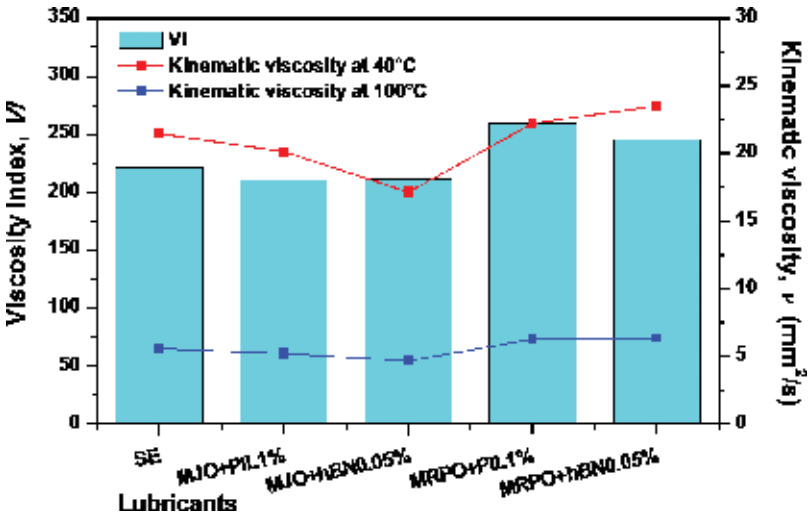

Figure 3. The kinematic viscosity values at 40 and 100°C and the calculated viscosity index value.

3.2. Tapping torque performance

Figure 4 shows the tapping torque and efficiency for all lubricant samples. The reference oil (SE) had the highest tapping torque at 129 Nm. The results reveal that the tapping torque for all modified vegetable oils exceeded the tapping torque of SE. MJO + PIL1% had the lowest tapping torque of 104 Nm correlated with the highest tapping torque efficiency of 124%. The presence of PIL as an additive improves the tapping torque performance. This is because of the addition of PIL in MJO-based oil, which is thermally more stable than SE. The alkyl chain length and hydrogen bonding between the cation and the anion seem to influence the tribofilm formation of PIL [29]. Meanwhile, MJO + hBN0.05% recorded tapping torque of 117 Nm with the tapping torque efficiency of 110%. The presence of hBN particles provided a thin lubrication film that allows the particles to change from sliding friction to the rolling friction [18]. Moreover, the presence of long carbon chain length of MJO-based oil and MRPO-based oil which is between 16 and 18 carbon number had enhanced the adsorption ability of the fatty acids on the metal surfaces, thus exhibited better tapping torque performance. MRPO + hBN0.05% and MRPO + PIL1% had tapping torque efficiency of 107 and 106%. It can be seen that the addition of PIL and hBN particles as the additive in MRPO-based oil did not significantly affect the tapping torque performance compared to the MJO-based oils. This scenario is due to the weak tribo-chemical reactions of additives with the MRPO-based oil, thus reduced the adsorption ability of the lubricant molecules on the metal surface [46].

3.3. Orthogonal cutting performance

The orthogonal lathe cutting operations were conducted at a constant speed and feed. The cutting force, cutting temperature, chip thickness, specific cutting energy, and tool-chip contact length are the main outputs of this experimental section analysis. The results for each lubricant mixture were compared with the conventional cutting fluid, synthetic ester (SE).

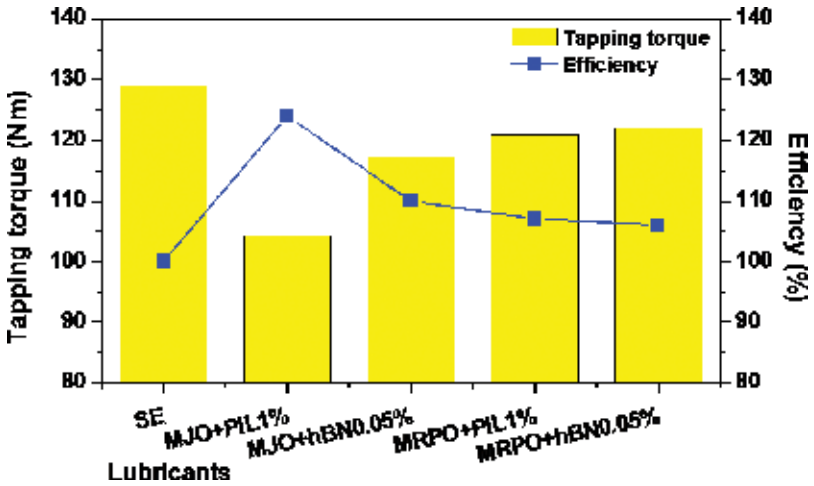

Figure 4. Tapping torque and torque efficiency value of all lubricant samples.

3.3.1. Cutting force and temperature analysis

Figure 5 shows the results of cutting force, F_c measured in the Z-axis and the maximum cutting temperature results after the orthogonal cutting operations. It is shown that SE produced the highest cutting force and cutting temperature at ca. 612 N and 308°C respectively. SE generated poor lubrication condition on the cutting zone as compared to the other lubricant samples. MJO + PIL1% produces the greatest reduction of cutting force (2% reduction) as well as the cutting temperature (10% reduction) compared to the SE which corresponds to the good lubrication ability of the PIL additive contained in the base oil, MJO. The addition of 0.05 wt. % hBN solid particles also improved the lubrication ability of the MJO base oil. It is anticipated that the different type of lubricant used with the addition of the same additive did

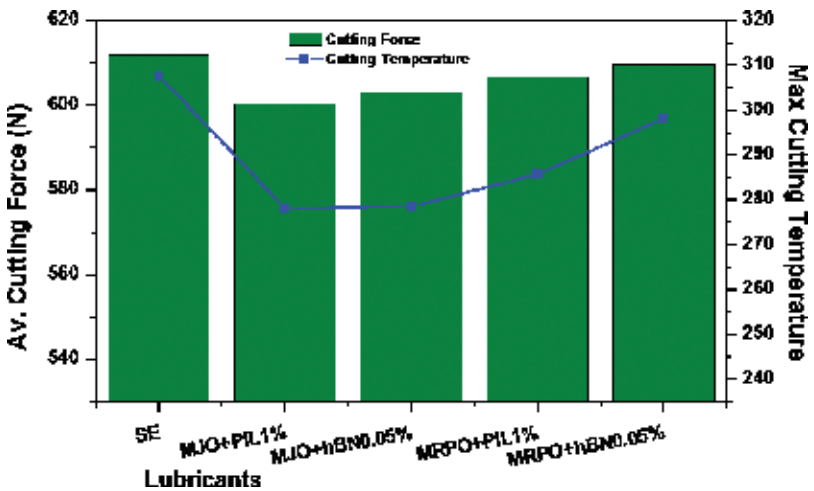

Figure 5. Cutting force and temperature results.

give similar improvement effect as shown by the results of MRPO base oil. MRPO + PIL1% and MRPO + hBN0.05% show a reduction in both cutting force and cutting temperature when compared to the SE in a range between 0.4 and 8% decrement respectively.

The addition of 1 wt. % PIL has enhanced the antifriction and antiwear properties of the base oil by reducing the scuffing effect and the abrasive wear mechanism [25]. The polarity of the phosphonium-based IL additive has resulted in the increased adsorption rate of the additive molecules on the metal surface. The result is also corroborated by the tapping torque and efficiency values reported in the previous section. The tribofilm formed helps lower the frictional torque of the base oil corresponding to the reduction of friction coefficient. It acts as a separation layer between the metal asperities and kept them apart from direct contact, thus reduces the cutting force and generates less heat.

The addition of 0.05 wt. % hBN solid particles in the base oil reduces the average cutting force as well as the heat generated within the cutting zone by separating the metal asperities contacts during the sliding processes. However, the ability of the particles in reducing the frictional force and the heat generation is greatly affected by the particles filling rate in the asperity valleys which enabled them to align in parallel to the relative sliding motion, thus reducing the stress concentration on the contact surfaces [31]. Therefore, the high polarity of the PIL and the ability of its anionic moieties that can quickly adsorb on the sliding metal surfaces via strong electrostatic interactions even at high temperature and load working conditions has become the most attractive contribution of the PIL additive toward the formation of tenacious lubricant films on the metal surface that greatly reduces friction and wear [20]. This type of lubricant additive has successfully improved the tribological performance of the polar oil of MJO- and MRPO-based lubricant samples during the machining of the plain medium carbon steel of AISI 1045 [47].

3.3.2. Chip thickness analysis

The average chip thickness after the machining processes is exhibited in **Figure 6**. During the material removal process, the chip is formed due to the elastic, elastic-plastic, and plastic deformation processes of the workpiece material. It is mainly influenced by the heat generation under high stresses and temperature arisen due to the high deformation resistance between the cutting insert and the workpiece material being cut [48]. The chip thickness is one of the parameters that affected the chip formation mechanisms with the shearing angle between the uncut chip thickness and the cutting forces required during the material removal process [39].

An effective surface lubrication on the cutting zone has helped reduce the chip thickness produced after the machining operations by reducing the thermal stresses that occurred on the sliding surfaces. As presented in the previous subsection, the reduced friction due to high lubrication effect of MJO + PIL1% compared to the SE has successfully decreased 20% of the chip size which indicates the reduced tensile strain on the outer surface of the chip during bending. The specific thermal effects were reduced due to the adequate lubricant being sprayed and penetrated the sliding interfaces [49]. In addition, the fast and strong electrostatic interactions between the lubricant and additive molecules with the metal substrates had formed the tenacious lubricant film that reduced the contact area at the shear zone, thus resulting in the reduction of frictional force [20, 30, 38]. Furthermore, this phenomenon also contributed to thinner chips being cut with large shear angle and low cutting energy. These results were

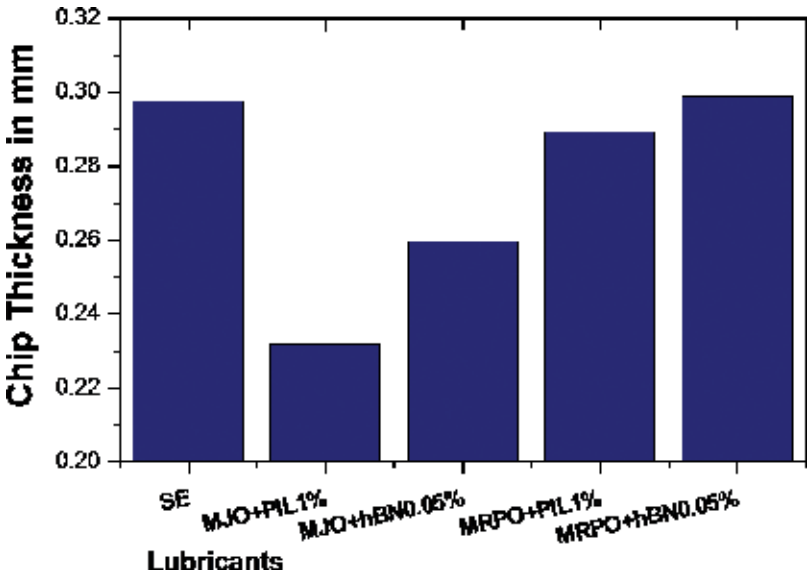

Figure 6. Result of the measured chip thickness.

comparable to the findings reported by Somers et al. [35]. They identified that the more polar IL additive has improved the properties of the polar vegetable oil. They also indicated that the ILs can form low-shear layers of anions and cations when adsorbed onto the metal surface and they can also break down to form a protective tribolayer by reacting with the exposed metal. The more polar ILs induced physical and chemical interactions with the metallic surface by adsorption at the sliding contact, thus contributing to the reduction of friction.

3.3.3. Evaluation of specific cutting energy

The calculated specific cutting energy following Eq. (2) of the orthogonal lathe machining is presented in **Figure 7**. Specific cutting energy is correlated with the energy during plastic deformation and friction [43, 48]. It indicates the amount of energy required to perform plastic deformation and overcome friction in the machining process [39]. Specific cutting energy decreases with temperature as the shear stress of the material in the shear plane decreases with the reduction of the chip thickness compression ratio [48].

It is clearly seen from **Figure 7** that the SE poses the highest cutting energy which correlates with the production of high shear stresses in the shear plane. The shear angle is also a predominant factor controlling the distribution of stresses together with the chip compression ratio and the rake angle. The lubrication characteristics of the lubricant mixtures have considerably reduced the shear stresses between metal surfaces when they were in relative motions by providing adequate lubrication film with high load carrying capacity, thus reducing the requirement of the cutting energy [43]. As mentioned earlier, the formation of tribofilm by the active end of the lubricant molecules and the additives on the metal surfaces has directly enhanced the lubrication properties on the contact zone. The complex and branched chain of TMP triester and the additive molecules caused a superior lubricity behavior and a high thermal stability which offered better tribological behavior regarding friction reduction and lower the generated thermal stresses.

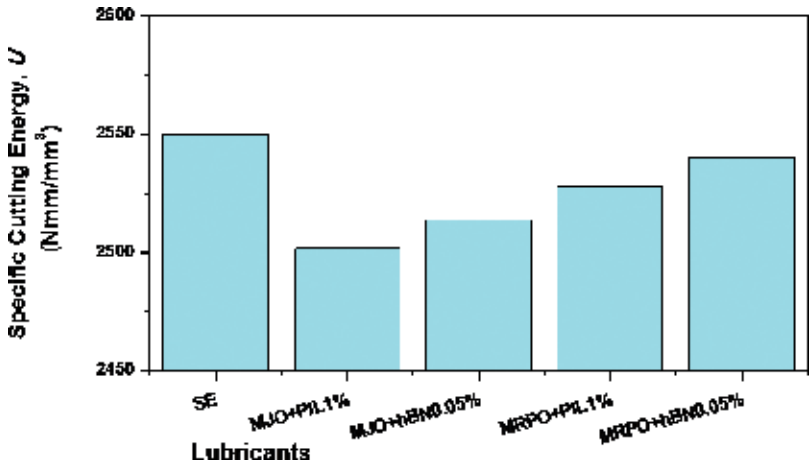

Figure 7. Specific energy of the orthogonal cutting process lubricated with all lubricant samples.

3.3.4. Evaluation of tool-chip contact length

The tool-chip contact region was analyzed underneath an optical microscope and the average contact length was measured and presented in **Figure 8**. The interaction between the metal chip and the tool rake face produces two contact regions of sticking and sliding friction during the orthogonal cutting process [43, 48]. The contact length and cutting forces are greatly influenced by the cutting lubricants applied on the cutting zone. The total contact length, L_c has been reported to depend most strongly on the deformed chip thickness h_c and proportional to the product of the chip thickness and the effective friction coefficient. Here, the lubrication effect by using different MQL lubricant mixtures had improved the tool/chip contact

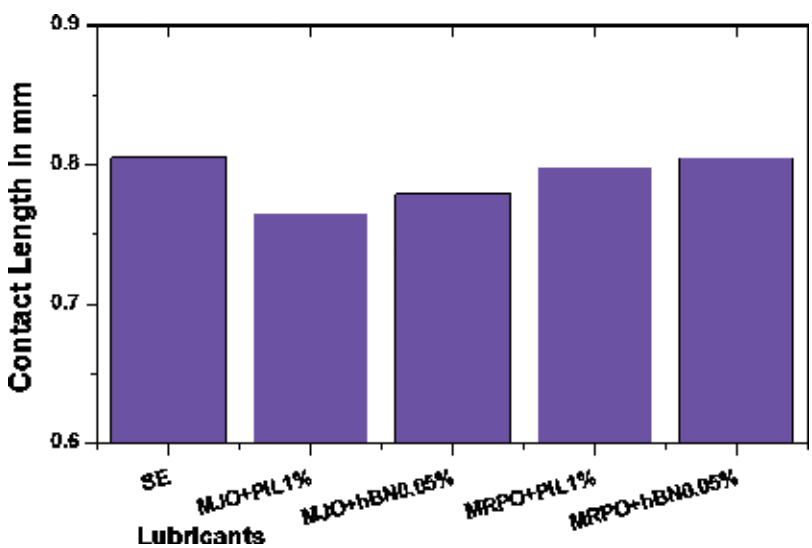

Figure 8. Results of the measured tool-chip contact length.

length compared to the surface lubricated with SE. It was clearly seen that the various types of the metalworking fluids clearly affected the tool-chip contact length. The poor lubrication effect of the SE has resulted in the high frictional sticking contact with the workpiece material and produces high shear and strain stress on the cutting edge, which leads to the high frictional stress and longer contact length [39, 49].

The lubricant forms an intrinsically hydraulic wedge between the chip and the rake face of the tool insert, which may prevent seizure between the tool-chip interfaces and thus greatly lower the cutting force [48]. The addition of additives has successfully reduced the total stresses on the sticking and sliding regions during the chip formation processes [26, 36]. The tribofilm formed on the sliding surfaces acts as a wear-protected film and the lubricant spray mist penetrates to the tool cutting edge. It reduces the friction stress and subsequently shortens the tool/chip contact length and improved chip control [43, 48]. Sticking or seizure occurs at the tool edge interface and the chip then slides beyond the sticking region. The occurrence of material transfer or adhesion on the rake face indicates the material wear mechanism and the lubrication effects of different lubricant samples during the material removal process. The surface topography of the sliding region is presented in **Figure 9**.

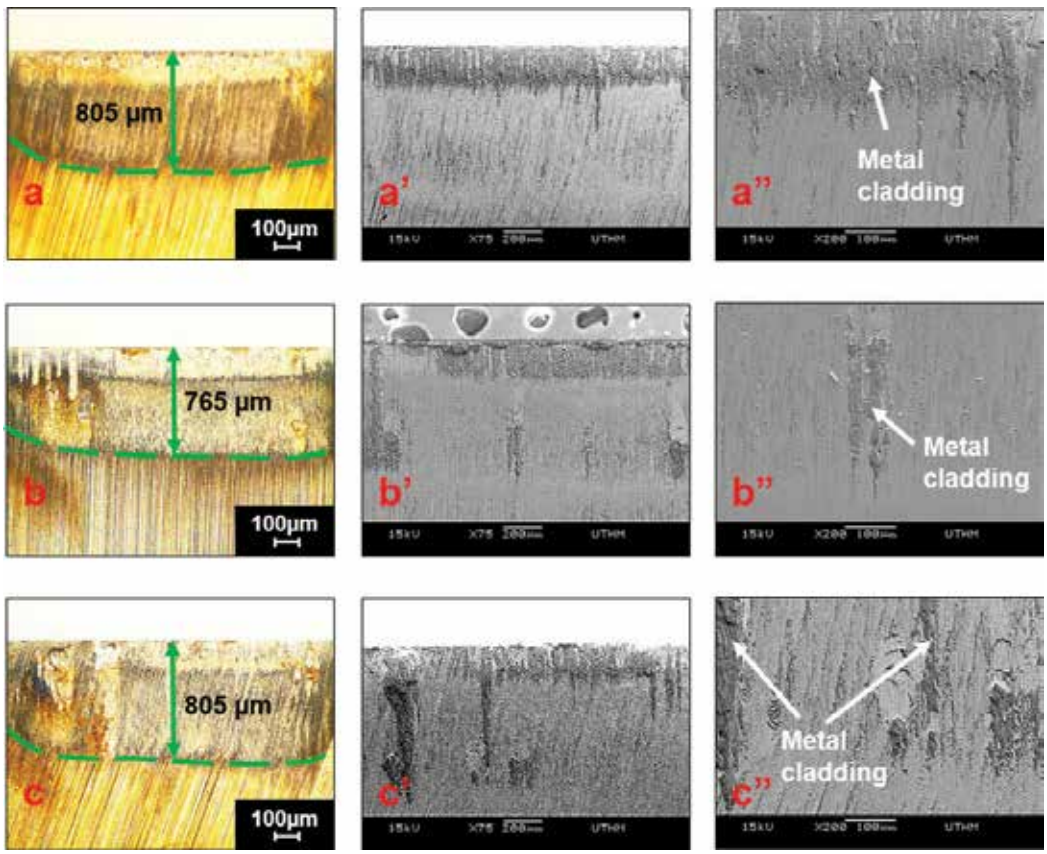

Figure 9. Optical and SEM images of the selected surface morphology on the cutting tools rake face at 50×, 75×, and 200× magnifications respectively; (a, a′, a″) SE; (b, b′, b″) MJO + PIL1% and (c, c′, c″) MRPO + hBN0.05.

The lubrication characteristics of metalworking fluids considerably reduced the friction between surfaces when they were in relative motions, thus reducing the requirement of cutting energy [48]. SE contributed to poor lubrication behavior where oxidization at high operation temperature could easily take place [18]. MRPO + hBN0.05% shows a decrement of 0.4% in specific cutting energy under the given cutting condition, while MJO + PIL1% shows superior performance with 2% improvement compared to the SE. The presence of solid additive of boron nitride particles in the vegetable base oils did help to increase the base oil performance, however, the higher adsorption rate of PIL than the hBN particles are seen to impose better lubrication effect. The poor lubrication film of the SE and MRPO + hBN0.05% was contributed by a low formation of protective layers on the contacting surfaces and also corresponds to the decreased of spray penetration into the cutting zone which leads to the direct contact of metal asperities that produces high friction between the tool and workpiece surfaces. In conclusion, the low energy required posed by the lubricant mixtures clearly proved the ability of these lubricant additives to be used as new formulations for an advanced renewable bio-based MWF from Jatropha and palm olein oils. They may become an attractive alternative to the world dominating mineral-based MWFs.

4. Conclusions

From the experimental data analyzed in this work, the following conclusions are obtained:

- The presence of polyol ester and fatty acids in the newly refined biodegradable lubricants from Jatropha and palm olein oils plays a significant importance to the tribological behavior on the metal sliding pairs in terms of wear and friction reduction. The presence of alkyl groups affects the good tribological behavior posed by the vegetable-based oils, MJO & MRPO.
- The MJO & MRPO lubricants proved to be more effective in enhancing their machining performances during the tapping torque tests and the orthogonal cutting experiments with the addition of a small quantity of an oil-miscible ionic liquid and hBN solid particles as lubricant additives.
- Good synergistic effect on the tribological and machining performance of the lubricant mixtures was shown by enhanced machining performances with improved physical properties and lubrication effects. All lubricant mixtures have shown reduced tapping torque, improved tapping efficiency, low cutting force and cutting temperature, reduced specific cutting energy and tool-chip contact length compared to the conventional synthetic ester, SE.
- The addition of phosphonium-based ionic liquid (1 wt. % PIL) into the MJO and MRPO is found to impose better lubrication ability than the addition of hBN solid particles (0.05 wt. %) in improving the tribological and machining performances of the base oils.
- The low amount of the additives used in the MJO & MRPO has great potential to be used as lubricant additives in the bio-based cutting fluids for metalworking applications.
- 'Greener' manufacturing activities by using renewable sources and low amount of biocompatible additives resulted in good energy efficiency and cleaner environment. In terms of sustainable machining operation, MJO + PIL1% & MJO + hBN0.05% are found to be a good alternative as reference for replacing the industrial dominating mineral oil-based lubricants.

Acknowledgements

The authors would like to thank the Ministry of Education Malaysia and University Tun Hussein Onn Malaysia for the financial support via Fundamental Research Grant Scheme (Vot. 1467 and Vot. 1591).

Author details

Erween Abd. Rahim*, Amiril Sahab Abdul Sani and Norfazillah Talib

*Address all correspondence to: erween@uthm.edu.my

Precision Machining Research Center (PREMACH), Faculty of Mechanical and Manufacturing Engineering, Universiti Tun Hussein Onn Malaysia, Batu Pahat, Johor, Malaysia

References

[1] Erhan SZ, Sharma BK, Perez JM. Oxidation and low temperature stability of vegetable oil-based lubricants. Industrial Crops and Products. 2006;**24**:292-299

[2] Nicol A, Hurrell AC. Exploring knowledge translation in occupational health using the mental models approach: A case study of machine shops. Proceedings of the European Safety and Reliability Conference. 2008;**1**:749-756

[3] Lawal SA, Choudhury IA, Nukman Y. Application of vegetable oil-based metalworking fluids in machining ferrous metals–A review. International Journal of Machine Tools and Manufacture. 2012;**52**:1-12

[4] Mang T, Dresel W. Lubricants and Lubrication. 2nd ed. Weinheim, Germany: WILEY-VCH Verlag GmbH & Co. KGaA; 2007. 890 p

[5] Skerlos SJ, Hayes KF, Clarens AF. Current advances in sustainable metalworking fluids research. International Journal of Sustainable Manufacturing. 2008;**1**:180-202

[6] Belluco W, Chiffre L. Performance evaluation of vegetable-based oils in drilling austenitic stainless steel. Journal of Materials Processing Technology. 2004;**148**:171-176

[7] Kuram E, Ozcelik B, Simsek BT, Demirbas E. The effect of extreme pressure added vegetable based cutting fluids on cutting performance in milling. Industrial Lubrication and Tribology. 2013;**65**(3):181-193. DOI: 10.1108/00368791311311187

[8] Rahim EA, Sasahara H. A study of the effect of palm oil as MQL lubricant on high speed drilling of titanium alloys. Tribology International. 2011;**44**:309-317

[9] Jayadas NH, Nair KP, Ajithkumar G. Tribological evaluation of coconut oil as an environment-friendly lubricant. Tribology International. 2007;**40**:350-354

[10] Brinksmeier E, Meyer D, Huesmann-Cordes AG, Herrmann C. Metalworking fluids–Mechanisms and performance. CIRP Annals–Manufacturing Technology. 2015;**64**:605-628

[11] Vasu V, Reddy PKG. Effect of minimum quantity lubrication with Al2O3 nanoparticles on surface roughness, tool wear and temperature dissipation in machining Inconel 600 alloy. Proceedings of the Institution of Mechanical Engineers, Part N: Journal of Nanoengineering and Nanosystems. 2011;**225**:3-16

[12] Reeves CJ, Menezes PL. Advancements in eco-friendly lubricants for tribological applications: Past, present, and future. In: Davim JP, editor. Ecotribology. Switzerland: Springer International Publishing; 2016. p. 41-61

[13] Zhang Y, Li C, Jia D, Zhang D, Zhang X. Experimental evaluation of MoS_2 nanoparticles in jet MQL grinding with different types of vegetable oil as base oil. Journal of Cleaner Production. 2015;**87**:930-940

[14] Li B, Li C, Zhang Y, Wang Y, Yang M, Jia D, Zhang N, Wu Q. Effect of the physical properties of different vegetable oil-based nanofluids on MQLC grinding temperature of Ni-based alloy. International Journal of Advanced Manufacturing Technology. 2016;**89**:3459-3474

[15] Nam JS, Lee PH, Lee SW. Experimental characterization of micro-drilling process using nanofluid minimum quantity lubrication. International Journal of Machine Tools and Manufacture. 2011;**51**:649-652

[16] Nguyen TK, Do I, Kwon P. A tribological study of vegetable oil enhanced by nano-platelets and implication in MQL machining. International Journal of Precision Engineering and Manufacturing. 2012;**13**:1077-1083

[17] Abdullah MIHC, Abdollah MF, Amiruddin H, Tamaldin N, Nuri NRM, Hassan M, Rafeq SA. Improving engine oil properties by dispersion of hBN/Al_2O_3 nanoparticles. Applied Mechanics and Materials. 2014;**607**:70-73

[18] Talib N, Nasir RM, Rahim EA. Tribological behaviour of modified jatropha oil by mixing hexagonal boron nitride nanoparticles as a bio-based lubricant for machining. Journal of Cleaner Production. 2017;**147**:360-378

[19] Bermudez M-D. Introduction to the ionic liquids special issue. Tribology Letters. 2010; **40**(2):213. DOI: 10.1007/s11249-010-9707-0

[20] Amiril SAS, Rahim EA, Syahrullail S. A review on ionic liquids as sustainable lubricants in manufacturing and engineering: Recent research, performance, and applications. Journal of Cleaner Production. 2017;**168**:1571-1589. DOI: 10.1016/j.jclepro.2017.03.197

[21] Chetan SGP, Rao V. Application of sustainable techniques in metal cutting for enhanced machinability: A review. Journal of Cleaner Production. 2015;**100**:17-34. DOI: 10.1016/j.jclepro.2015.03.039

[22] Zhang L, Feng D, Bin X. Tribological characteristics of alkylimidazolium diethyl phosphates ionic liquids as lubricants for steel–steel contact. Tribology Letters. 2009;**34**(2): 95-101. DOI: 10.1007/s11249-009-9412-z

[23] Cai Z-b, Meyer HM, Ma C, Chi M, Luo H, Jun Q. Comparison of the tribological behavior of steel–steel and Si3N4–steel contacts in lubricants with ZDDP or ionic liquid. Wear 2014;**319**(1-2):172-183. DOI: 10.1016/j.wear.2014.08.002

[24] Hernández Battez A, Blanco D, Fernández-González A, Mallada MT, González R, Viesca JL. Friction, wear and tribofilm formation with a [NTf2] anion-based ionic liquid as neat lubricant. Tribology International. 2016; **103**(November 2016):73-86. DOI: 10.1016/j.triboint.2016.06.038

[25] Anand M, Hadfield M, Viesca JL, Thomas B, Hernández Battez A, Austen S. Austen. Ionic liquids as tribological performance improving additive for in-service and used fully-formulated diesel engine lubricants. Wear 2015;**334-335**:67-74. DOI: 10.1016/j.wear.2015.01.055

[26] Zhu L, Zhao Q, Wu X, Zhao G, Wang X. A novel phosphate ionic liquid plays dual role in synthetic ester oil: From synthetic catalyst to anti-wear additive. Tribology International. 2016;**97**(May 2016):192-199. DOI: 10.1016/j.triboint.2015.12.047

[27] Qu J, Truhan JJ, Dai S, Luo H, Blau PJ. Ionic liquids with ammonium cations as lubricants or additives. Tribology Letters. 2006;**22**(3):207-214. DOI: 10.1007/s11249-006-9081-0

[28] Palacio BB. A review of ionic liquids for green molecular lubrication in nanotechnology. Tribology Letters. 2010;**40**(2):247-268. DOI: 10.1007/s11249-010-9671-8

[29] Yu B, Bansal DG, Qu J, Sun X, Luo H, Dai S, Blau PJ, Bunting BG, Mordukhovich G, Smolenski DJ. Oil-miscible and non-corrosive phosphonium-based ionic liquids as candidate lubricant additives. Wear 2012;**289**:58-64. DOI: 10.1016/j.wear.2012.04.015

[30] González R, Bartolomé M, Blanco D, Viesca JL, Fernández-González A, Hernández Battez A. Effectiveness of phosphonium cation-based ionic liquids as lubricant additive. Tribology International. 2016;**98**:82-93. DOI: 10.1016/j.triboint.2016.02.016

[31] Amiril SAS, Rahim EA, Talib N, Kamdani K, Rahim MZ, Syahrullail S. Performance evaluation of palm- olein TMP ester containing hexagonal boron nitride and an oil miscible ionic liquid as bio-based metalworking fluids. Journal of Mechanical Engineering. 2017;**SI 4**(1):223-234

[32] Pham M-Q, Yoon H-S, Khare V, Ahn S-H. Evaluation of ionic liquids as lubricants in micro milling–Process capability and sustainability. Journal of Cleaner Production. 2014;**76**:167-173. DOI: 10.1016/j.jclepro.2014.04.055

[33] Davis B, Schueller JK, Huang Y. Study of ionic liquid as effective additive for minimum quantity lubrication during titanium machining. Manufacturing Letters. 2015;**5**:1-6. DOI: 10.1016/j.mfglet.2015.04.001

[34] Goindi GS, Sarka P, Jaya AD, Chavan SN, Mandal D. Investigation of ionic liquids as additives to canola oil in minimum quantity lubrication milling of plain medium carbon steel. International Journal of Advanced Manufacturing Technology. 2017. DOI: 10.1007/s00170-017-0970-1

[35] Somers AE, Khemchandani B, Howlett PC, Sun J, MacFarlane DR, Forsyth M. Ionic liquids as anti-wear additives in base oils: Influence of structure on miscibility and wear

performance for steel on aluminium. ACS Applied Materials & Interfaces. 2013;**5**(22): 11544-11553. DOI: 10.1021/am4037614

[36] Zhu L, Zhao G, Wang X. Investigation on three oil-miscible ionic liquids as antiwear additives for polyol esters at elevated temperature. Tribology International. 2017;**109** (May 2017):336-345. DOI: 10.1016/j.triboint.2016.10.032

[37] Zhou Y, Jun Q. Ionic liquids as lubricant additives: A review. ACS Applied Materials & Interfaces. 2017;**9**(4):3209-3222. DOI: 10.1021/acsami.6b12489

[38] Hernández Battez A, Bartolomé M, Blanco D, Viesca JL, Fernández-González A, González R. González. Phosphonium cation-based ionic liquids as neat lubricants: Physicochemical and tribological performance. Tribology International. 2016;**95**:118-131. DOI: 10.1016/j.triboint.2015.11.015

[39] DeVries WR. Analysis of Material Removal Processes. 1st ed. USA: Springer-Verlag; 1992. 254 p. DOI: 10.1007/978-1-4612-4408-0

[40] Bart JCJ, Gucciardi E, Cavallaro S. Advanced lubricant fluids. In: Bart JCJ, Gucciardi E, Cavallaro S, editors. Biolubricants: Science and Technology. Cambridge: Woodhead Publishing Limited; 2013. pp. 824-846

[41] Shashidhara YM, Jayaram SR. Vegetable oils as a potential cutting fluid—An evolution. Tribology International. 2010;**43**:1073-1081

[42] Arbain NH, Salimon J. The effects of various acid catalyst on the esterification of jatropha curcas oil based trimethylolpropane ester as biolubricant base stock. Journal of Chemistry. 2011;**8**:33-40

[43] Stephenson DA, Agapiou JS. Metal Cutting Theory and Practice. 3rd ed. USA: CRC Press; 2016. p. 947

[44] Syahrullail S, Izhan MI. Tribological investigation of RBD palm olein in different sliding speeds using pin-on-disk tribotester. Scientia Iranica. 2014;**21**:162-170

[45] Salimon J, Abdullah BM, Yusop RM, Salih N. Synthesis, reactivity and application studies for different biolubricants. Chemistry Central Journal. 2014;**8**:1-11

[46] Minami I. Molecular science of lubricant additives. Applied Sciences. 2017;**7**:1-33

[47] Qu J, Bansal DG, Yu B, Howe JY, Luo H, Dai S, Li H, Blau PJ, Bunting BG, Mordukhovich G, Smolenski DJ. Antiwear performance and mechanism of an oil-miscible ionic liquid as a lubricant additive. ACS Applied Materials & Interfaces. 2012;**4**(2):997-1002. DOI: 10.1021/am201646k

[48] Grzesik W. Advanced Machining Processes of Metallic Materials–Theory, Modelling and Applications. 1st ed. Amsterdam, Netherlands: Elsevier; 2008. 472 p

[49] Trent EM, Wright PK. Metal Cutting. 4th ed. Oxford, United Kingdom: Elsevier Science & Technology; 2000. 464 p

Chapter 4

Evaluation of the Biotribological Behavior and Cytotoxicity of Laser-Textured ISO 5832-1 Stainless Steel for Use in Orthopedic Implants

Eurico Felix Pieretti, Andrea Cecília Dorión Rodas, Renato Altobelli Antunes and Maurício David Martins das Neves

Additional information is available at the end of the chapter

http://dx.doi.org/10.5772/intechopen.73140

Abstract

This chapter evaluated the influence of laser texturing process on the tribological behavior of the ISO 5832-1 austenitic stainless steel (SS). The friction coefficient and wear were determined using ball-cratering wear tests. The laser texturing process was carried out with a nanosecond optical fiber ytterbium laser at four different pulse frequencies. Cytotoxicity tests were carried out to determine if laser texturing affects the biomaterial biocompatibility. For comparison reasons, pristine surfaces were also evaluated. The results indicated that the wear volume and friction coefficient were reduced after laser texturing. The samples were considered noncytotoxic according to the biocompatibility tests as the laser texturing process did not decrease cell's viability.

Keywords: biomaterials, cytotoxicity, laser texturing, stainless steel, tribology

1. Introduction

Implantable medical devices used in mobile joints of the human body as well as for dental purposes require biocompatibility with the surrounding tissues and organs, mechanical strength, and corrosion resistance. The body fluids constitute a hostile environment for the implant, which is also subjected to various loads. The implant can release particles due to corrosion, corrosion associated with fatigue, and even friction against implantable components, bones, or other body parts. By coming into contact with the body fluids, these particles can be placed in locations far from the removed source causing complications to the patients.

Okasaki [1] evaluated the properties of metallic biomaterials with regard to the effect of friction on anodic polarization. He observed that corrosion was accelerated in the frictional environment with respect to static conditions. This effect was due to the formation of anodic areas in the stressed regions under friction whereas its periphery is cathodic.

Metallic particles released from the corrosion process may move passively, through tissue and/or circulatory system or can be transported in an active way when metabolized by macrophages [2]. In either case, this mass transport may lead to debris accumulation in surrounding tissues or even remote sites where they can participate in undesirable biological reactions, compromising biomaterial's biocompatibility.

Interaction between metallic implants and the human body can be affected by numerous factors such as the structure of the metal surface, its mechanical properties, size, and shape. When in contact with the body tissues after implantation, metallic devices affect the intensity of stresses to which the whole human body is subjected as well the implant itself. Wear and corrosion processes are additional effects arising from the interaction between metallic biomaterials and the body tissues [3].

The orthopaedic implants are projected and manufactured so that when used under the conditions and for the purposes designed, without compromising the clinical condition or the safety of patients. Any risks that may be associated with the implants use are acceptable when compared to benefits for the patients [2, 3].

The alloy described in part 1 of ISO 5832 [4] (ASTM F138/ASTM F139) is an austenitic stainless steel. It is one of the metallic materials most used in Brazil for manufacturing implants, because of its suitable mechanical strength, reasonable corrosion resistance, and low cost [5–8]. Stainless steel implantable medical devices are used as permanent or temporary implants to help bone healing. The laser texturing process is used to modify the biomaterial surface roughness and hardness.

The microscale abrasion test (or ball-cratering wear test) is a practical method to analyze the wear resistance of materials [8–11]. The ball-cratering wear test has gained large acceptance at universities and research centers and is widely used in studies focusing on the abrasive wear behavior of different materials [12–16]. **Figure 1** presents a schematic diagram of the principle of this wear test, where a rotating ball is forced against the specimen being tested and an

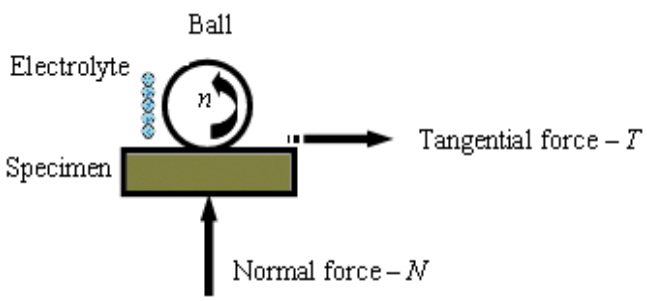

Figure 1. Schematic representation of the operating principle of ball-cratering wear test.

electrolyte is supplied between the ball and the specimen during the experiments. The aim of the ball-cratering wear test is to generate "wear craters" on the specimen surfaces. The wear volume (V) may be determined as a function of b, using Eq. (1) [12], where b is the wear crater diameter and R is the ball radius.

$$V \cong \frac{\pi b^4}{64R} \text{ for } b << R \quad (1)$$

Wear tests conducted under the ball-cratering technique present advantages in relation to other types of tests, because it can be performed with normal forces (N) and rotations of the sphere (n) relatively low (N < 0.5 N and n < 80 rpm) [17–21]. Tests in micro- and nanotribometers are used to investigate small regions and thin layers of different surfaces [22, 23].

The aim of this work was to evaluate the cytotoxicity and the tribological behavior of ISO 5832-1 austenitic stainless steel (SS) textured by Yb optical fiber laser, varying its pulse frequency, using two ball-cratering wear methods.

2. Experimental

2.1. Material and sample preparation

The material employed in the present work was a round bar (15 mm diameter) of the ISO 5832-1 austenitic stainless steel (chemical composition in wt%: 0.023 C, 0.78 Si, 2.09 Mn, 0.026 P, 0.0003 S, 18.32 Cr, 2.59 Mo, 14.33 Ni, and Fe balance). Specimens were treated with a nanosecond ytterbium (Yb) optical fiber laser at four different pulse frequencies, as shown in **Table 1**. A pulsed Nd: YAG laser (TRUMARK 5050™) was operated at a wavelength of 1062 ± 3 nm, with a laser average power of 50 W and a scanning speed of 200 mm s^{-1}. **Figure 2** shows the surface finish of the laser-textured specimens.

2.2. Ball-cratering wear test

An instrument with free-ball configuration was used for the sliding wear tests. Two load cells were used in the ball-cratering apparatus: one load cell to control the normal force (N) and one load cell to measure the tangential force (T) developed during the experiments. "Normal" and "tangential" load cells had a maximum capacity of 50 N and an accuracy of 0.001 N. The values of "N" and "T" were registered by a readout system. **Table 2** presents the test conditions selected for the experiments conducted in this work. Balls for the ball-cratering wear test were made of AISI 316L stainless steel, with a diameter of D = 25.4 mm (D = 1″). A phosphate buffer solution (PBS), with chemical composition (g/l): 8.0 NaCl, 0.2 KCl, 1.15 Na_2HPO_4, 0.2 KH_2PO_4, with a pH value of 7.4 and a conductivity of 15.35 mS was dropped between the ball and the specimen.

Specimens	1	2	3	4
Frequencies (kHz)	80	188	296	350

Table 1. Frequencies used for ytterbium optical fiber laser treatment.

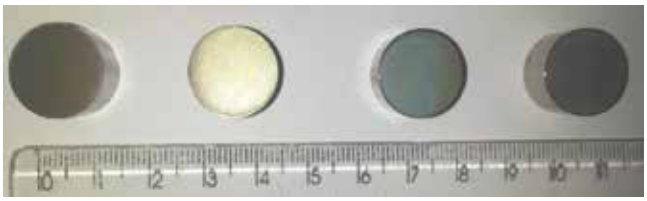

Figure 2. ISO 5832-1 austenitic stainless steel textured by ytterbium optical fiber laser.

Test condition	
(N) Normal force (N)—ball of AISI 316 L SS	0.25
(S) Sliding distance—(m)	8.0
(n) Ball rotational speed—(rpm)	50
(v) Tangential sliding velocity—(m/s)	0.1
(t) Test duration—(min)	10

Table 2. Test conditions selected for the ball-cratering wear experiments.

The values of normal force (N) were defined as a function of the density (ρ) of the ball material (AISI 316 L SS): $\rho_{316L} = 8\ g \cdot cm^{-1}$.

The tests were conducted at t = 10 min. The sliding distance (S) was calculated based on the values of $v = 0.1\ m \cdot s^{-1}$ and t = 10 min (t = 600 s) and was equal to 60 m.

All experiments were conducted without interruption, and the PBS solution was continuously agitated and fed between the ball and the specimen under a frequency of 1 drop/2 s. Both the normal force (N) and the tangential force (T) were monitored and registered constantly. Then, the friction coefficient (μ) was determined using Eq. 2:

$$\mu = \frac{T}{N} \tag{2}$$

2.3. Nanotribometer

The tribological behavior of the ISO 5832-1 austenitic stainless steel was also assessed by wear tests conducted in a nanotribometer (Anton Paar—model NTR²). The tests were performed in the air, at 25°C, with counterbody of chrome steel 52–100 rotating ball shape, 2 mm in diameter, during 10 min, with normal force of 100.0 mN, distance equivalent to 2.4 m, and a scan speed of 4.0 $cm.s^{-1}$. Both laser-textured and pristine materials were evaluated.

2.4. Microhardness (HV)

Vickers microhardness analyses were performed in a microdurometer coupled with optical microscope, Fisherscope HM 2000. The hardness values refer to the average of five measurements at a distance of 50 μm between each indentation, and applied load of 25.0 $mN \cdot 0^{-1}$, for surfaces treated with laser and also for the untreated stainless steel specimens.

2.5. Roughness analysis

A LEXT OLS 4100 confocal laser scanning microscope (Olympus, TM) was used in order to obtain the surface roughness of the laser-textured and untreated samples with a higher definition quality in the topographic analysis. The values are expressed as the mean roughness Ra.

2.6. Cytotoxicity analysis

Cytotoxicity was assessed by quantitative methodology. The test is based on the determination of viable cells after exposure of the cell population to the extract obtained from incubation of the samples in cell culture medium RPMI (Gibco®) supplemented with serum bovine fetal 10% and antibiotic/antimycotic (solution Gibco®) 1% at 37°C for 9 days under constant gentle stirring. The long period use was chosen to mimic if the samples were implanted. The treated surface was carefully immersed in cell culture medium to evaluate if there was debris released from the samples that can lead to a cytotoxicity effect. The extract of each sample were used to cultivate on a cell monolayer, CHO (Chinese Hamster Ovarian) cell line for 24 hours.

The analysis of the number of viable cells was performed by the colorimetric method for the metabolization of *supravital* dye, MTS, and the electron coupling agent, PMS (Promega®) were used as the supplier instructions, and subsequently reading in a spectrophotometer at 490 nm. The amount of dye metabolized by the cell population is directly proportional to the number of viable cells on the plate.

3. Results and discussion

3.1. Wear volume analysis

The environment of implants usually induces wear deriving from the contact between the biomaterial and surrounding tissues, so that when manufacturing an implant, one has to choose a suitable area for laser treatment. **Figure 3** shows this biomaterial surface without texturizations (blank).

Figure 4 presents the wear volumes (V) for the untreated and laser-textured samples after the ball-cratering wear tests. These values were determined according to Eq. (1). It is possible to observe that the wear volume decreased for the laser-textured specimens with respect to the untreated steel. This fact is likely to be associated with an increase in the surface hardness after laser texturing. As shown in **Table 3**, the microhardness of the laser-textured samples was higher than that of the untreated material. The highest values of wear volume were obtained for the untreated specimens. The wear resistance of the laser-textured surfaces was superior to that of the pristine material. Similar results were reported by Cozza et al. [13] using the same test for a different tribological system.

Microstructural and topographic modifications due to changes in some parameters of the laser beam were identified by Lima et al. [24]. They used a Q-switched Nd: YAG laser with different pulse frequencies. Similarly, they performed texturing treatment that consisted of

Figure 3. Wear test conducted on the ISO 5832-1 SS without laser treatment. Ball of AISI 316 L SS.

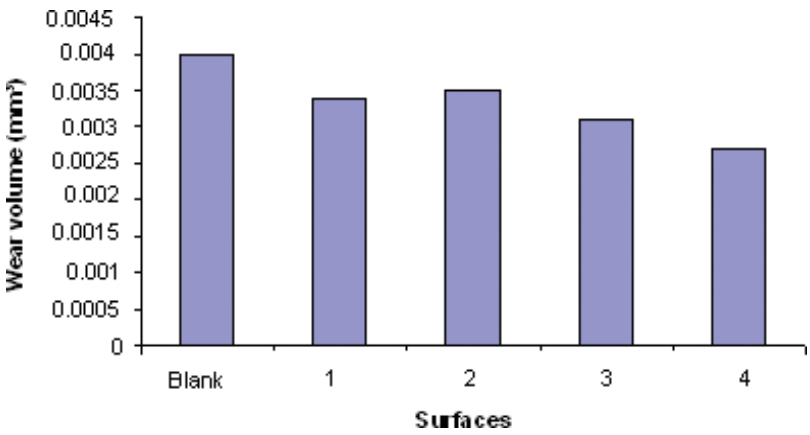

Figure 4. Wear volumes of the untreated and laser-textured surface determined after the ball-cratering wear tests.

juxtaposed lines on the surface of the AISI M2 tool steel. Changes in beam energies and intensities were observed. All conditions used produced metal fusion. They noticed that there was little roughness for the low intensities generated by the laser beam; however, there were "craters", that is, regions with high roughness at the higher intensities.

Allsopp and Hutchings [25] have suggested that surface roughness is interesting for improving adhesion between coatings and metallic alloys, and can be produced and controlled by laser beam. This effect is desirable on some biomaterials' surfaces for permanent fixture medical devices. The values of Ra shown in **Table 3** reveal that the average roughness increased after laser texturing, scaling up with the pulse frequency.

Specimens	**Blank**	**1**	**2**	**3**	**4**
Microhardness (HV)	199.3	204.3	215.4	226.1	239.9
Ra (μm)	0.2	1.5	5.2	9.2	11.5

Table 3. Microhardness and roughness values for the untreated and laser-textured samples.

3.2. Friction coefficient

Because wear is a surface phenomenon that occurs at the interface between the asperities of the surfaces in contact, biotribology results are strongly influenced by the surface finish produced by the laser beam texturing.

Considering the ball-cratering wear test, the highest value of the friction coefficient was obtained for the untreated surface as shown in **Figure 5**. The laser-textured specimens presented lower friction coefficient. The lowest value was observed for specimen 3. There was no apparent relationship between the friction coefficient and the laser pulse frequency. Notwithstanding, it is possible to infer that the hardness increase can be related to this effect. Surface roughness, in turn, did not increase the friction coefficient, being the hardness effect more prominent to the friction characteristics of the treated surface. Values of such magnitudes were reported in literature [25–28], with the same type of test under different tribological systems.

In the biomaterials' field for implantable medical or dental devices, tribological assays are of great value in providing an estimate of the normal, tangential, and frictional forces in relation to the volume of material that can be detached from the surface, migration, and accommodation of some particles.

This work also analyzed the evolution of the friction coefficient by nanotribometer wear tests of the surfaces of these biomaterials with laser texturing treatment. The results obtained are presented in **Figure 6**, and are compared with the blank specimen (without treatment).

No direct relationship between wear volume and friction coefficient was observed; i.e., the highest value of wear volume was not related to the higher value of coefficient of friction [25–28].

The variation of the friction coefficient with the test time is shown in **Figure 6** for the laser-textured and untreated samples. These results were obtained by means of the wear tests conducted in the nanotribometer. For the laser-textured surfaces, the values of friction coefficient were lower than those obtained for untreated surface, confirming the results of the ball-cratering wear test.

For the laser-textured surfaces, **Figure 6**, the values of friction coefficient obtained were lower than those obtained in the samples without treatment by the laser beam (blank).

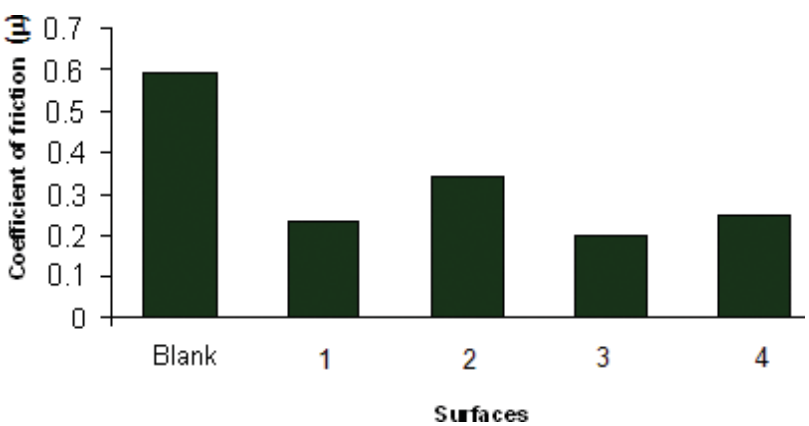

Figure 5. Friction coefficient obtained by the ball-cratering wear test for untreated and textured specimens.

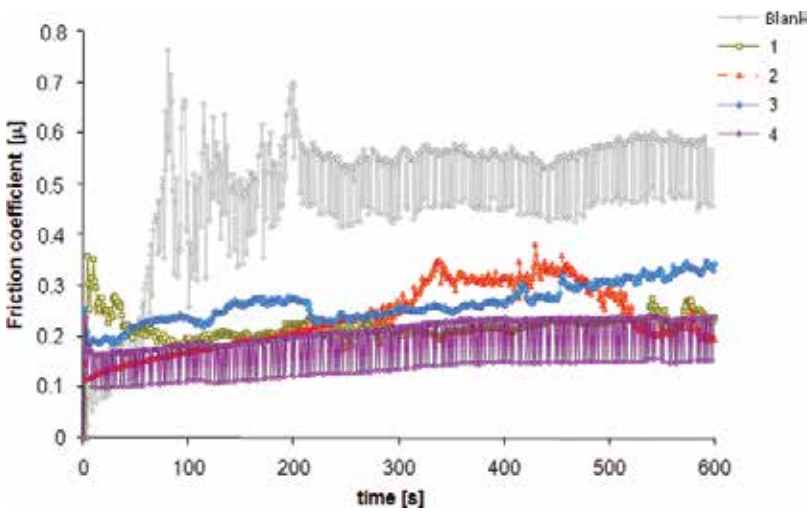

Figure 6. Variation of friction coefficient as a function of the test time for the laser-textured and -untreated specimens.

The friction coefficient values for the untreated specimen showed a rapid increase in the beginning of the test (running-in), and practically stabilized around values close to $\mu = 0.5$ as the surface becomes less rough. In the case of the laser-textured samples, the friction coefficient decreases up to 100 s, reaching a stabilization period up to the end of the test. For sample 2, the friction coefficient initially presented gradual increase up to 500 s reaching 0.35 and then drops to less than 0.2 at the end of the test. Sample 3 showed a tendency of continuous increment of the friction coefficient with time. For sample 4, in turn, it remained practically constant and at lower than that of the other conditions.

The effect of the variation of the coefficient of friction as a function of the test time was studied by Huang et al. [29]. They verified some tribological properties of Ti-6Al-4 V alloys with and without coating ("laser clad"), for a period of 3500 s in different rotation frequencies, and at the end of the tests, they verified that the coefficient of friction for the coatings was always inferior to the substrate.

3.3. Cytotoxicity analysis

The results presented in **Figure 7** indicate that the austenitic ISO 5832-1 SS exhibited cytotoxic behavior similar to the negative control, that is, it shows no cytotoxicity. This is indicated by the cell viability curve for the laser-treated samples above the level $IC_{50\%}$ of cytotoxicity. **Table 4** shows the pH of the extracts at a concentration of 100%.

The cytotoxicity of the ISO 5832-1 stainless steel was evaluated in the present study according to ISO 10993-5 [30]. The absence of cytotoxicity is desired for stainless steels for medical and dental applications [31]. The slight decrease in the cell viability for the laser-treated samples

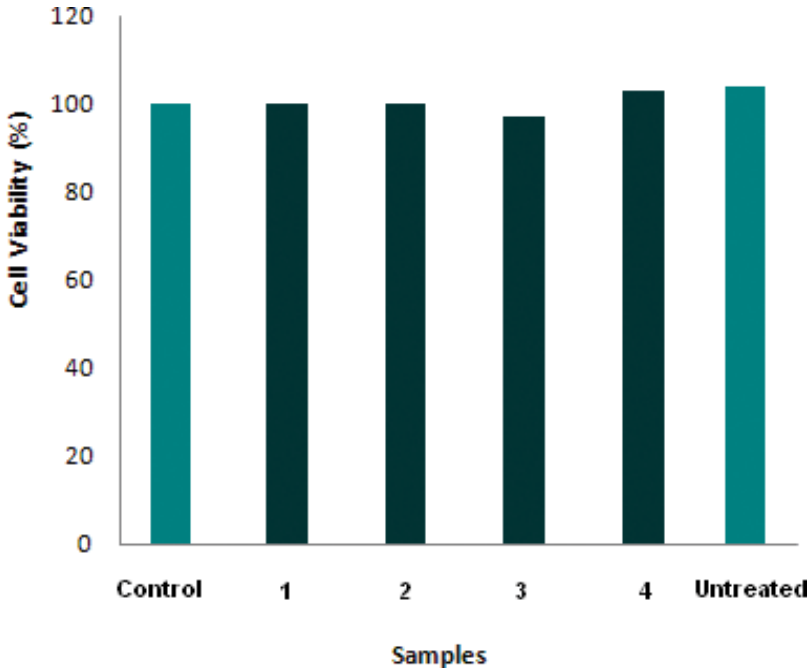

Figure 7. Cell viability as a function of the extract concentration of the laser-textured and untreated samples.

Extracts	pH
Control (Pure Ti)	7.50
ISO 5832-1 SS treated by laser	7.88

Table 4. Values of pH for the extracts at a concentration of 100%.

is explained by its susceptibility to localized corrosion [5, 6, 32, 33]. According to Pieretti and Costa [5], the laser process affects the corrosion resistance of the laser-treated stainless steel biomaterials, producing a less protective passive film with areas prone to its breakdown, although the samples are not considered cytotoxic.

Studies on the biomaterials tribological behavior are important because they reveal unique aspects about the surface wear mechanisms [34]. The knowledge of wear response contributes to the understanding of other surface phenomena, which can occur simultaneously and potentiate one another, such as the phenomenon of corrosion.

The occurrence of both concomitantly can lead to acceleration of particle detachment, including nonmetallic inclusions that may be housed under biomaterial surface [35], and these may come into contact with the bloodstream and lodge in any part of the human body causing, many times, harm to the patients.

4. Conclusions

In this work, surface texturing of ISO 5832-1 stainless steel samples was carried out using an optical fiber Yb laser. The effect of the laser pulse frequency on the tribological behavior of the treated steel was evaluated by ball-cratering wear tests and sliding wear tests using a nano-tribometer. The wear volume determined from the ball-cratering wear test points out that the laser-textured surfaces were more resistant to wear, presenting lower wear volumes than the untreated material. The friction coefficient decreased after laser texturing likely due to the increased surface hardness of the laser-treated samples as revealed by Vickers microhardness measurements. This effect was observed for the wear tests conducted with the ball-cratering apparatus and the nanotribometer. The laser texturing process did not impart any cytotoxicity to the ISO 5832-1 samples, preserving the biocompatibility of the pristine surface.

Acknowledgements

The authors acknowledge CNPq for the financial support, under grant number Process: 350798/2014-1, Project: 459565/2013-3, and Dr. R. C. Cozza.

Author details

Eurico Felix Pieretti[1]*, Andrea Cecília Dorión Rodas[2], Renato Altobelli Antunes[2] and Maurício David Martins das Neves[1]

*Address all correspondence to: efpieretti@usp.br

1 Nuclear and Energy Research Institute (IPEN-CNEN), São Paulo, SP, Brazil

2 Federal University of ABC (UFABC), Santo André, SP, Brazil

References

[1] Okasaki Y. Effect of friction on anodic polarization properties of metallic biomaterials. Biomaterials. 2002;**23**:2071-2077

[2] Black J. Systemic effects of biomaterials. Biomaterials. 1984;**5**:11-18

[3] Anderson JM. Biological response to materials. Annual Review of Materials Research. 2001;**31**:81-110

[4] ISO 5832-1:2016, Implants for Surgery - Metallic Materials - Part 1: Wrought Stainless Steel

[5] Pieretti EF, Costa I. Surface characterisation of ASTM F139 stainless steel marked by laser and mechanical techniques. Electrochimica Acta. 2013;**114**:838-843

[6] Pieretti EF, Manhabosco SM, Dick LFP, Hinder S, Costa I. Localized corrosion evaluation of the ASTM F139 stainless steel marked by laser using scanning vibrating electrode technique, X-ray photoelectron spectroscopy and Mott-Schottky techniques. Electrochimica Acta. 2014;**124**:150-155

[7] Pieretti EF, Palatnic RP, Leivas TP, Costa I, Neves MDM. Evaluation of laser marked ASTM F 139 stainless steel in phosphate buffer solution with albumin. International Journal of Electrochemical Science. 2014;**9**:2435-2444

[8] Pieretti EF, Costa I, Marques RA, Leivas TP, Neves MDM. Electrochemical study of a laser marked biomaterial in albumin solution. International Journal of Electrochemical Science. 2014;**9**:3828-3836

[9] Adachi K, Hutchings IM. Wear-mode mapping for the micro-scale abrasion test. Wear. 2003;**255**:23-29

[10] Stachowiak GB, Stachowiak GW, Celliers O. Ball-cratering abrasion tests of high-Cr white cast irons. Tribology International. 2005;**38**:1076-1087

[11] Stachowiak GB, Stachowiak GW, Brandt JM. Ball-cratering abrasion tests with large abrasive particles. Tribology International. 2006;**39**:1-11

[12] Rutherford KL, Hutchings IM. Theory and application of a micro-scale abrasive wear test. Journal of Testing and Evaluation - JTEVA. 1997;**25**(2):250-260

[13] Cozza RC, Tanaka DK, Souza RM. Friction coefficient and abrasive wear modes in ball-cratering tests conducted at constant normal force and constant pressure – Preliminary results. Wear. 2009;**267**:61-70

[14] Cozza RC, de Mello JDB, Tanaka DK, Souza RM. Relationship between test severity and wear mode transition in micro-abrasive wear tests. Wear. 2007;**263**:111-116

[15] Cozza RC. Influence of the normal force, abrasive slurry concentration and abrasive wear modes on the coefficient of friction in ball-cratering wear tests. Tribology International. 2014;**70**:52-62

[16] Trezona RI, Allsopp DN, Hutchings IM. Transitions between two-body and three-body abrasive wear: Influence of test conditions in the microscale abrasive wear test. Wear. 1999; **225**-**229**:205-214

[17] Cozza RC, Tanaka DK, Souza RM. Friction coefficient and wear mode transition in micro-scale abrasion tests. Tribology International. 2011;**44**:1878-1889

[18] Cozza RC. A study on friction coefficient and wear coefficient of coated systems submitted to micro-scale abrasion tests. Surface & Coatings Technology. 2013;**215**:224-233

[19] Bose K, Wood RJK. Optimum tests conditions for attaining uniform rolling abrasion in ball cratering tests on hard coatings. Wear. 2005;**258**:322-332

[20] Axén N, Jacobson S, Hogmark S. Influence of hardness of the counterbody in three-body abrasive wear – An overlooked hardness effect. Tribology International. 1994;**27**(4):233-241

[21] Gee MG, Wicks MJ. Ball crater testing for the measurement of the unlubricated sliding wear of wear-resistant coatings. Surface and Coatings Technology. 2000;**133-134**:376-382

[22] Sun D, Wharton JA, Wood RJK. Micro-abrasion mechanisms of cast CoCrMo in simulated body fluids. Wear. 2009;**267**:1845-1855

[23] Wood RJK, Sun D, Thakare MR, de Frutos Rozas A, Wharton JA. Interpretation of electrochemical measurements made during micro-scale abrasion-corrosion. Tribology International. 2010;**43**:1218-1227

[24] Lima MSF, Vieira ND Jr, Morato SP, Vencovsky P. Microstructural changes due to laser ablation of oxidized surfaces on an AISI M2 tool steel. Materials Science and Engineering A. 2003;**344**:1-9

[25] Allsopp DN, Hutchings IM. Micro-scale abrasion and scratch response of PVD coatings at elevated temperatures. Wear. 2001;**251**:1308-1314

[26] Adachi K, Hutchings IM. Sensitivity of wear rates in the micro-scale abrasion test to test conditions and material hardness. Wear. 2005;**258**:318-321

[27] Cozza RC. Effect of the pressure on the abrasive wear modes transitions in micro-abrasive wear tests of WC-co P20. Tribology International. 2013;**57**:266-271

[28] Adachi K, Hutchings IM. Wear-mode mapping for the micro-scale abrasion test. Wear. 2003;**255**:23-29

[29] Huang C, Zhang Y, Vilar R, Shen J. Dry sliding wear behavior of laser clad TiVCrAlSi high entropy alloy coatings on Ti-6Al-4V substrate. Materials and Design. 2012;**41**:338-343

[30] ISO 10.993 - Biological Evaluation of Medical Devices - Part 5: Tests for Cytotoxicity: *In vitro* Methods; 1992. pp. 1-7

[31] Marques RA, Rogero SO, Terada M, Pieretti EF, Costa I. Localized corrosion resistance and cytotoxicity evaluation of Ferritic stainless steels for use in implantable dental devices with magnetic connections. International Journal of Electrochemical Science. 2014;**9**:1340-1354

[32] Pieretti EF, Pessine EJ, Correa OV, Rossi W, Neves MDM. Effect of laser parameters on the corrosion resistance of the ASTM F139 stainless steel. International Journal of Electrochemical Science. 2015;**10**:1221-1232

[33] Pieretti EF, Neves MDM. Laser marked and textured biomaterial evaluated by Mott-Schottky technique. International Journal of Electrochemical Science. 2017;**12**:9204-9211

[34] Duisabeau L, Combrade P, Forest B. Environmental effect on fretting of metallic materials for orthopaedic implants. Wear. 2004;**256**:805-816

[35] Pieretti EF, Neves MDM. Influence of laser marks on the electrochemical behaviour of the ASTM F139 stainless steel for biomedical application. International Journal of Electrochemical Science. 2016;**11**:3532-3541

Chapter 5

Surface Morphology and Tribological Properties of Nanoscale (Ti, Al, Si, C)N Multilayer Coatings Deposited by Reactive Magnetron Sputtering

Mei Wang and Shojiro Miyake

Additional information is available at the end of the chapter

http://dx.doi.org/10.5772/intechopen.73141

Abstract

The current topics related to the morphology and tribology of TiAlN monolayer, TiAlN/SiNx, TiAlN/CNx and TiAlN/CNx±CNx nanoscale multilayer coatings and refer to our recent results on the evaluation of surface morphology, and nanoscale mechanical and tribological properties of coatings deposited on cemented carbide cutting tools and silicon wafer substrates by reactive magnetron sputtering deposition. The surface morphology and microstructure of the coatings were evaluated with an atomic force microscope in dynamic friction mode together with transmission electron microscope imaging. The tribological properties of the coatings were evaluated by pin-on-disc friction testing in dry air, and high-frequency linear-oscillation friction testing under various lubrication conditions. The tribological properties of the multilayer TiAlCrSiN and TiAlSiN coatings were compared with those of a single layer TiAlN coating to evaluate their possible applications to the surfaces of cutting tools. The machining performances of single layer TiAlN, multilayer TiAlSiN, and TiAlCrSiN coated drills were investigated in drilling of carbon steel.

Keywords: surface morphology, tribological property, nanoscale multilayer, atomic force microscope, cutting tools

1. Introduction

Currently, thin hard physical vapor deposition (PVD) coatings are widely used to improve the tribological performance of forming tools, cutting tools, and machine elements [1]. In these applications, the surface morphology and tribology of the coated part are the most important factors influencing the tool and equipment performance [2]. Cutting tools might be used in

harsh machining environments without lubrication or under water-lubricated conditions. Tribological applications of thin films to cutting tools have considerably extended tool life and enabled the realization of dry machining and high-speed machining of hardened materials [3, 4]. Films of diamond-like carbon (DLC) and transition-metal and carbon nitrides (CNx), such as titanium aluminum nitride (TiAlN) and CNx are the most widely used coatings for tribological applications, such as for forming and cutting tools. Thus, it is desirable to improve the tribological properties of these films to enhance their performance in tool applications [5].

In this chapter, topics related to evaluation of the surface morphology and tribological properties of thin films are reviewed. Our recent results on the morphology and tribological properties of TiAlN monolayer, and TiAlN/SiNx and TiAlN/CNx multilayer coatings deposited on cemented carbide cutting tools and silicon wafer substrates by reactive magnetron sputtering deposition are referred in [4, 6, 7]. First, nanoscale TiAlN/SiNx multilayer films were deposited to improve the hardness of TiAlN; we found that the mechanical properties of the multilayer film were considerably improved compared with those of the monolayer film [4]. The introduction of a SiNx layer led to the formation of hard coatings owing to suppression of the TiAlN grain growth, grain refinement, and a decrease in surface roughness. A decrease in the grain diameter and associated decrease in surface roughness likely led to improved mechanical and tribological properties of the coatings [4]. However, the wear performance of the TiAlN/SiNx coating under ambient or high-temperature conditions showed negligible improvement because of its high friction coefficient. Second, CNx is an important tribological material and CNx thin films feature attractive properties such as improved hardness and elasticity and a lower friction coefficient [8, 9]. CNx thin films are currently being extensively studied for their potential tribological applications owing to their favorable mechanical and tribological properties [10]. These materials have already found applications as protective overcoatings for hard discs and read/write heads [11, 12]; furthermore, such materials are of interest in the field of nanotechnology owing to their high wear resistance and low friction properties [11, 12]. It has been found that amorphous CNx films exhibit good wear resistance with a low coefficient of friction (COF) in the range of 0.07–0.3, which is dependent on the N/C ratio and the fraction of the sp3-bonded carbon in the film [8, 9]. Therefore, attention has been paid for combining low COF CNx and hard nitrides together by forming composites or multilayer coatings to achieve the desired mechanical and tribological properties, for example, TiN:CNx composite films [13, 14], and CNx:TiN multilayer coatings [15, 16].

Several studies have indicated that multilayer coatings can exhibit high hardness and fracture resistance with low compressive stress through control of the parameters of the layered structure [5, 17]. The tribological behavior of carbon-based thin films is also strongly influenced by their chemical composition, polycrystalline structure, and surface morphology [18]. However, there remain uncertainties regarding the effects of the deposition of (Ti,Al)N, TiAlN/SiNx, TiAlN/CNx, and CNx coatings on the surface morphology, microstructure, and tribological properties of these coatings. The potential for low friction coefficients and high resistance to abrasive wear are important characteristics for high-speed and hard material cutting applications. In investigations that have aimed to increase the wear resistance and tribological properties of TiAlSiN coatings for wet cutting applications, improved tribological properties have been achieved through the incorporation of chromium (5–10 at%) into PVD TiAlSiN coatings [19–22].

The wet (water soluble fluid) machining performance of single layer TiAlN, and multilayer TiAlSiN and TiAlCrSiN coatings were assessed when drilling into a carbon steel workpiece (S50C, 50-53HRC). The objective of the present study was to assess the performance of 6-mm diameter WC–Co drills (OSG Corporation, Japan). The critical wear regions of the drills were examined metallographically with the use of a scanning electron microscope (SEM) to identify wear mechanisms acting at the cutting edges of the single layer TiAlN and multilayer TiAlCrSiN coated drills.

This chapter is focused on the influence of morphology on the tribological properties of TiAlN, TiAlN/SiNx, and TiAlN/CNx multilayer coatings with and without a CNx top layer deposited on Si(100) and cemented carbide tool steel (WC) substrates. We also compare the performance of the multilayer coatings with that of a TiAlN monolayer with and without a CNx top layer. To study the friction behavior of these films, in relation to their various structures and surface morphologies resulting from the deposition parameters, we measured the microstructure and surface morphology of the films by transmission electron microscope (TEM) and SEM imaging together with atomic force microscope (AFM) measurements. Vickers hardness, pin-on-disc friction, and high-frequency linear-oscillation (SRV) friction testing were also used to study the tribological properties and wear resistance of such coatings. Furthermore, we compared the tribological properties of the multilayer TiAlCrSiN and TiAlSiN coatings with those of a single layer TiAlN coating to evaluate their possible application to surfaces of cutting tools. The machining performance of the single layer TiAlN, multilayer TiAlSiN, and TiAlCrSiN coated drills were investigated in the drilling of carbon steel (S50C, hardness 50HRC).

2. Experimental methods

2.1. Sample preparation

Figure 1 shows a schematic illustration of the multi-target DC reactive magnetron sputtering equipment used in this experiment. The equipment consisted of four independent target holders and DC power was applied to both the target holders and the substrate holder. As shown in **Figure 2**, in this study we prepared: a TiAlN monolayer (TiAlN), a TiAlN/SiNx multilayer, and a TiAlN monolayer with a CNx top layer (TiAlN+CNx), a TiAlN/CNx multilayer with a top TiAlN layer (TiAlN/CNx+TiAlN), and a TiAlN/CNx multilayer with a CNx top layer (TiAlN/CNx+CNx) [4, 6, 7]. All coatings were prepared on polished Si wafers and cemented carbide tools by DC magnetron sputtering from TiAl alloy (50/50 at%, 99.99% purity), carbon (99.99% purity), and Si (99.99% purity) targets. Alternating deposition of TiAlN and SiNx or CNx layers was applied to realize the TiAlN/SiNx and TiAlN/CNx multilayer coatings [4, 7]. Full details of the deposition process have been previously reported [7]. The coating process consisted of three steps such as heating, cleaning by ion bombardment, and multi-nanolayer coating. The system base pressure was maintained at approximately 3.5×10^{-3} Torr to produce enough Ar ions for ion bombardment cleaning of the substrate [4]; the substrate was heated at a power of 7000 W for 30 min prior to deposition and the substrate temperature was maintained at ~420°C for the deposition. During the ion bombardment

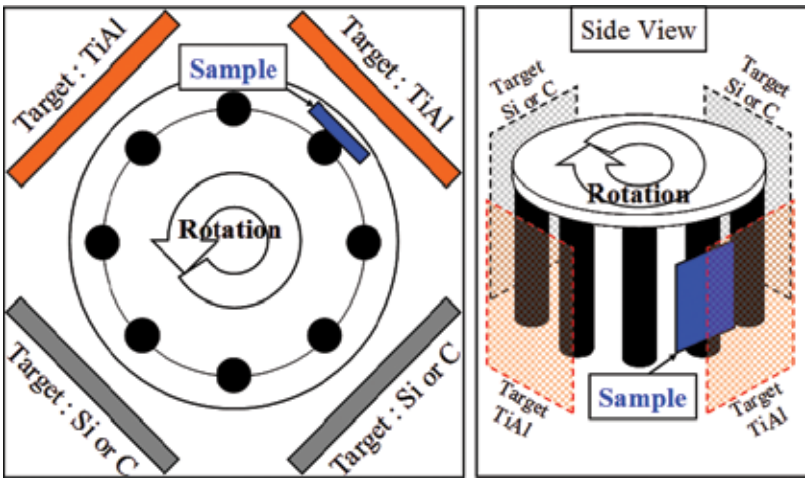

Figure 1. Schematic of DC sputtering equipment.

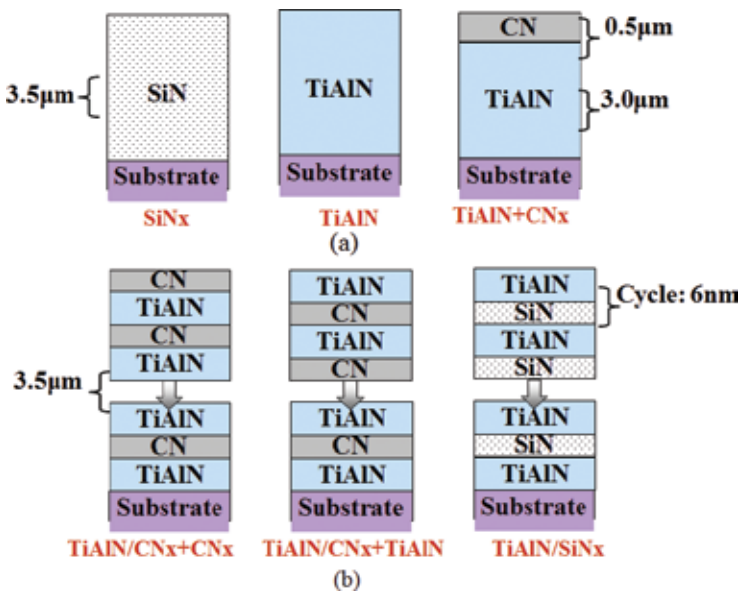

Figure 2. Samples of mono- and multilayer coatings.

cleaning process, Ar ions were directed at the substrate with a substrate bias of −500 V. Subsequently, the multi-component multi-nanolayer films were coated with a gas mixture of Ar (220 ml) and N_2 (160 ml). On the basis of preliminary experiments, the optimal deposition parameters were determined and multilayer coatings were fabricated. To compare the frictional properties of the monolayer and multilayer coatings, the total film thickness of the TiAlN, or TiAlN/CNx layers was set to be 3 μm. The CNx top layer was approximately 0.5 μm. For multilayer coatings, the layer period was set to be approximately 7 nm and the thickness of the TiAlN layer was approximately 6 nm [4, 7].

http://dx.doi.org/10.5772/intechopen.73141

2.2. Morphology and microstructure observations

The microstructures of the coatings were evaluated by TEM and SEM cross-sectional imaging. AFM was used to observe the surface of the TiAlN, SiNx, TiAlN/SiNx, TiAlN+CNx, TiAlN/CNx+TiAlN, and TiAlN/CNx+CNx coatings [4, 7]. The morphological characteristics of the coatings were measured with the use of AFM in dynamic friction mode (DFM) with a carbon nanotube tip having a radius of approximately 44 nm. The AFM system (Digital Instruments Nanoscope III, Hysitron Inc.) was used. Calculations were performed within the scanning probe image processor (SPIP) software, which is a standard program for processing AFM data at the nanoscale. The grain diameter and surface roughness of the coatings were determined by scanning an area 3 × 3 μm with the AFM. To investigate the effects of grain diameter on the surface morphology and the boundaries between the grains, simulations were performed to calculate the mean grain diameter and surface roughness of the scanning area. The coating surfaces were characterized with the use of the roughness analysis module; the values for surface roughness, average roughness (calculated by Sa: distance between peaks), and peak-peak roughness (calculated by Sy: height difference between the highest and lowest peaks in the image), were obtained by analyzing the images and cross-sectional profiles and measuring the mean grain diameter parameters.

2.3. Mechanical and tribological properties evaluation

Mechanical properties, including hardness and adhesion strength were measured by Vickers hardness and scratch testing (CSM Instruments SA). The load used for hardness measurements was 0.025 N. A scratch tester was used to apply an increasing load with a spherical diamond indenter having a radius of approximately 0.2 mm. The critical load Lc, determined by acoustic emission (AE) observations of the scratch, was used as a quantitative measurement. Full details of the methods used in the hardness and scratch tests have been previously reported [4].

The tribological properties were evaluated from pin-on-disc friction and SRV testing methods. The pin-on-disc wear test was performed at an air humidity of 50 ± 10% and a temperature of

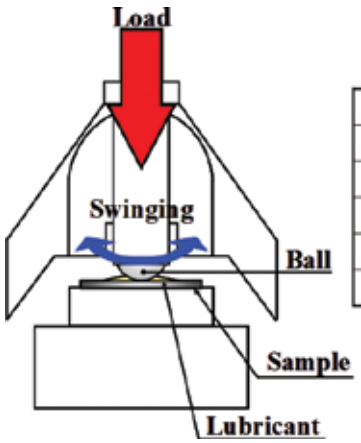

Tab.1 Friction test conditions

Load:	10N
Stroke:	500μm
Frequency:	50Hz
Number of Cycles:	30000times
Ball:	SUS440C 6.0mm
Lubricant:	Dry, Water, PAO

Water: Tap water

PAO: Poly Alpha Olefin

Figure 3. Swing type friction tester (SRV).

25 ± 3°C with the use of a pin-on-disc tribometer with a counterpart composed of SUS304 steel, placed horizontally on a turntable. The wear test was performed at a load of 0.5 N and a linear speed of 100 mm/s for a total sliding time of 600 s (corresponding to a sliding distance of 60 m). The frictional coefficients were calculated by measuring the frictional force from the wear scar area. In the SRV tests, the two test specimens, namely balls and discs, were installed in the test chamber and pressed together. As shown in **Figure 3**, the upper specimen was oscillated over the lower specimen at pre-programmed frequency, stroke, load, and temperature settings. In this study, the test was conducted with the use of an AISI440C ball indenter (SUS440C, 6.0 mm diameter) without lubricant under a 10 N load, with the use of a 500-μm stroke, a 50-Hz frequency, and 30,000 revolutions at room temperature and atmospheric pressure (30–45% humidity). The wear profiles of the coatings were measured by the SRV test.

3. Result and discussion

3.1. Microstructure and morphology

SEM micrographs of the film fracture cross-sections are shown in **Figure 4** for the TiAlN monolayer with a thickness of approximately 3 μm and the TiAlN/SiNx and TiAlN/CNx multilayer coatings with a total thickness of approximately 3.6 μm [7]. TiAlN has a columnar morphology, as shown in **Figure 4a**. The introduction of SiNx into the coating system changed the fracture morphology of TiAlN from a columnar microstructure to a fine-grained structure

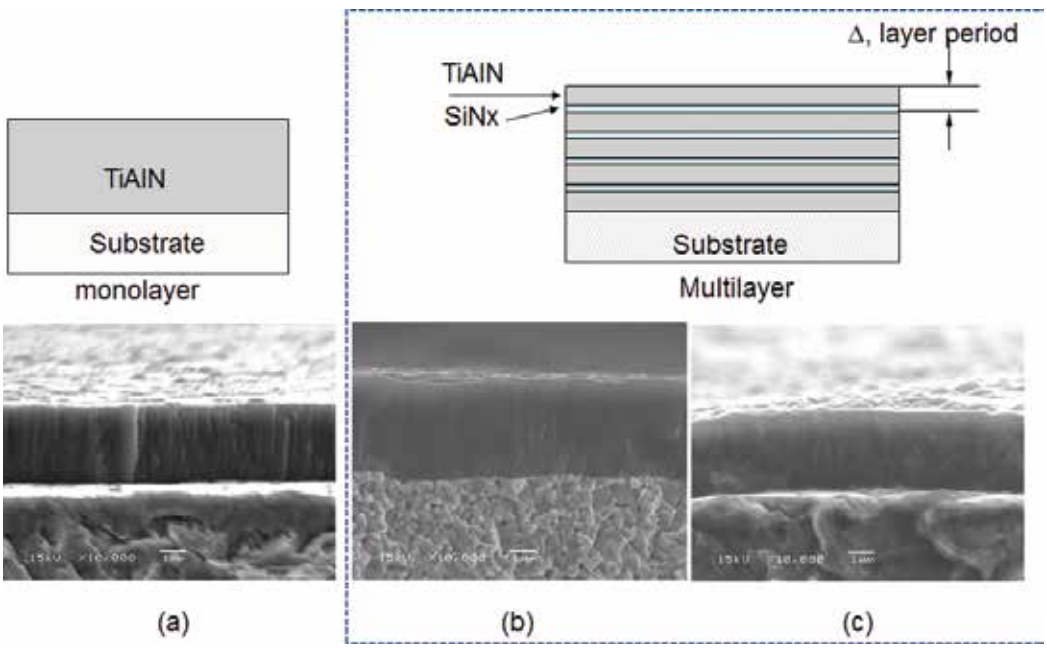

Figure 4. Cross-sectional image of TiAlN monolayer, and TiAlN/SiNx and TiAlN/CNx multilayer coatings.

of TiAlN/SiNx, as shown in **Figure 4b**. This effect could be attributed to growth of the primary nuclei on the top layer (**Figure 4b**). This result indicates that growth of crystals was blocked periodically by the development of the surface covering layer, which covered the whole surface of the crystals and suppressed grain growth [4, 7, 23]. **Figure 4c** shows a SEM image of a fracture cross-section of a TiAlN/CNx coating. The TiAlN/CNx also showed a fine-grained structure owing to the introduction of CNx into the coating system [7].

Figure 5 shows TEM images of the microstructure of a TiAlN/SiNx multilayer film. The TiAlN/SiNx was formed by alternation of the TiAlN and SiNx layers at a rotation speed of 3 revolution per minute (rpm) [4]. A nanolayered structure composed of sequentially alternating TiAlN and SiNx layers was confirmed [4]. High resolution TEM images of the TiAlN/SiNx nanolayer cross-section exhibited a bilayer period of 6–8 nm and nanometer-sized grains. The white arrows in the figure indicate the film growth direction. The film morphology showed a dense columnar structure.

Figure 6 shows a TEM image of the microstructure of a TiAlN/CNx+CNx multilayer film. As shown in area I (**Figure 6a**, marked by an arrow), the bright dots indicate the presence of a CNx top layer phase with a uniform amorphous structure. In areas II and III of **Figure 6a** (indicated by arrows), micro-diffraction patterns featured both individual spots and continuous rings that corresponded to the superposition of individual diffraction patterns of TiAlN and CNx [7]. **Figure 6b** shows that the film morphology was fine-grained and that the growth directions of the TiAlN and CNx layers alternated, as indicated by the dark and bright layers, respectively. **Figure 6c** shows that the TiAlN nanolayers in the TiAlN/CNx coating were approximately 5-nm thick and separated by a matrix of amorphous carbon [4]. This result suggests that the TiAlN/CNx multilayer had a modulated structure with a periodicity of approximately 7 nm, indicating that the nanolayered structure was composed of sequentially alternating TiAlN/CNx, owing to the rotation speed of 3 rpm [4, 7, 23, 24].

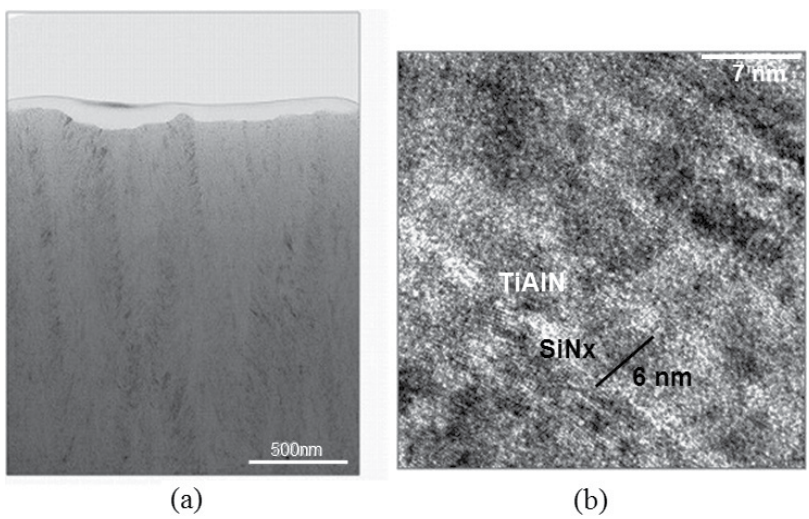

Figure 5. Cross-sectional TEM images of TiAlN/SiN coating, observed at scale of (a) 500 nm and (b) 7 nm.

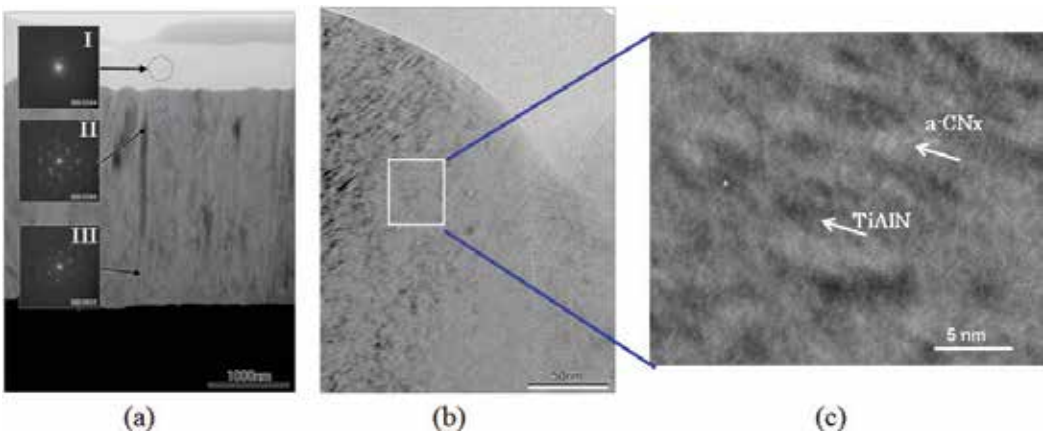

Figure 6. Cross-sectional TEM images of the TiAlN/CNx + CNx coating observed at scales of (a) 1000 nm, (b) 50 nm, and (c) 5 nm.

The surface morphology and roughness of the films were observed by AFM in DFM and analyzed by collecting three-dimensional surface profile data. The mean grain diameters of the samples were determined by averaging three or more results obtained from a 3 × 3 μm area. As shown in **Figure 7**, the average grain diameters for the TiAlN (**Figure 7a**) and TiAlN/SiNx (**Figure 7b**) films were 342 and 274 nm, respectively. In **Figure 7**, we compared the TiAlN and TiAlN/SiNx films, to show that the average grain diameter of TiAlN/SiNx was smaller than that of TiAlN. Hence, the introduction of the SiNx layer contributed to a decrease in the grain diameter [4]. The roughness of the TiAlN and TiAlN/SiNx films was determined by measuring the grain diameter and surface peak-peak height (Sy) with the AFM, where Sy is defined as the height difference between the highest and lowest peaks in the topology [4]. The

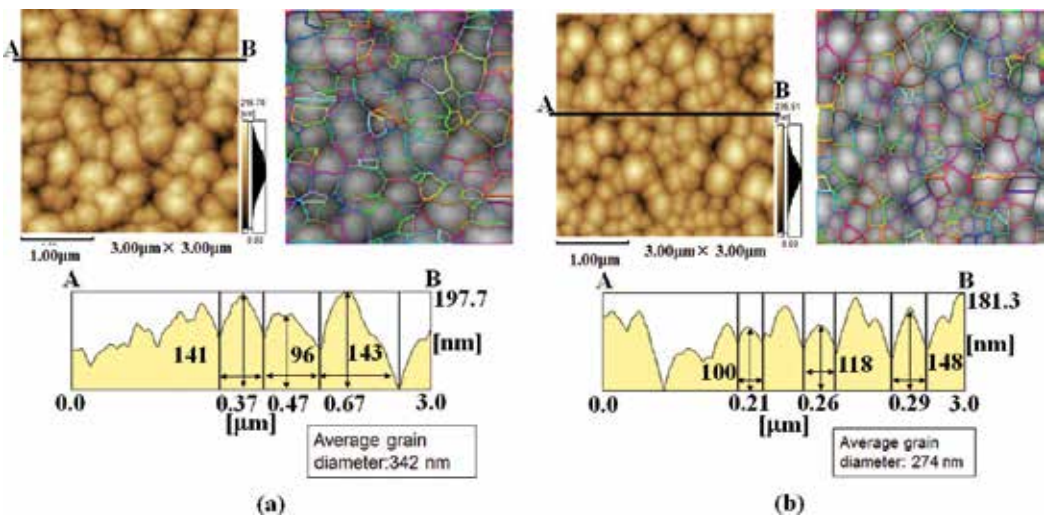

Figure 7. Surface topography map and cross-sectional image profiles of the TiAlN (a) and TiAlN/SiNx (b) films.

http://dx.doi.org/10.5772/intechopen.73141

DFM measurement showed that the TiAlN coating had a Sy value of 211 nm. The Sy value for the TiAlN/SiNx was approximately 180 nm. Thus, the Sy of the TiAlN/SiNx coating decreased together with the grain diameter.

As shown in **Figure 8**, the average grain diameters for TiAlN + CNx (**Figure 8a**), TIAlN/CNx + TiAlN (**Figure 8b**), and TiAlN/CNx + CNx (**Figure 8c**) films were 168, 175, and 161 nm, respectively [7]. The Sy values for the TiAlN + CNx, TIAlN/CNx + TiAlN, and TiAlN/CNx + CNx films were 31.8, 46.9, and 28.2 nm, respectively. The mean grain diameters and Sy value (roughness) of the multilayer TiAlN/CNx + TiAlN and TiAlN/CNx + CNx films were smaller than that of the TiAlN film owing to the introduction of the CNx layer [7]. As a result, the average grain diameters of the TiAlN and TiAlN/CNx film decreased owing to the deposition of the CNx top layer. The TiAlN and TiAlN/CNx films consisted of an arrangement of globular grains with fine spaces and intervals, which became filled by CNx during the

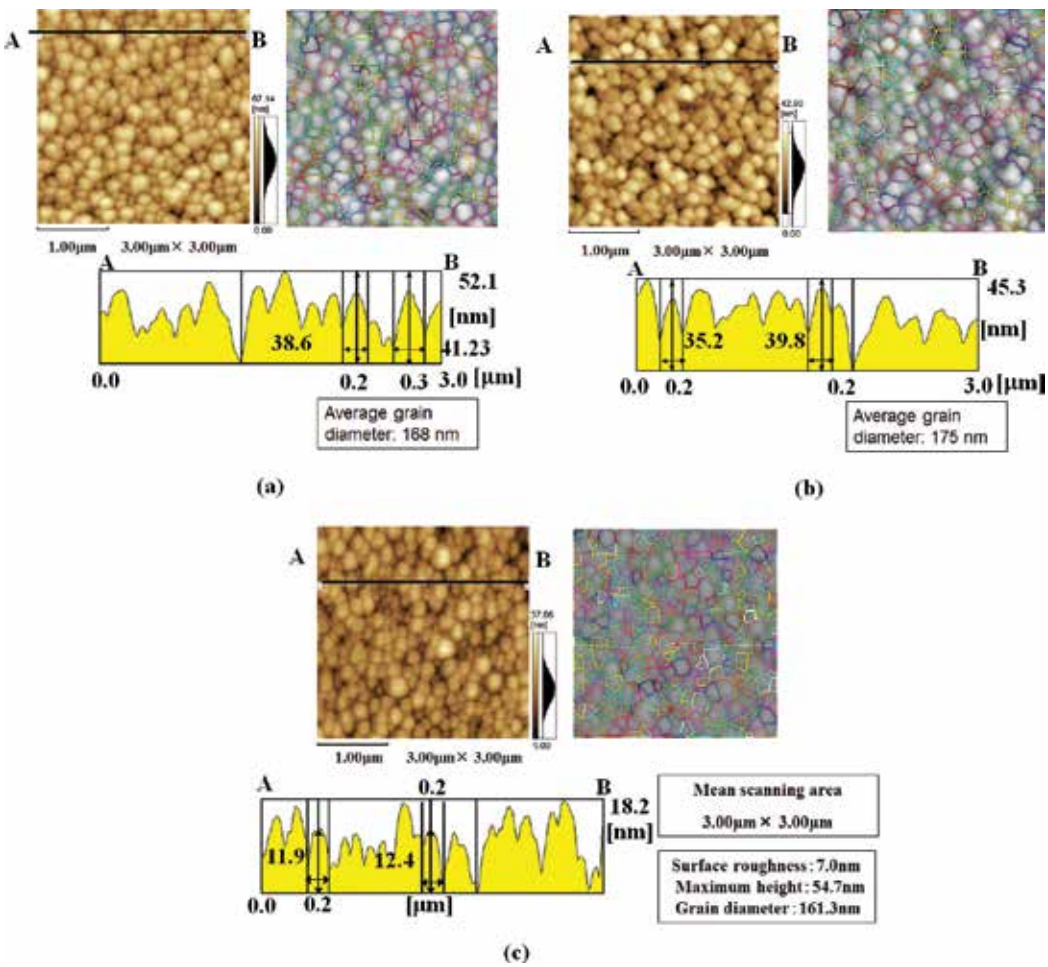

Figure 8. Surface topography map and cross-sectional image profiles of the TiAlN + CNx (a), TiAlN/CNx + TiAlN top (b) and TiAlN/CNx + CNx top films (c).

deposition of CNx as the top layer. Bonds formed between the CNx and TiAlN (or TiAlN/CNx) led to an increase in the area of boundaries [4, 7]. The morphology was related to the thickness and morphology of the top coating. The CNx top layer had a considerable effect on the surface morphology and roughness, changing the real contact area and the friction and wear behavior. Generally, the surface roughness decreased as the grain size decreased. This trend was accompanied by an improvement in the density of the morphology with a marked transition from a columnar to a fine-grained morphology [25].

The introduction of SiNx or CNx onto the TiAlN monolayer and the apparent decrease in the grain size could have contributed to the small increase of the hardness for the multilayer TiAlN/SiNx and TiAlN/CNx. The first factor that we considered was the structure parameter. When SiNx or CNx was introduced onto the TiAlN, there was a decrease in the grain size, an increase in the compressive stress level, and an improvement in the coating density accompanying the transition from a columnar to fine-grained morphology. All these factors are known to contribute to hardening of materials [25].

Factors such as residual stress, morphology, phase composition, and grain size are usually taken into account as hardening mechanisms and were considered here; however, we did not identify any major changes between the ternary and binary films that could explain the observed trend in hardness. We believed that the decrease in grain diameter might have resulted in a decrease in surface roughness, which led to the improved mechanical and tribological properties of the films [4, 7].

3.2. Evaluation of mechanical properties

The results from the characterization of the TiAlN, TiAlN/SiNx, TiAlN + CNx, TiAlN/CNx + TiAlN, and TiAlN/CNx + CNx films are summarized in **Table 1** [4, 7]. The hardness measured for TiAlN was 2590 HV. The hardness values of the multilayer TiAlN/SiNx, TiAlN/CNx + TiAlN, and TiAlN/CNx + CNx films were higher than those of the monolayer TiAlN and TiAlN + CNx films. The increase in hardness could be attributed to the introduction of a large number of TiAlN/SiNx and TiAlN/CNx interfaces in the cases of the TiAlN/SiNx and TiAlN/CNx films, respectively [4, 7]. The high hardness of the multilayer coatings is related to the role of interfaces as effective obstacles to lattice dislocation slip, which is the dominant deformation mechanism in microscale composite coatings. Owing to these interfacial and nanoscale effects, conventional lattice dislocation slip was prevented in the nanostructure

Coating	Hardness (HV0.025)	Critical Load (N)	Average grain diameter (nm)	Surface peak-peak height (Sy)
TiAlN	2590	64	342	211
TiAlN/SiNx	3200	88	274	180
TiAlN+CNx	2552	86	168	31.8
TiAlN/CNx+TiAlN	2989	127	175	46.9
TiAlN/CNx+CNx	2886	120	161	28.2

Table 1. Vickers microhardness, critical load, grain size and roughness (Sy) of monolayer and multilayer films.

coatings [4, 26, 27]. Scratch tests were conducted on the coatings and the results are shown in **Table 1**. The multilayer TiAlN/SiNx, TiAlN/CNx + TiAlN, and TiAlN/CNx + CNx films showed higher critical load values than the monolayer TiAlN and TiAlN + CNx films. These results suggest that the improved adhesion strength might be attributed to the interfaces of the multilayer preventing extension of fractures and the multilayer structure improving the wear resistance of the coating [4].

3.3. Evaluation of tribological properties

All the mono- and multilayer systems were investigated by a reciprocating SRV friction test under dry conditions, and with water and polyalphaolefin (PAO) as a lubricating film to characterize the coating frictional properties. PAO (WO-20) made by Nissan is a lubricating oil for engines and commercially available. Since PAO has characteristics such as low pour point, high viscosity index, evaporation characteristics, low traction, etc., it was used as a lubricant film in this study. The Si wafer substrates (test discs) were coated with the monolayer and multilayer systems and tested with an AISI440C ball indenter, (SUS440C, diameter: 6.0 mm). This test provided information about the cycle number dependence of the friction coefficient, and the wear behavior of the coated substrate and of its tribological counterpart. The wear volume was deduced from the wear depth created at the counterpart and was used to quantify the counterpart wear. Optical microscopy and energy dispersive X-ray spectroscopy were used to examine the wear of the coated substrate.

3.3.1. Frictional and wear properties under dry conditions

Figure 9 shows the variation of the coefficient of friction as a function of the number of sliding cycles for the investigated mono- and multilayer systems under dry conditions at room temperature. The coefficient of friction was taken as the average of four tests. Although the SiNx, TiAlNx, and TiAlN/SiNx coatings showed similar friction coefficients (1.11, 0.93, and 0.99, respectively) in frictional contact with a steel counterpart (**Figure 9a-c**), the abrasive wear of the SiNx and TiAlN coating was greater than that of the TiAlN/SiNx coating. Investigations of the wear after testing were performed with an optical microscope. Corresponding optical photomicrographs and cross-sectional images of the wear marks formed on the coatings are shown in **Figure 10**, comparing the monolayer SiNx, TiAlN, and multilayer TiAlN/SiNx films. The average cross-sectional areas of the wear tracks were measured at three or more locations after 30,000 revolutions. For the dry conditions, the wear depth of SiNx was over 29.5 μm (**Figure 10a**) and that of the TiAlN was approximately 13.6 μm (**Figure 10b**). The TiAlN/SiNx film had a wear depth of 9.9 μm (**Figure 10c**) and showed better wear resistance than that of the SiNx and TiAlN films. Although the TiAlN film showed lower friction coefficients than that of the TiAlN/SiNx film (**Figure 9a–c**), the abrasive wear of the TiAlN film was greater than that of the TiAlN/SiNx film. The wear resistance of the TiAlN/SiNx film was enhanced owing to its nanolayer microstructure and small grain size compared with that of the TiAlN film. We believe that the decrease of the grain diameter might have caused a decrease of the surface roughness, which led to the improved tribological properties of the coating. Conversely, as shown in **Figure 9c-f**, the monolayer TiAlN + CNx film showed a lower friction coefficient

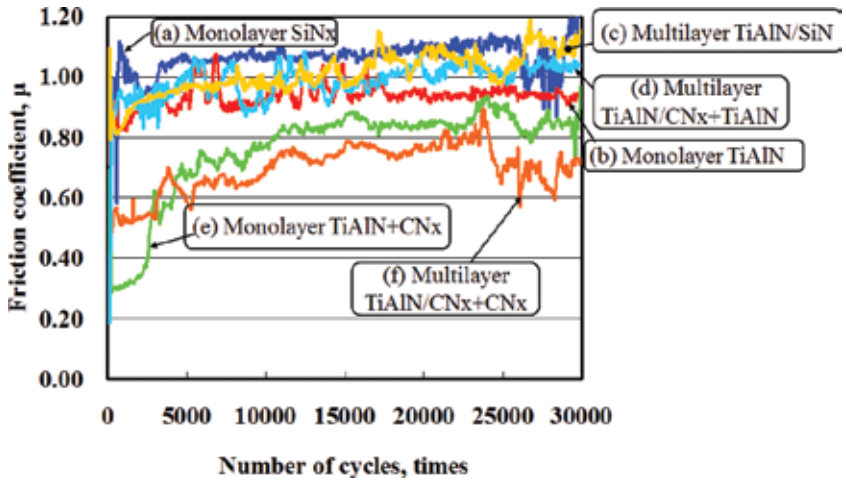

Figure 9. Friction coefficient vs. number of sliding cycles for the SRV friction test under dry conditions for: (a) SiNx, (b) TiAlN, (c) TiAlN/SiN, (d) TiAlN/CNx + TiAlN, (e) TiAlN + CNx, and (f) TiAlN/CNx + CNx coatings.

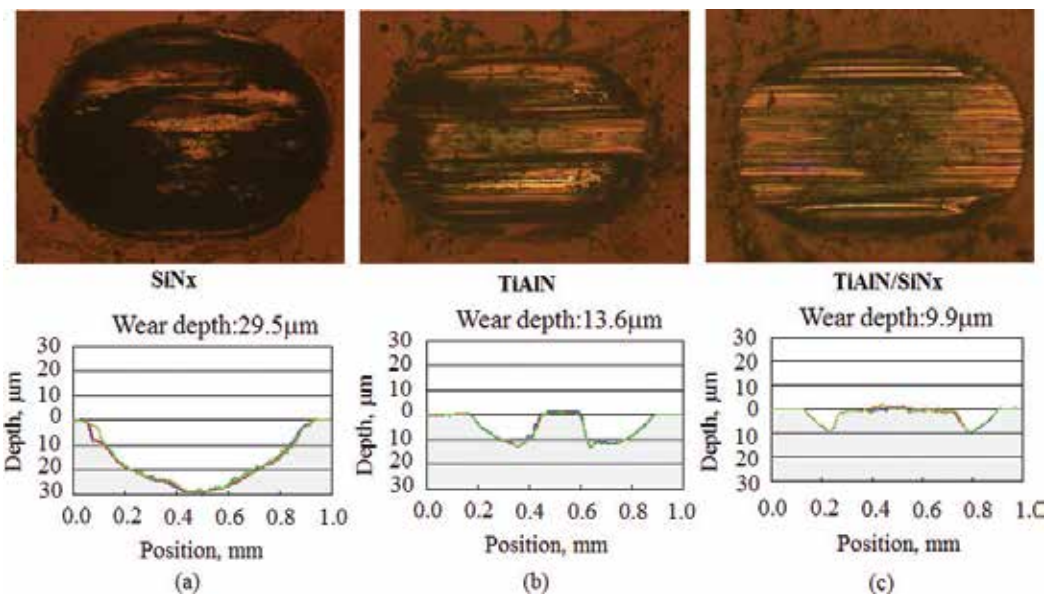

Figure 10. Wear profiles of the SiNx (a), TiAlN (b) and TiAlN/SiNx (c) coatings after SRV testing under dry conditions.

(approximately 0.71, as shown in **Figure 9e**) followed by 0.93 for the monolayer TiAlN (**Figure 9b**), 0.99 for the TiAlN/SiNx (**Figure 9c**), and 1.03 for TiAlN/CNx + TiAlN (**Figure 9d**) films. Thus, the TiAlN film with the CNx top layer had the second lowest friction coefficient of approximately 0.71. Notably, the TiAlN/CNx films with the CNx top layer had considerably lower friction coefficients than the other coatings. Furthermore, the lowest friction coefficient (approximately 0.62), which also showed a tendency to further decrease, was observed for the

multilayer TiAlN/CNx + CNx film, as shown in **Figure 9f**. Corresponding optical photomicrographs and cross-sectional images of the wear marks formed on the films are shown in **Figures 11** and **12**. The size of wear scar was calculated from the cross-sectional area of the central portion of the wear mark. The average cross-sectional areas of the wear tracks were obtained at three or more locations after 30,000 revolutions, and the size of wear scar of the

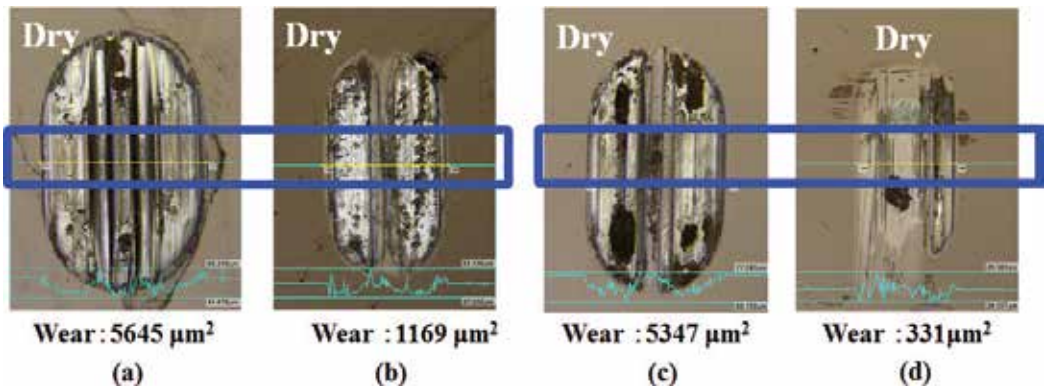

Figure 11. Wear profiles of (a) TiAlN, (b) TiAlN + CNx, (c) TiAlN/CNx + TiAlN, and (d) TiAlN/CNx + CNx coatings after SRV testing under dry conditions.

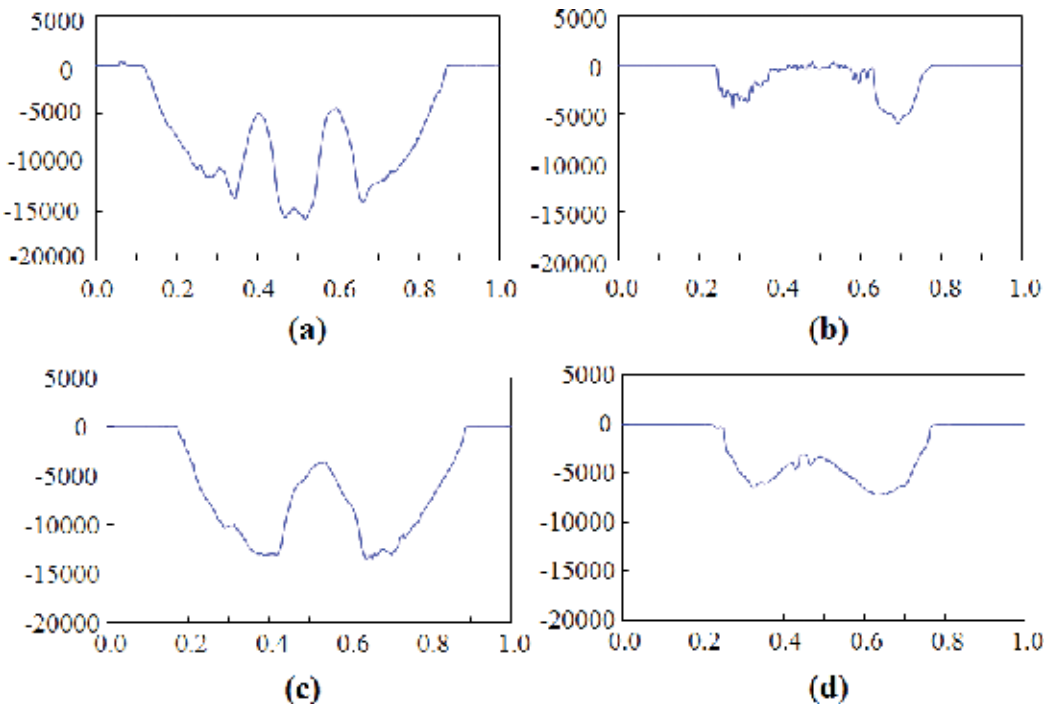

Figure 12. Cross-sectional images of wear created by SRV testing under dry conditions on (a) TiAlN, (b) TiAlN + CNx, (c) TiAlN/CNx + TiAlN, and (d) TiAlN/CNx + CNx coatings.

films were recorded after testing. The size of wear scar of the TiAlN films was greater than 5645 μm^2 (**Figures 11a** and **12a**), while that of the TiAlN/CNx + TiAlN film size was approximately 5347 μm^2 (**Figures 11c** and **12c**). However, the sizes of wear scar of the TiAlN + CNx and the TiAlN/CNx + CNx films were 1169 and 331 μm^2, as shown in **Figures 11b** and **d** and **12b** and **d**, respectively. The TiAlN/CNx + TiAlN film showed better wear resistance than the TiAlN film. The improvement in wear resistance can be attributed to the introduction of a large number of TiAlN/CNx interfaces and refinement of the multilayer microstructure. The friction coefficient and size of wear scar of the TiAlN + CNx and TiAlN/CNx + CNx films were small, such that the wear resistance values were clearly improved by the deposition of the CNx top layer because the CNx film has both wear resistance and lubricating properties [8–10].

3.3.2. Frictional and wear properties under water lubrication

The friction coefficients of the coatings were measured in the sliding system with the use of water as a lubricant. As shown in **Figure 13**, the friction coefficients of the SiNx, TiAlN, TiAlN/SiNx, TiAlN/CNx + TiAlN, TiAlN + CNx, and TiAlN/CNx + CNx films were 0.54, 0.46, 0.52, 0.45, 0.23, and 0.22 (**Figure 13a-f**, respectively). For the monolayer SiNx and TiAlN, and multilayer TiAlN/SiNx, as shown in **Figure 14**, although a large wear track (approximately 28.1 μm deep) was observed for the monolayer SiNx (**Figure 14a**), no apparent wear tracks were observed for the TiAlN (**Figure 14b**) and TiAlN/SiNx (**Figure 14c**) films under water lubrication. This result indicates that the wear resistance of the TiAlN and TiAlN/SiNx films was improved by water lubrication [4, 7].

For the TiAlN, TiAlN/CNx + TiAlN, TiAlN + CNx, and TiAlN/CNx + CNx samples, optical photographs and cross-sectional images of the wear tracks formed on the coatings are shown in **Figures 15** and **16**. The wear of the films was evaluated from the size of wear scar, as described earlier. We observed that the mean sizes of wear scar were 301, 296, 203, and 184 μm^2 for the TiAlN, TiAlN/CNx + TiAlN, TiAlN + CNx, and TiAlN/CNx + CNx films, respectively. Although

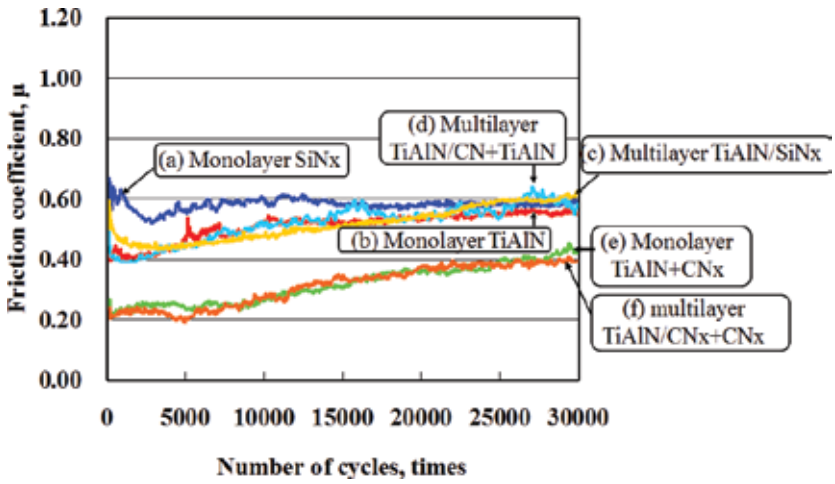

Figure 13. Friction coefficients of the coatings determined by SRV testing under water lubrication.

http://dx.doi.org/10.5772/intechopen.73141

the TiAlN and TiAlN/CNx + TiAlN films showed similar friction coefficients, the size of wear scar of the TiAlN film is larger than that of TiAlN/CNx + TiAlN, indicating that the wear resistance of the TiAlN/CNx + TiAlN film was improved by the multilayered structure. However, the wear resistance and friction coefficients of the TiAlN + CNx and TiAlN/CNx + CNx films were considerably improved owing to the deposition of CNx [7], which has both wear resistance and lubricating properties [8–10]. This result is consistent with the reduced surface roughness and grain diameters of the films. Notably, the lowest friction and wear depths under the water lubrication conditions were obtained for the coatings with the CNx top layer, indicating that the wear resistance of the CNx layer is higher in humid air. Specifically, the lowest friction coefficients were 0.23 and 0.22 for the TiAlN + CNx and TiAlN/CNx + CNx coatings,

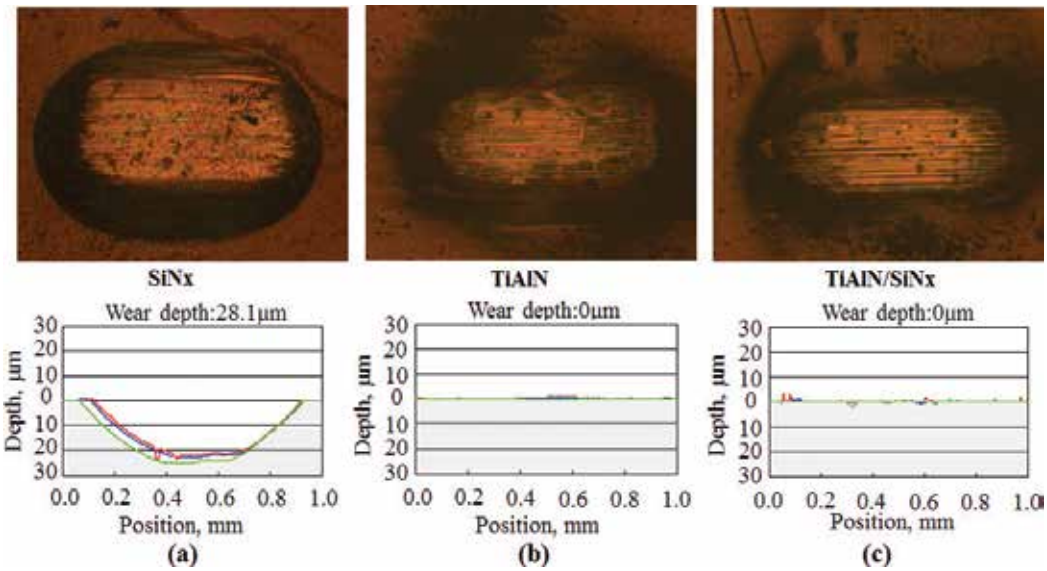

Figure 14. Wear profiles of the SiNx, TiAlN, and TiAlN/SiNx coatings after SRV testing under water lubrication.

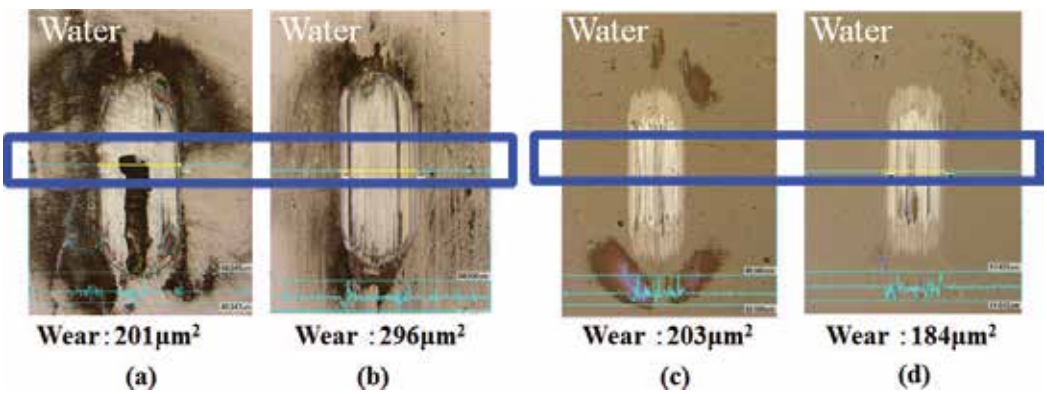

Figure 15. Wear profiles of (a) TiAlN, (b) TiAlN/CNx + TiAlN, (c) TiAlN + CNx, and (d) TiAlN/CNx + CNx coatings after SRV testing under water lubrication.

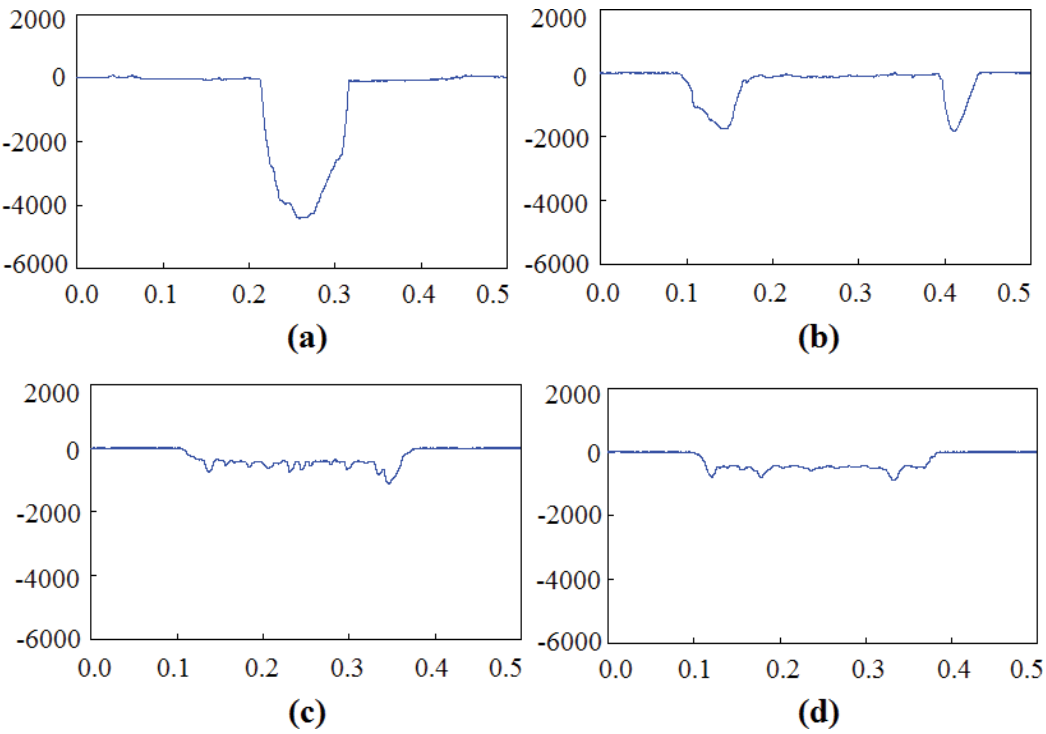

Figure 16. Cross-sectional images of wear created by SRV testing under water lubrication on the (a) TiAlN, (b) TiAlN/CNx + TiAlN, (c) TiAlN + CNx, and (d) TiAlN/CNx + CNx coatings.

values which were, respectively, 49 and 51% of the friction coefficient for the coatings without the CNx layer [7].

3.3.3. Frictional and wear properties under PAO lubrication

Figure 17 shows the variation of the coefficient of friction measured from SRV testing under PAO lubrication. The mean values of the friction coefficients for SiNx, TiAlN, TiAlN/SiNx, TiAlN/CNx + TiAlN, TiAlN + CNx, and TiAlN/CNx + CNx coatings were 0.18, 0.16, 0.19, 0.15, 0.15, and 0.14 (**Figure 17a-f**, respectively). Although the differences among the friction coefficients of the coatings was small, the TiAlN and TiAlN/CNx + TiAlN films with the CNx top layer had lower friction coefficients than those without the CNx top layer. The wear tracks formed on the coatings were observed by laser microscopy. Optical photographs and cross-sectional images of the wear tracks are shown in **Figure 18**. The size of wear scar was markedly reduced for all coatings measured by SRV testing under PAO lubrication compared with those under dry and water conditions. The sizes of wear scar were 73.0, 24.0, 14.7, and 14.3 μm^2 for the TiAlN, TiAlN + CNx, TiAlN/CNx + TiAlN, and TiAlN/CNx + CNx films. The PAO lubricant reduced the size of wear scar for the coatings with and without the CNx top layer. For the multilayer TiAlN/CNx + TiAlN, the size of wear scar of the TiAlN/CNx + TiAlN film was lower and similar to that of the TiAlN/CNx + CNx film when PAO was introduced as a

http://dx.doi.org/10.5772/intechopen.73141

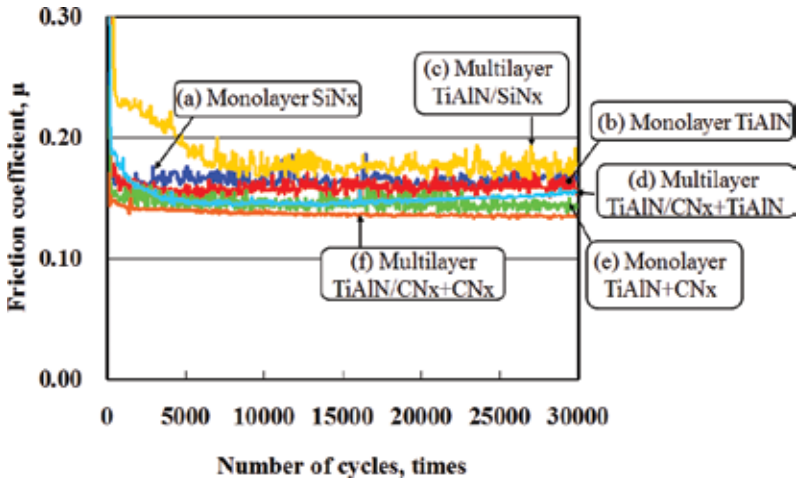

Figure 17. Average friction coefficients for monolayer and multilayer films under dry conditions and water and PAO lubrication.

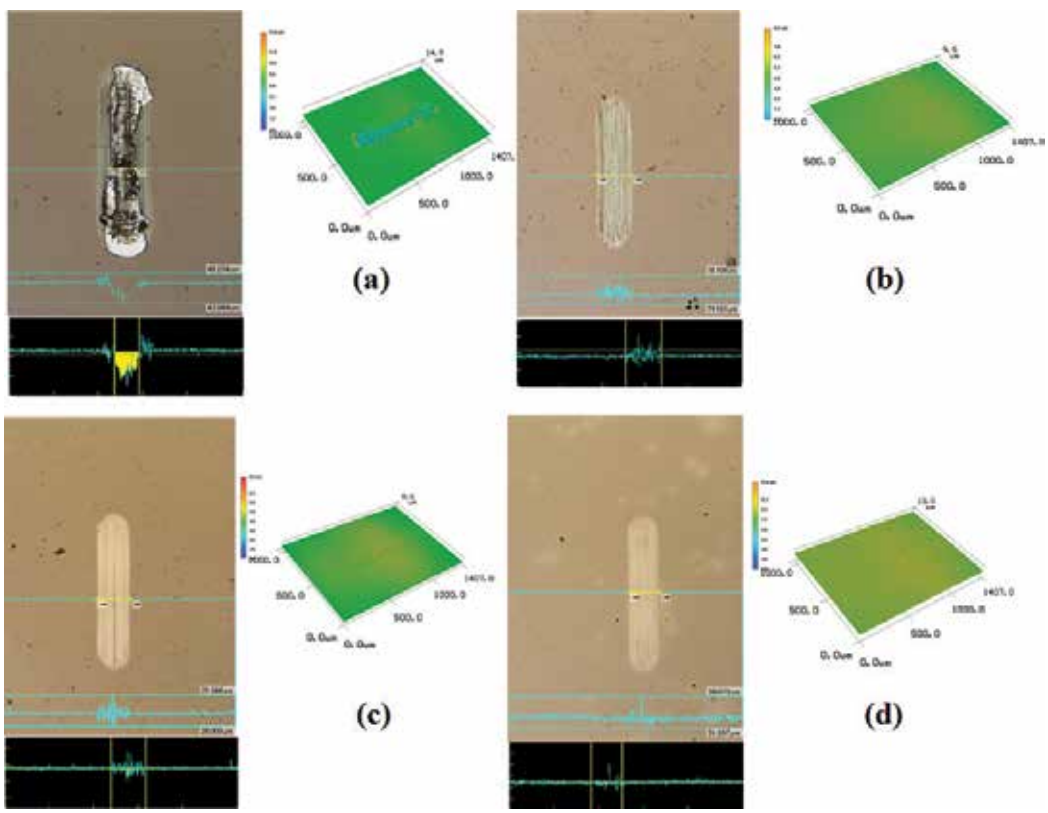

Figure 18. Images and cross-sectional of wear created by SRV testing under PAO lubrication on (a) TiAlN, (b) TiAlN/CNx + TiAlN, (c) TiAlN + CNx, and (d) TiAlN/CNx + CNx coatings.

lubricant. This result suggests that under these lubricant conditions a beneficial tribolayer forms on the wear surface, which provides a low coefficient of friction.

The friction coefficients of the films, as determined by SRV friction testing, are summarized in **Figure 19** for dry, water, and PAO conditions. The coatings with the CNx top layer showed a lower friction coefficient under dry and water conditions than the coatings without the CNx top layer. However, all the coatings showed low friction coefficients owing to the introduction of water or PAO lubricants. This result suggests that lubricants such as water and PAO can improve the tribological properties in terms of friction and wear control in, for example, cutting applications.

3.4. Performance of single layer and multilayer coatings in drilling

Single layer TiAlN, and nanoscale multilayer TiAlSiN and TiAlCrSiN coatings were prepared on cemented carbide pins and WC–Co drills by reactive magnetron sputtering deposition. The deposition conditions are detailed in previous reports [4, 7]. The tribological characteristics of the films were investigated with the use of a pin-on-disc friction test. The pin-on-disc wear test was performed at an air humidity of 50 ± 10% and a temperature of 25 ± 3°C with a pin-on-disc tribometer featuring a counterpart composed of cemented carbide [4]. The wear test was performed at a load of 2 N and a linear speed of 150 mm/s for a total sliding time of 900 s (corresponding to a sliding distance of 135 m). **Figure 20** compares the friction coefficients of the TiAlN, TiAlSiN, and TiAlCrSiN films. The TiAlCrSiN (**Figure 20c**) showed a stable and low friction coefficient in the range of 0.35–0.42; the values for TiAlN and TiAlSiN were 0.53 and 0.54, respectively (**Figure 20a** and **b**). The stable frictional properties of the TiAlCrSiN film were attributed to the nanolayer microstructure. The wear tracks formed on the films were

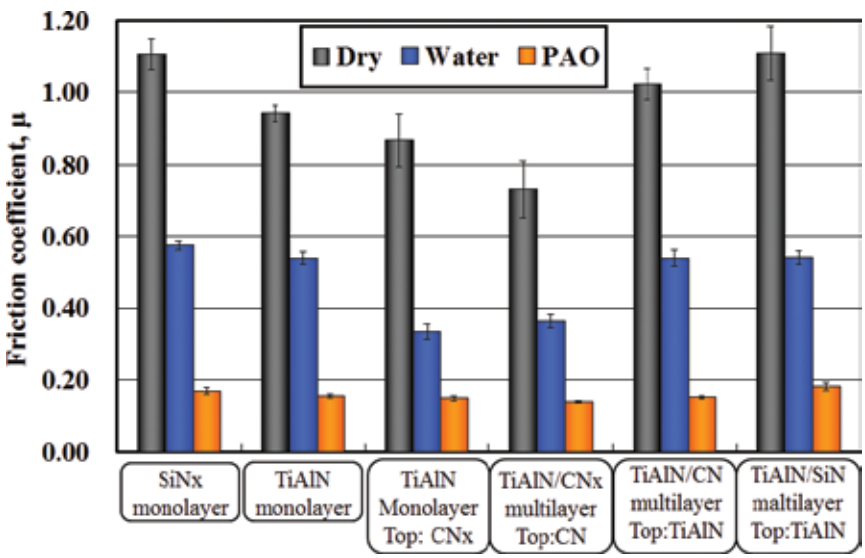

Figure 19. Average friction coefficients for monolayer and multilayer films under dry conditions and water and PAO lubrication.

http://dx.doi.org/10.5772/intechopen.73141

observed by laser microscopy. **Figure 21** shows the profile and cross-section images of the wear tracks. The sizes of wear scar of the TiAlN (**Figure 21a**) and TiAlSiN (**Figure 21b**) coatings were 1.6 × 10^5 and 7.9 × 10^4 μm^2. The multilayer TiAlCrSiN coating (**Figure 21c**) showed a lower size of wear scar (approximately 3.6 × 10^4 μm^2) compared with that of the single layer TiAlN and multilayer layer TiAlSiN coatings. The wear resistance of the multilayer TiAlCrSiN coating was further improved by incorporation Cr into the TiAlSiN coating.

Friction properties and wear resistance to abrasive wear and oxidation are important characteristics for high-speed and cutting application. The lifetimes of the monolayer TiAlN, and multilayer TiAlSiN and TiAlCrSiN coated 6-mm diameter WC–Co drills (OSG Corporation, Japan) in wet (water soluble fluid) drilling of carbon steel (S50C, 50-53HRC) are shown in

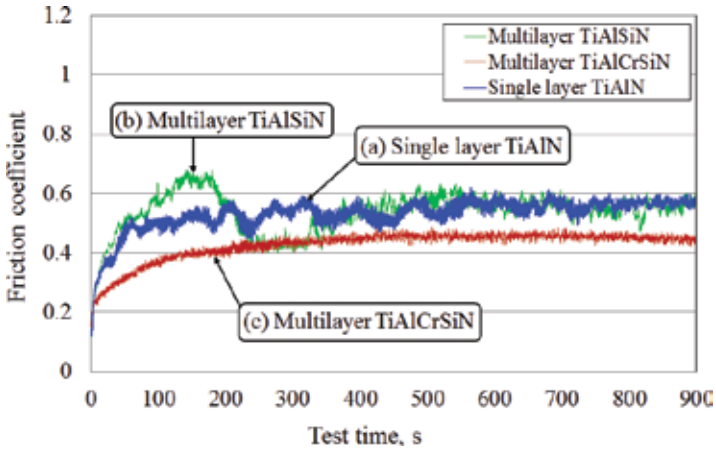

Figure 20. Friction coefficients of the coatings by pin-on-disc testing under dry conditions.

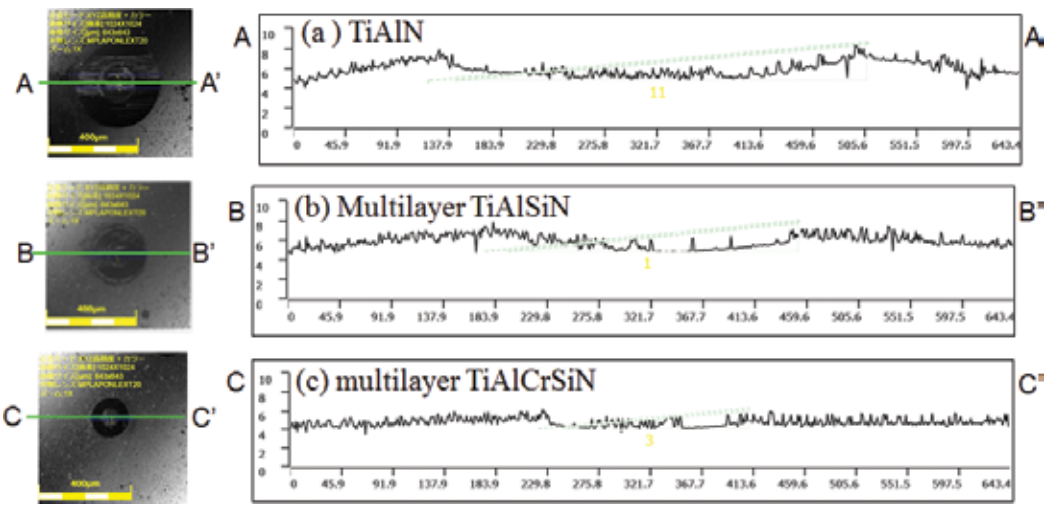

Figure 21. Wear tracks and cross-sectional images of the coatings subjected to pin-on-disc test under dry conditions.

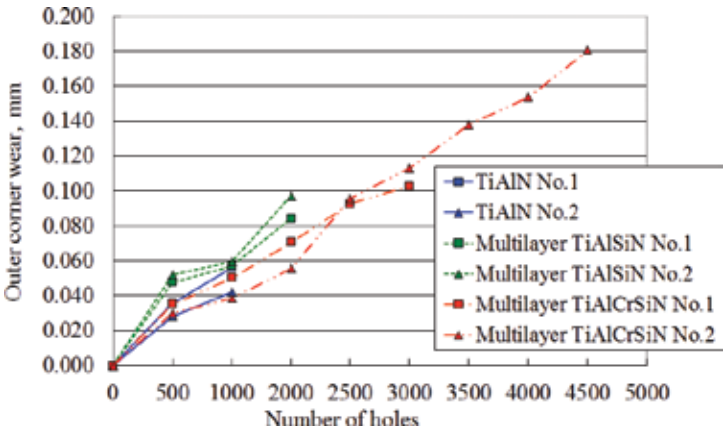

Figure 22. Outer corner wear of 6-mm diameter WC–co drills as a function of the number of holes drilled. Cutting speed: 100 m/min (5304 rpm), feed rate: 0.18 mm/rev. Workpiece: Carbon steel (S50C). Cutting fluid: Water soluble agent. Hole depth 30 mm (5×diameter).

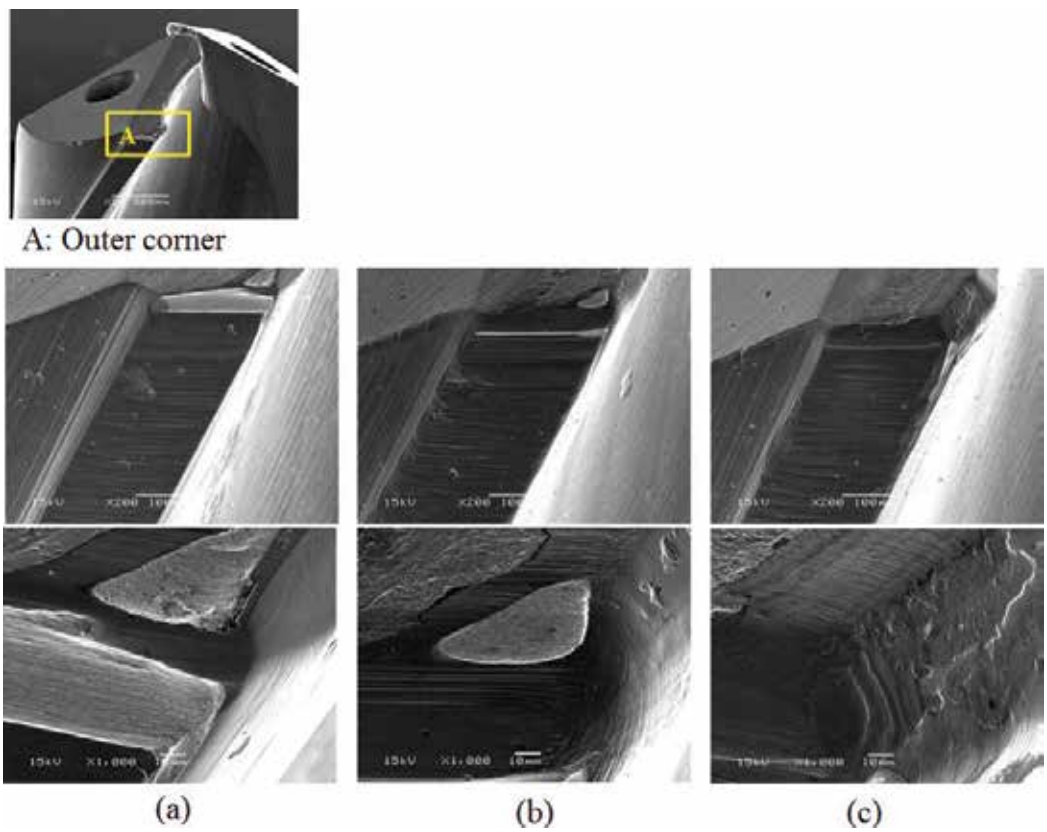

Figure 23. SEM images of the outer corner of worn areas of (a) TiAlN, (b) multilayer TiAlSiN, and (c) multilayer TiAlCrSiN coated 6 mm diameter WC–co drills after 1000-hole drilling test.

Figure 22. The performances of the multilayer TiAlSiN and TiAlCrSiN coatings were compared with that of the single layer TiAlN coating, which was used as reference. The drilling tests were performed on a drill-milling machine NH4000 (DMG MORI, Japan) at a cutting speed of 100 m/min (5304 rpm), feed rate of 0.18 mm/rev (955 mm/min), hole depth of 30 mm (5×diameter), and allowance of 0.2 mm. The lifetime of drills with the multilayer TiAlCrSiN coating was 2.01 times as long as that of the tools coated with single layer TiAlN and the multilayer TiAlSiN coatings. To investigate the differences observed in the performance of the coatings, the morphology of the outer corner flank was examined by SEM imaging. The wear patterns observed are shown in **Figure 23**. After drilling 1000 holes, the single layer TiAlN and multilayer TiAlSiN coatings showed considerable wear at the outer corner and margin of the drill bit (**Figure 23a** and **b**). Conversely, the multilayer TiAlCrSiN coated drill showed negligible wear at the outer corner and margin (**Figure 23c**). The superior drilling performance of the multilayer TiAlCrSiN coating compared with those of the single layer TiAlN and TiAlSiN coatings can be attributed to more favorable mechanical (high hardness) and tribological (low friction) properties, and wear resistance. The performance was likely enhanced by the incorporation of Cr into the multilayer TiAlSiN coating [19–22]. The low friction coefficient suggests that the decreased friction between the tool and chip in machining and a reduced tendency to stick and pick up material from the counterpart material, led to the extended service life of the cutting tool.

4. Conclusion

TiAlN monolayer, TiAlN/SiNx, TiAlN/CNx, TiAlSiN, and TiAlCrSiN multilayer coatings were deposited on WC–Co carbide tools and silicon wafer substrates by reactive magnetron sputtering. We show that the multilayer structure affects the surface morphology, microstructure, mechanical, and tribological properties.

1. The introduction of a SiNx or a CNx layer leads to the formation of hard coatings owing to suppression of the TiAlN grain growth, grain refinement, and a decrease of the surface roughness. The morphology of the coating changed from a columnar structure to a fine-grained structure when SiNx and CNx layers were formed.

2. The wear characteristics of the TiAlN/SiNx, TiAlN/CNx, TiAlSiN, and TiAlCrSiN multilayer coatings described in this study were improved compared with those of the TiAlN single layer coating. Furthermore, the tribological properties of the TiAlN and TiAlN/CNx coatings were improved owing to the deposition of CNx as the topmost layer, and the friction coefficients and size of wear scar of the coatings was decreased.

3. The wear of the TiAlN/SiNx, TiAlN + CNx, and TiAlN/CNx + CNx coatings in sliding systems was considerably reduced with the use of water as a lubricant by approximately two orders of magnitude compared with the performance under dry conditions. The wear of the coating was considerably reduced for all coatings in SRV testing under PAO lubrication conditions compared with the results obtained under dry and water conditions.

4. The tribological properties of the multilayer TiAlCrSiN-base coatings make these coatings effective at resisting wear and improved the cutting tool performance under wet conditions. The multilayer TiAlCrSiN coated drills outperformed the single layer TiAlN and multilayer TiAlSiN coated drills, which might be attributed to the multilayered structure of the TiAlCrSiN coating and to the improved tribological properties of the multilayer TiAlCrSiN coating owing to the incorporation Cr. The influence of the latter on cutting tool performance of the TiAlCrSiN coatings requires further investigation and will form part of our ongoing research into PVD coatings for dry machining in the automobile and aerospace industries.

Acknowledgements

This research was performed with the help of the graduate students at Nippon Institute of Technology.

Author details

Mei Wang[1]* and Shojiro Miyake[2]

*Address all correspondence to: mwang@osg.co.jp

1 Coating Research and Development, OSG Coating Service Co., Ltd. Aichi, Japan

2 Department of Innovative System Engineering, Nippon Institute of Technology, Saitama, Japan

References

[1] Hongmark S, Jacobson S, Larsson M. Design and evaluation of tribological coatings. Wear. 2000;**246**:20-33 https://doi.org/10.1016/S0043-1648(00)00505-6

[2] Miyake S. Tribology of carbon nitride and boron nitride nanoperiod multilayer film and its application to nanoscale processing. Thin Solid Films. 2005;**493**:160-169 https://doi.org/10.1016/j.tsf.2005.07.284

[3] Miyake S, Kaneko R. Microtribological properties and potential applications of hard, lubricating coatings. Thin Solid Films. 1992;**212**:256-261 https://doi.org/10.1016/0040-6090(92)90530-O

[4] Sakurai M, Toihara T, Wang M, Kurusaka W, Miyake S. Surface morphology and mechanical properties of nanoscale TiAlN/SiNx multilayer coating deposited by reactive magnetron

sputtering. Surface and Coating Technology. 2008;**203**:171-179 https://doi.org/10.1016/j.surfcoat.2008.08.060

[5] Nose M, Kawabata T, Khamseh S, Matsuda K, Fujii K, Ikeno S, Chiou WA. Microstructure and properties of TiAlN/a-C nanocomposite coatings prepared by reactive sputtering. Materials Transactions. 2010;**51**(2):282-287 http://doi.org/10.2320/matertrans.MC200913

[6] Kurosaka W, Shindo T, Wang M, Miyake S. Deposition and tribological properties of TiAlN/SiNx multilayer coatings. Journal of the Japan Society for precision engineering. 2012;**78–10**:905-911(in Japanese). http://doi.org/10.2493/jjspe.78.905

[7] Wang M, Toihara T, Sakurai M, Kurosaka W, Miyake S. Surface morphology and tribological properties of dc sputtered nanoscale multilayered TiAlN/CNx coatings. Tribology International. 2014;**73**:36-46 https://doi.org/10.1016/j.triboint.2014.01.008

[8] Miyake S, Watanabe S, Miyazawa H, Murakawa M, Miyamoto T, Kaneko R. Modification of nanometer scale wear of nitrogen-containing carbon films due to ion implantation. Nuclear Instruments and Methods in Physics Research. 1997;**B 122**:643-649. https://doi.org/10.1016/S0168-583X(96)00924-X

[9] Miyake S, Watanabe S, Miyazawa H, Murakawa M. Improved microscratch hardness of ion-plated carbon film by nitrogen inclusion evaluated by atomic force microscope. Applied Physics Letters. 1994;**65**(25):3206-3208 http://dx.doi.org/10.1063/1.112414

[10] Miyake S, Saito T, Wang M, Watanabe S. Tribological properties of extremely thin protective carbon nitride films deposited on magnetic discs by complex treatment. Journal of Engineering Tribology Part – J, Proceedings of the Institution of Mechanical Engineers. 2006;**220**(7):587-595. DOI: https://doi.org/10.1243/13506501JET124

[11] Wang M, Miyake S, Saito T. Nanoindentation and nanowear of extremely thin protective layers of C-N and B-C-N. Tribology International. 2005;**38**(6–7):657-664 https://doi.org/10.1016/j.triboint.2005.03.001

[12] Miyake S, Hashizume T, Kurosaka W, Sakurai M, Wang M. Deposition and tribology of carbon and boron nitride nanoperiod multilayer solid lubricating films. Surface and Coating Technology. 2007;**202**(4–7):1023-1028 https://doi.org/10.1016/j.surfcoat.2007.07.079

[13] Liu CS, Zheng ZY, DW W, Ye MS, Gao P, Peng YG, Fan XJ. Sliding friction and wear properties of CNx /TiN composite films. Tribology International. 2004;**37**(9):721-725 https://doi.org/10.1016/j.triboint.2004.03.001

[14] Zheng XH, Tu JP, Song RG. Microstructure and tribological performance of CN(x)–TiN(x) composite films prepared by pulsed laser. Material Design. 2010;**31**:1716-1719. https://doi.org/10.1016/j.matdes.2009.01.043

[15] Wang TS, DL Y, Tian YJ, Xiao FR, He JL, Li DC, Wang WK, Li L. Cubic-C3N4 nanoparticles synthesized in CNx/TiNx multilayer films. Chemical Physics Letters. 2001;**334**(1–3):7-11 https://doi.org/10.1016/S0009-2614(00)01251-3

[16] Liu ZJ, Vyas A, YH L, Shen YG. Structural properties of sputter-deposited CNx/TiN multilayer films. Thin Solid Films. 2005;**479**:31-37 https://doi.org/10.1016/j.tsf.2004.11.106

[17] Cao M, Li DJ, Deng XY, Sun X. Synthesis of nanoscale CNx/TiAlN multilayered coatings by ion-beam-assisted deposition. Journal of Vacuum Science and Technology. 2008;**A 26–5**:1314-1318. http://dx.doi.org/10.1116/1.2956627

[18] Riedo E, Chevrier J, Comin F, Brune H. Nanotribology of carbon based thin films: The influence of film structure and surface morphology. Surface Science. 2001;**477**:25-34 https://doi.org/10.1016/S0039-6028(01)00701-4

[19] Derflinger VH, Schutze A, Ante M. Mechanical and structure properties of various alloyed TiAlN-based hard coatings. Surface and Coatings Technology. 2006;**200**:4693-4700 https://doi.org/10.1016/j.surfcoat.2005.02.065

[20] Kao CM, Lee JW, Chen HW, Chan YC, Duh JG, Chen SP. Microstructures and mechanical properties evaluation of TiAlN/CrSiN multilayered thin films with different bilayer periods. Surface Coatings and Tehnology. 2010;**205**:1438-1443 https://doi.org/10.1016/j.surfcoat.2010.07.107

[21] Donohue LA, Smith IJ, Munz W-D, Petrov I, Greene JE. Microstructure and oxidation-resistance of Ti1-x-y-zAlxCryYzN layers grown by combined steered-arc/unbalance-magnetron-sputter deposition. Surface and Coating Technology. 1997;**94-95**:226-231

[22] Simth IJ, Munz W-D, Donohue LA, Petrov I, Greene JE. Improved Ti1-xAlxN PVD coatings for dry high speed cutting operations. Surface Coatings and Technology. 1998;**14-1**:37-41. http://dx.doi.org/10.1179/sur.1998.14.1.37

[23] Watanabe S, Noshiro J, Miyake S. Tribological characteristics of WS2/MoS2 solid lubricating multilayer films. Surface and Coating Technology. 2004;**183**:347-351 https://doi.org/10.1016/j.surfcoat.2003.09.063

[24] Thornton JA, Hoffman DW. Stress-related effects in thin films. Thin Solid Films. 1989;**171**:5-31 https://doi.org/10.1016/0040-6090(89)90030-8

[25] Nanostructured Coatings, Edited by, Part of the Nanostructure Science and Technology book series (NST). New York, NY: Springer. Print ISBN 978-0-387-25642-9. pp. 253-270 https://doi.org/10.1007/978-0-387-48756-4

[26] Veprek S, Reiprich S. A concept for the design of novel superhard coatings. Thin Solid Films. 1995;**268**:64-71 https://doi.org/10.1016/0040-6090(95)06695-0

[27] Niederhofer A, Bolom T, Nesladek P, Moto K, Eggs C, Patil DS, Veprek S. The role of percolation threshold for the control of the hardness and thermal stability of super- and ultrahard nanocomposites. Surface and Coating Technology. 2001;**183**:146-147 https://doi.org/10.1016/S0257-8972(01)01469-4

Chapter 6

Effects of Different Materials on the Tribological Performance of PVD TiN Films under Starved Lubrication Regime

Dong Jiang, Xiaoming Gao, Ming Hu, Desheng Wang, Yanlong Fu, Jiayi Sun and Lijun Weng

Additional information is available at the end of the chapter

http://dx.doi.org/10.5772/intechopen.75842

Abstract

Grit blasting is one simple but effective method to modify the morphology of material surface and can improve the tribological performance. In this study, a thick TiN film was prepared by arc ion plating on the steel disk treated with grit blasting, and the rough surface coated solid film was obtained. The tribological properties of solid film against different materials were evaluated under starved lubrication regime. The results showed that the friction coefficients of rough titanium nitride (TiN) films were lower than those of rough steel disks exclude alumina ball under starved lubrication, and the wear rates of TiN film were negligible due to the high hardness of TiN film and small contact area. For four kinds of balls including steel ball, silicon nitride, zirconia, and alumina, the wear scar diameter of steel ball is biggest, and the wear scar diameters of other balls are small. The hardness of steel ball is less than others, which results in the easy abrasion and increases the contact area to reduce the pressure. So the friction coefficient of TiN against steel is low and steady.

Keywords: TiN film, grit blasting, tribological properties, starved lubrication

1. Introduction

Titanium nitride (TiN) film is applied as a hard coating in industrial fields, which is prepared by physical vapor deposition (PVD), chemical vapor deposition (CVD), and thermal spraying techniques. Because of the B1 NaCl-type structure, titanium nitride exhibits some intrinsic

characteristics such as high hardness, high melting point, chemical stability, and wear resistance [1]. For these reasons, TiN is extensively used on cutting blades for longer service life, safe medical instruments, diffusion barrier in semiconductor apparatuses and architectural decoration fields, and so on.

As one wear-resistant coating, the coefficient of friction and wear rate of TiN films are high under dry friction conditions. Efforts to improve the tribological properties of TiN have included changed deposition parameter and doped chemical elements during the film preparation [2–5], surface treatments, and modifications during film post-processing [6–9].

Surface treatments are applied extensively to improve the mechanical properties and tribological performance of many materials, which contain anodizing and hard anodizing, laser texture, mechanical rough, surface hardening, and so on. Among all the methods, blasting with different particles, as one kind of surface treatment technologies, is an effective low-cost surface-modifying method, which can be used to enhance the mechanical character in biomedical [10], automotive [11, 12], aerospace sectors [13], and other industrial applications [14, 15].

Blasting with different particles can enhance mechanical properties of many materials and protected coatings. Lee found that the shear loads for the Al5052/CFRP composites fabricated with treated Al5052 sheet, of which surface roughness (Ra) values were 1.84 and 4.25 μm, were three and five times higher than that of the composite fabricated by using the untreated sheet with Ra value of 0.73 μm, and the bending stress increased from 200 to 400 MPa [12]. During cold rolling process, weight losses for steel sheets finished by conventional acid pickling was greater than those of steel sheets finished using shot blasting [16]. Shot blasting treatment can improve the steam oxidation resistance of austenitic steel compared with previous report [17]. Abusuilik has investigated the effects of various surface treatments on the properties and performance of the hard coating, and found that material transfer and build-up at the coating surface were higher for the surfaces treated by grinding and shot blasting than those treated by other methods [18]. During the open pore metallic foam core sandwich panels prepared by thermal spraying of a coating, Salavati found that the coating porosity and adhesion strength were determined by the substrate surface roughness, which could be controlled by grit-blasting parameters [14]. Other studies of modified surface in metal substrates and some hard coatings on tribological properties are carried out under fully flood lubrication condition. Nakano investigated the effect of pattern texture by grit-blasting method for their tribological properties [19]. Groove pattern texture suppressed the generation of the hydrodynamic pressure, and the lubricating condition of the tests became boundary lubrication. Because the lubrication film became thicker and the hydrodynamic lubrication region was expanded for dimple pattern texture, the lower friction coefficient was lower than that of groove pattern texture. Additionally, some investigations of modified surface under starved lubrication are carried out in last decade, such as laser texture on steel [20, 21], copper [22], hard coatings [23], and piston ring-cylinder [24].

However, only limited studies can be found in the literature associated with the friction and wear behavior of physical vapor deposited TiN film covered the grit-blasting steel substrate sliding against different materials under starved lubrication regime. This paper was investigated the tribological performance of different friction pairs under starved lubrication regime after grit blasting. And the tribological mechanism for different materials was discussed.

http://dx.doi.org/10.5772/intechopen.75842

2. Experimental methods

2.1. Grit blasting and TiN film prepared

AISI 440c stainless steel was chosen as substrate for sand blasting and TiN film prepared. Before grit blasting, the stainless steel substrate was grinded with emery papers and rinsed with acetone and ethanol to get rid of impurity. Grit blasting was carried by a handheld sand blasting machine (China, JICHAN TECH) using 60# Al_2O_3 particles (diamond 300 μm, JICHAN TECH). After then, the morphology of steel substrate was characterized by a JSM-5600LV scanning electron microscope, which attaches with energy disperse spectrometer.

The hard titanium nitride film was prepared using ion plated technology with Hauzer Flexicoat 1200 coating. The deposition parameters were following: 60 A of arc current, 200 V of bias volt, 400 centigrade degree of steel disks, 100 min of deposition time, and 1.8 Pa of N_2 pressure.

2.2. Friction tests

Friction tests were conducted to evaluate the tribological properties of hard TiN film covered the grit-blasting steel substrate against four different material ball counterbodies using a ball-on-disk tribo-tester under starved lubrication regime. The four different upper balls were made of bearing steel, silicon nitride, alumina, and zirconia, which diameter is 8 mm. And the hardness of bearing steel was lower than those of TiN film and other materials. The diameter of the lower disk covered with TiN film was 24 mm. The surface roughness of the test sample was measured with the Micro-Map surface mapping microscope. The initial average surface roughnesses (Ra) of all the upper balls are less than 0.03 μm, and the roughness of lower disk covered TiN film was 8.2 μm which was much higher than upper balls. Friction tests were carried out in ambient temperature and atmospheric environment for 120 min of duration under 5 N of normal load and sliding speed of 31 m/min. The coefficient of friction was recorded automatically during the friction test.

In order to obtain the starved lubrication regime, the small amount of lubricating oil was injected the surface of lower TiN film-covering disk. The calculated thickness of oil film was lower to 3 μm. After friction tests, all the balls and disks were cleaned with acetone by ultrasonic washer for three times. The typical surface morphologies and chemical compositions of friction tracks in lower disks and wear scars in upper balls were analyzed by scanning electron microscopy (SEM), which attached an energy dispersive spectrometer.

3. Results and discussion

3.1. Morphology and roughness

After grit blasting, the substrate surface is nonmetal shiny and matte-like. The surface morphology of as-obtained grit-blasting steel substrate was shown in **Figure 1**. It can be seen that surface roughness of the steel substrate was enlarged obviously than the polished samples.

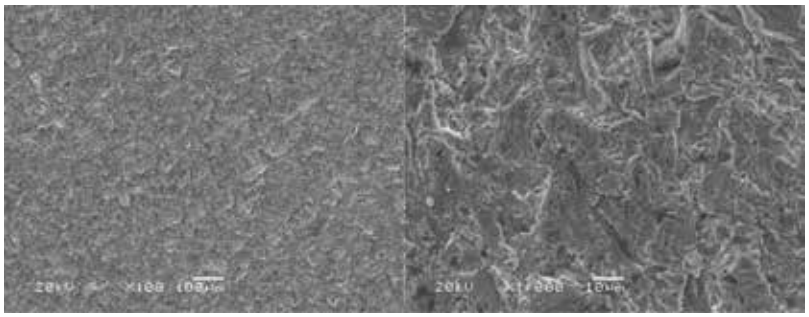

Figure 1. The morphology of grit-blasting steel substrate.

However, there are not clearly defects and concave pits in the substrate surface. The average Ra value of steel substrate and polished samples are 7.5 and 0.03 μm. Grit-blasting substrate was larger than that of polished sample.

The surface morphology of ion plating TiN film covered a grit-blasting substrate is shown in **Figure 2**. Compared with the surface morphology before covered TiN films, there is not notable difference for surface morphology of TiN-covered samples. The average Ra value of as-prepared TiN film covered grit-blasting steel substrate was 8.2 μm, which is similar to that of grit-blasting substrate. The film thickness of TiN film is 4 μm, which is measured with the profile meter.

3.2. Friction test results

The histogram of average friction coefficient of grit-blasting steel substrate and TiN films sliding against with different upper balls was shown in **Figure 3**. Because of the shorter friction duration for only few minutes, the average friction coefficient of alumina ball is not presented in the figure. For three other different balls, the average friction coefficient of silicon nitride ball against grit-blasting steel substrate is as same as that of silicon nitride ball sliding against TiN films. The average friction coefficients of TiN films were lower than those of grit-blasting steel substrate for steel ball and zirconia ball under the same lubrication conditions.

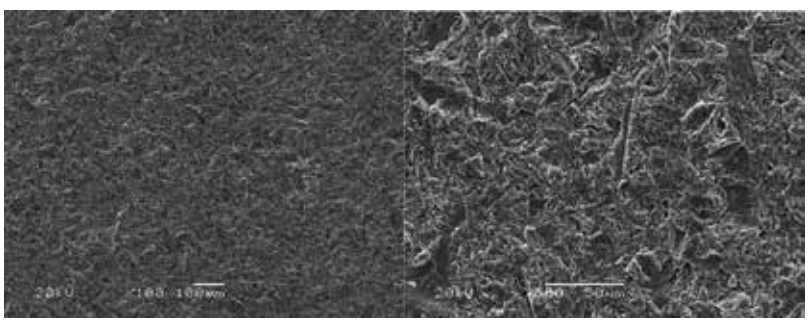

Figure 2. Surface morphology of ion plating TiN film covered the grit-blasting substrate.

http://dx.doi.org/10.5772/intechopen.75842

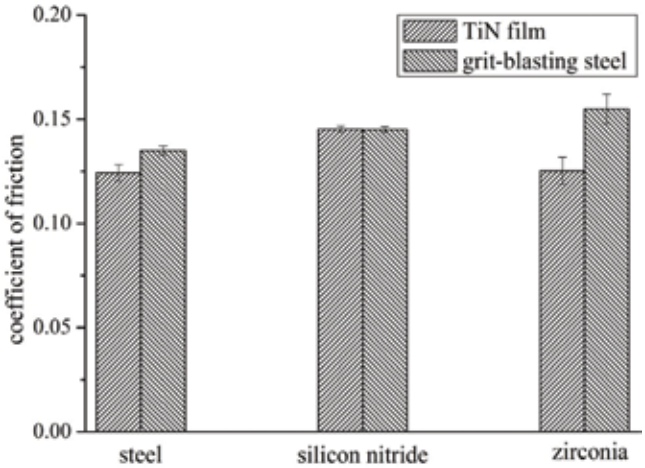

Figure 3. Histogram of average friction coefficient of grit-blasting steel substrate and TiN film sliding against with different upper balls.

The average friction coefficients of TiN film and grit-blasting steel substrate sliding against steel ball were 0.125 and 0.135, respectively, which reduced by 7%. For zirconia ball, the average friction coefficients of TiN film and grit-blasting steel substrate were 0.125 and 0.155, respectively, which reduced by 19%.

The tribological properties of grit-blasting steel and TiN film against four different upper balls were carried out by a rotating tribometer with ball-on-disk of configuration. The coefficient of friction of grit-blasting steel substrate was shown in **Figure 4**. For different upper balls, their friction behaviors are different. The friction duration of alumina balls is worse than steel, zirconia, and silicon nitride balls. The friction duration was only 2 min when the coefficient of friction is over the limited value. During the alumina ball sliding against grit-blasting steel disk, its coefficient of friction was 0.13 and increased drastically after 1 min. Its friction duration was very shorter than other balls. For other different upper balls of steel, silicon nitride and zirconia balls, they exhibited the similar trend that the coefficient of friction elevated gradually and reached the steady value of 0.17. However, the friction duration of three different upper balls is as long as 120 min, the reaching time of steady-state friction coefficient is different. The coefficient of friction raised to steady state for steel ball after 50 min. For silicon nitride and zirconia balls, the times to reach the steady-state friction coefficient are 10 and 25 min, respectively.

The real-time friction coefficients of TiN films covered grit-blasting steel substrate against four different upper balls are shown in **Figure 5**. The friction coefficient of TiN film against alumina ball elevated drastically and over the limited value of friction coefficient for a very short time, which was similar with the trend of grit-blasting steel substrate against alumina ball. For three other upper balls, the friction duration of TiN films can last with a steady-state friction coefficient until friction experiment ended up. However, the undulations of friction coefficient of TiN films sliding against silicon nitride, steel, and zirconia balls are smaller than those of grit-blasting steel disks.

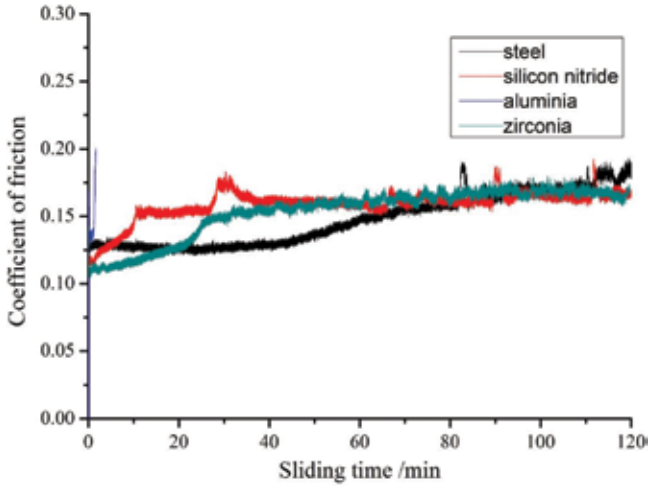

Figure 4. The coefficient of friction of grit blasting steel-disk sliding against different upper balls.

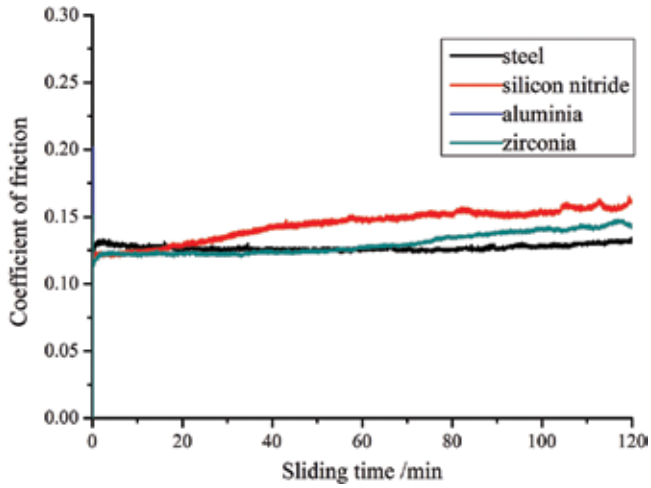

Figure 5. The coefficient of friction of TiN films sliding against different upper balls.

3.3. Surface analysis

Figure 6 shows the surface morphology of wear track in TiN film and upper steel ball under the starve lubrication regime. It is not seen that there is notable wear trace in the track from the low-resolution figure, which amplification is 100. However, there is some smooth pit in the wear track from the high-resolution figure, which amplification is 500. It can be attributed to the transfer phase from the upper steel ball and the plastic deformation of micro-bulge in the lower steel substrate. Because TiN is much hard than the soft steel ball, so the TiN film covered the grit-blasting steel substrate plays a similar role of sandpaper for upper steel ball. It is confirmed from the surface morphology of upper steel ball that there is a round wear scar with the diameter of 0.63 mm in the upper steel ball. The bigger wear scar of steel ball can result in reduced normal pressure, so the friction coefficient of TiN film against steel ball was steady.

http://dx.doi.org/10.5772/intechopen.75842

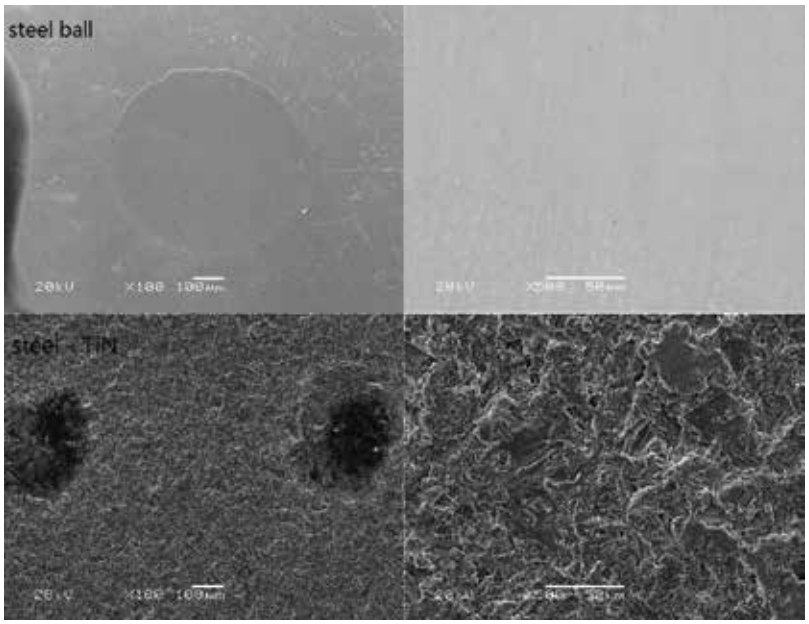

Figure 6. The morphology of wear track in TiN film and wear scar in upper steel ball after friction tests under the starve lubrication regime.

The surface morphology of wear track in TiN film and wear scar in upper silicon nitride ball were shown in **Figure 7**. It is seen that there is not obvious wear and more smooth pits in the wear track of TiN film. There is a wear scar with the diameter of 0.37 mm in the upper silicon nitride ball. Although both titanium nitride and silicon nitride are very hard materials, the micro-bulge in the lower rough disk could be deformed under high pressure. This resulted in the bigger real contact area, which means the friction force of among all the micro-bulge with upper ball increased. It is confirmed that the real-time friction coefficient raised during the later stage of the friction tests.

The surface morphology of wear track in TiN film and wear scar in upper zirconia ball are shown in **Figure 8**. It is also seen that there is not obvious wear and more smooth pits in the wear track of TiN film, which is similar with the wear track of TiN film sliding against silicon nitride ball. There is a wear scar with the diameter of 0.32 mm in the upper zirconia ball. Very small pores can be found in the wear scar of upper ball. These pores could absorb the lubricating oils on the surface of lower disk. During the sliding process, the absorbed oils in the pores can improve tribological properties by avoiding the direct contact of rubbing surface. So, the friction coefficient of TiN film against ZrO_2 was steady.

The surface morphology of wear track of TiN film and wear scar in upper alumina ball is shown in **Figure 9**. Compared with the negligible wear of other different ball, there is obvious wear trace from the low-resolution figure and bigger smooth contact area from the high-resolution figure in the TiN film. The bigger the contact area is, the bigger the friction force between the contact interface. So, the friction coefficient increases during the sliding process. There is a very small wear scar in the alumina ball as compared to the wear scars in the other different upper balls. It means that the material in the smooth contact area is from the lower disk and lubricating oil, not upper ball.

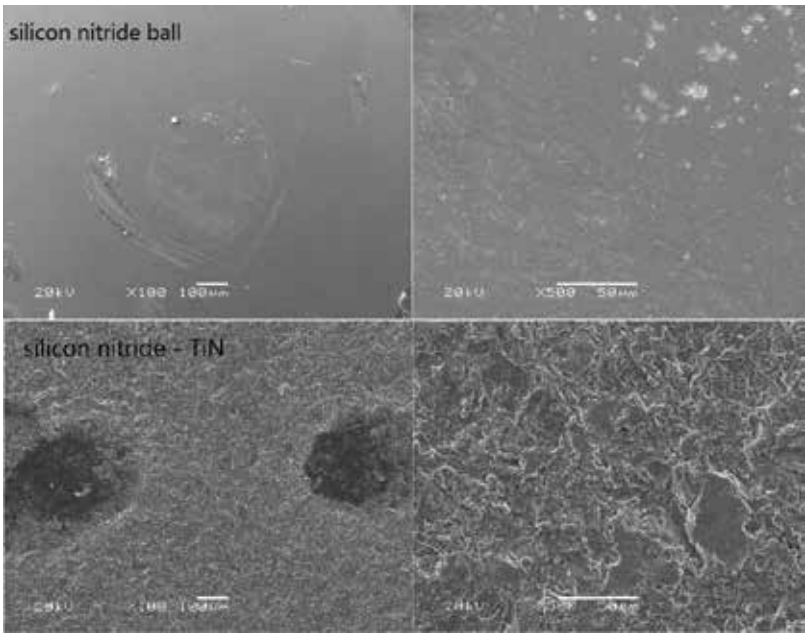

Figure 7. Morphology of wear track in TiN film and wear scar in upper silicon nitride ball after friction tests under the starve lubrication regime.

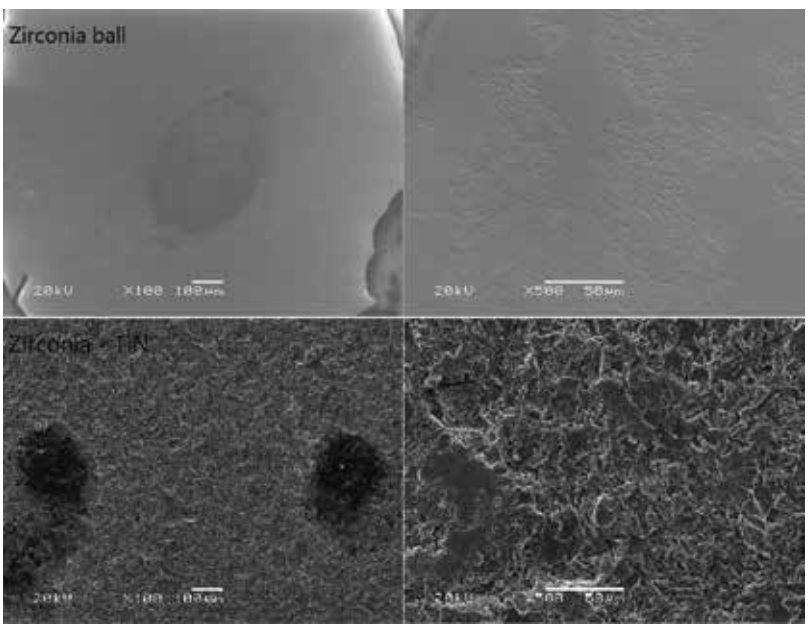

Figure 8. The morphology of wear track in TiN film and wear scar in upper zirconia ball after friction tests under the starve lubrication regime.

http://dx.doi.org/10.5772/intechopen.75842

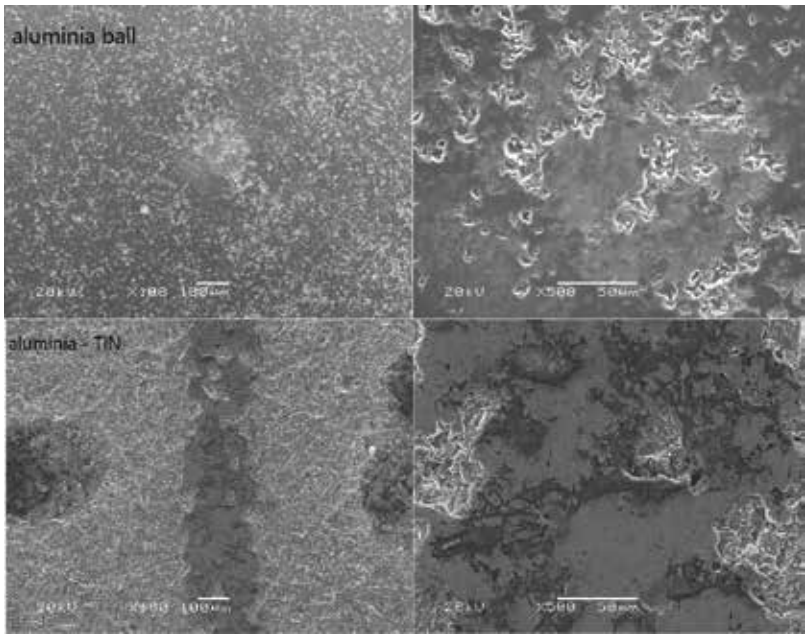

Figure 9. The morphology of wear track in TiN film and wear scar in upper aluminia ball after friction tests under the starve lubrication regime.

The tribological performance of friction pairs is attributed to many factors, such as the natural lubricating characteristic, the physic-chemical properties of different materials, the content of lubricating oil, experiment conditions, and so on. In this paper, however, the average oil thickness is 3 μm before the test, the real oil content about the contact area is more as compared to before the test because of the aggregation effect of lubricating oil caused by the surface free energies of different materials.

For the four kinds of upper balls, the lubricating abilities are different. Both zirconia and silicon nitride could exhibit better self-lubricating performance than alumina and steel. So, the friction durations of zirconia and silicon nitride are longer than alumina when they slid with TiN film under starved lubrication conditions. For one steel ball, its hardness is much smallest in all of the test balls. And the steel ball was worn in the sliding process.

4. Conclusion

One thick TiN film was prepared by ion-plated technology on the grit-blasted steel substrate. The tribological performance was evaluated with four upper balls made up of different materials under the starved lubrication regime. Compared with their higher friction coefficients for grit-blasting steel against different balls, the friction coefficients for TiN films on the grit-blasting steel were lower and steady. It was due to the hardness of TiN film and small contact

area in the contact zone. During the sliding process, the strong load capacity of TiN films ensures the negligible wear rate, and the small contact area between of the friction pairs plays an important role in the steady friction coefficient.

Acknowledgements

This work was supported by China National Natural Science Foundation (Grant no. 51505463).

Author details

Dong Jiang*, Xiaoming Gao, Ming Hu, Desheng Wang, Yanlong Fu, Jiayi Sun and Lijun Weng

*Address all correspondence to: jiangd@licp.cas.cn

State Key Laboratory of Solid Lubrication, Lanzhou Institute of Chemical Physics, Chinese Academy of Sciences, Lanzhou, China

References

[1] Santecchia E, Hamouda AMS, Musharavati F, Zalnezhad E, Cabibbo M, Spigarelli S. Wear resistance investigation of titanium nitride-based coatings. Ceramics International. 2015;**41**(9):10349-10379. DOI: 10.1016/j.ceramint.2015.04.152

[2] Luo Q, Yang S, Cooke KE. Hybrid HIPIMS and DC magnetron sputtering deposition of TiN coatings: Deposition rate, structure and tribological properties. Surface & Coatings Technology. 2013;**236**:13-21. DOI: 10.1016/j.surfcoat.2013.07.003

[3] de La Roche Yepes J, Gonzalez Carmona JM, Ruden MA, Restrepo Parra E, Sequeda OF. Mechanical, and tribological properties of TI/TIN bilayers: The dependence of TI interlayer thickness. Dyna-Colombia. 2013;**80**(178):115-122

[4] Akkaya SS, Vasyliev VV, Reshetnyak EN, Kazmanli K, Solak N, Strel'nitskij VE, Urgen M. Structure and properties of TiN coatings produced with PIII&D technique using high efficiency rectilinear filter cathodic arc plasma. Surface & Coatings Technology. 2013;**236**:332-340. DOI: 10.1016/j.surfcoat.2013.10.009

[5] Braic V, Vladescu A, Balaceanu M, Luculescu CR, Braic M. Nanostructured multi-element (TiZrNbHfTa)N and (TiZrNbHfTa)C hard coatings. Surface & Coatings Technology. 2012;**211**:117-121. DOI: 10.1016/j.surfcoat.2011.09.033

[6] Coblas DG, Fatu A, Maoui A, Hajjam M. Manufacturing textured surfaces: State of art and recent developments. Proceedings of the Institution of Mechanical Engineers Part J-Journal of Engineering Tribology. 2015;**229**(1):3-29. DOI: 10.1177/1350650114542242

[7] Demir AG, Pangovski K, O'Neill W, Previtali B. Laser micromachining of TiN coatings with variable pulse durations and shapes in ns regime. Surface & Coatings Technology. 2014;**258**:240-248. DOI: 10.1016/j.surfcoat.2014.09.021

[8] Demir AG, Previtali B, Lecis N. Development of laser dimpling strategies on TiN coatings for tribological applications with a highly energetic Q-switched fibre laser. Optics and Laser Technology. 2013;**54**:53-61. DOI: 10.1016/j.optlastec.2013.05.007

[9] Demir AG, Lecis N, Previtali B, Ugues D. Scratch resistance of fibre laser surface textured TiN coatings. Surface Engineering. 2013;**29**(9):654-659. DOI: 10.1179/174329413x13614824551916

[10] Lieblich M, Barriuso S, Multigner M, Gonzalez-Doncel G, Gonzalez-Carrasco JL. Thermal oxidation of medical Ti6Al4V blasted with ceramic particles: Effects on the microstructure, residual stresses and mechanical properties. Journal of the Mechanical Behavior of Biomedical Materials. 2016;**54**:173-184. DOI: 10.1016/j.jmbbm.2015.09.032

[11] Sun L, Li CA, Tu JW, Peng MC. Effect of surface treatment to inserted ring on Al-Fe bonding layer of aluminium piston with reinforced cast iron ring. Journal of Central South University. 2014;**21**(8):3037-3042. DOI: 10.1007/s11771-014-2273-0

[12] Lee MS, Kim SJ, Lim OD, Kang CG. Effect of surface roughness of Al5052/CFRP composites on adhesion and mechanical properties. Asian Journal of Chemistry. 2014;**26**(17):5871-5878. DOI: 10.7234/composres.2013.26.5.295

[13] Encinas N, Oakley BR, Belcher MA, Blohowiak KY, Dillingham RG, Abenojar J, Martinez MA. Surface modification of aircraft used composites for adhesive bonding. International Journal of Adhesion and Adhesives. 2014;**50**:157-163. DOI: 10.1016/j.ijadhadh.2014.01.004

[14] Salavati S, Coyle TW, Mostaghimi J. Optimization of grit-blasting process parameters for production of dense coatings on open pores metallic foam substrates using statistical methods. Journal of Thermal Spray Technology. 2015;**24**(7):1246-1255. DOI: 10.1007/s11666-015-0291-6

[15] Piasecka M. Laser texturing, spark erosion and sanding of the surfaces and their practical applications in heat exchange devices. Advanced Materials Research. 2014;**874**:95-100. DOI: 10.4028/www.scientific.net/AMR.874.95

[16] Labiapari WD, de Alcantara CM, Costa HL, De Mello JDB. Wear debris generation during cold rolling of stainless steels. Journal of Materials Processing Technology. 2015;**223**:164-170. DOI: 10.1016/j.jmatprotec.2015.03.050

[17] Liang ZY, Zhao QX, Singh PM, Wang YG, Li YX, Wang YS. Field studies of steam oxidation behavior of austenitic heat-resistant steel 10Cr18Ni9Cu3NbN. Engineering Failure Analysis. 2015;**53**:132-137. DOI: 10.1016/j.engfailanal.2015.02.019

[18] Abusuilik SB. Pre-, intermediate, and post-treatment of hard coatings to improve their performance for forming and cutting tools. Surface & Coatings Technology. 2015;**284**:384-395. DOI: 10.1016/j.surfcoat.2015.07.003

[19] Nakano M, Korenaga A, Korenaga A, Miyake K, Murakami T, Ando Y, Usami H, Sasaki S. Applying micro-texture to cast iron surfaces to reduce the friction coefficient under lubricated conditions. Tribology Letters. 2007;**28**(2):131-137. DOI: 10.1007/s11249-007-9257-2

[20] Xiong DS, Qin YK, Li JL, Wan Y, Tyagi R. Tribological properties of PTFE/laser surface textured stainless steel under starved oil lubrication. Tribology International. 2015;**82**:305-310. DOI: 10.1016/j.triboint.2014.07.017

[21] Mishra SP, Polycarpou AA. Tribological studies of unpolished laser surface textures under starved lubrication conditions for use in air-conditioning and refrigeration compressors. Tribology International. 2011;**44**(12):1890-1901. DOI: 10.1016/j.triboint.2011.08.005

[22] Li KM, Yao ZQ, Hu YX, Gu WB. Friction and wear performance of laser peen textured surface under starved lubrication. Tribology International. 2014;**77**:97-105. DOI: 10.1016/j.triboint.2014.04.017

[23] Zhang KD, Deng JX, Xing YQ, Li SP, Gao HH. Effect of microscale texture on cutting performance of WC/Co-based TiAlN coated tools under different lubrication conditions. Applied Surface Science. 2015;**326**:107-118. DOI: 10.1016/j.apsusc.2014.11.059

[24] Grabon W, Koszela W, Pawlus P, Ochwat S. Improving tribological behaviour of piston ring-cylinder liner frictional pair by liner surface texturing. Tribology International. 2013;**61**:102-108. DOI: 10.1016/j.triboint.2012.11.027

Chapter 7

Lubrication and Friction of Porous Oil Bearing Materials

Yanguo Yin and Guotao Zhang

Additional information is available at the end of the chapter

http://dx.doi.org/10.5772/intechopen.72620

Abstract

In order to address poor lubrication of porous bearings due to the seepage flow of oil into the porous medium, multi-layered sintered composite bearings have been developed. Multi-layered bearings achieve a combination of high strength and good lubrication. Lubrication model of the porous multi-layer materials in polar coordinates was established based on Darcy's law. And the effect of surface Darcy flow and porous structure on the lubrication capacity were discussed by using the finite difference method. In the end, the tribology experiments of the multi-layer materials were presented on the end face tribo-tester to verify the simulation results. Results show that the lubrication performance of the multi-layer materials is better than that of the single layer materials. With the decrease of the surface porosity, the lubrication performance becomes better in the given range of surface layer. Also, it can be significantly improved if considering the surface Darcy flow. Within a certain range, the effects of surface Darcy flow on lubrication performance are more obviously with higher speed. There is a good agreement between the numerical analysis and the measurement. Research work provides a theoretical basis for analysis and design of multi-layer sintering bearing material.

Keywords: lubrication, friction, porous bearing, multi-layer materials, Darcy law

1. Introduction

Oil bearings with porous matrix have been widely used in industrial applications for its low manufacturing cost and oil self-lubricating properties [1]. As the counterpart picks up speed, the oil impregnated in the porous bearing exuded to the surface and the hydrodynamic oil film formed. Therefore, the oil storage capacity and lubrication performance have an important influence on the operating characteristic of oil bearing [2]. Over the past decades, a considerable number of theoretical models have been proposed on the lubrication characteristic by several researchers. The hydrodynamic theory of porous journal bearings was studied

originally by Morgan and Cameron, who gave a solution for a short bearing based on Darcy model [3]. Later, Darcy's equations were extensively used in the study of the lubrication characteristic of oil bearing. The unsteady state, non-Newtonian effect and rough surface were coupling to the lubrication model to improve the numerical accuracy [4–9]. These studies were all focused on single-layer bearing materials, without considering the change porosity in the thickness direction. Meurisse [10] and Usha [11] found that reducing the porosity can prevent the oil leaking into the porous medium and improve the bearing strength and hydrodynamic capacity. But the decreased porosity leads to the decrease of oil content and then will deteriorates the self-lubrication performance. Therefore, it can be concluded that the coexistence of high strength and good lubrication characteristics of the porous bearing are difficult to achieve. This is the biggest problem that oil bearing has encountered in the industrial application. Hence, adjusting the permeability of bearing reasonably is the key to improve the lubrication property. Based on the above studies, Naduvinamani [12] and Rao [13] discussed the effect of the multi-layer structure parameters on the lubrication property, which promoted the theoretical development of the oil bearing. This multiple-layer structure is useful, as it would not only increase the load capacity of the bearing because of reduced oil seepage into its wall but would also help to bring oil between the surfaces, thereby improving the bearing performance when saturated with oil Inadequately. But for now, there is no systematic research on the multi-layer oil bearing materials compared with the single-layer sintered materials. Especially, most researchers ignored the surface Darcy flow to simply the boundary condition in the previous work. It did not coincide with the homogeneity and isotropy hypothesis, which will undoubtedly have a bad effect on the analysis accuracy. In this paper, the multi-layer oil bearing composites with different porosities were made to achieve the unification of high strength and good lubrication property. Hydrodynamic lubrication model of the porous bearing in polar coordinate system was established based on Darcy's law. The effect of surface Darcy flow and porous structure on the lubrication property were also discussed. In the end, the tribology experiments of the multi-layer materials were presented on the end face tribotester to verify the simulation results.

2. Lubrication model of the multi-layer sintered material

The physical configuration of the multi-layer bearing system is shown in **Figure 1**. As shown in **Figure 1**, the porous disk bearing ($\phi 34 \times 4$ mm) prepared by powder metallurgy is fixed. And the counterpart rotates at the angular velocity ω. T_1 and T_2 are the thicknesses of the surface and bottom layers. Similarly, k_1 and k_2 are the permeability of the two layers respectively. The o-x-y-z coordinate system is built on the surface of the porous bearing. Assuming that the counterpart surface is smooth. While the bearing surface has a sinusoidal roughness. The fluid film thickness h can be shown as

$$h = h_0 + \delta_0 \sin(2b\pi r) \sin(c\theta) \tag{1}$$

where the minimum film thickness h_0 equal to 10 μm, and the height of the roughness asperity δ_0 equal to 2 μm. The characters b and c represent rough peaks in radial and circumferential directions, respectively.

http://dx.doi.org/10.5772/intechopen.72620

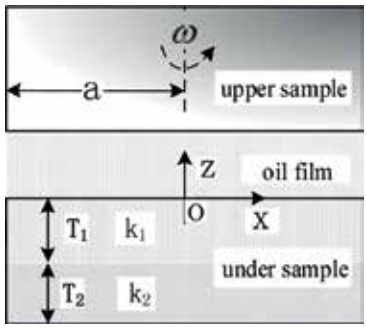

Figure 1. Two rotary parallel disc samples.

If take b equal to 2 and take c equal to 8, the film thickness is show in **Figure 2**.

Suppose the porous matrix is homogeneous and isotropic. That means the permeability is equal in any coordinate direction. The flow in porous matrix is governed by the Darcy's law.

$$U_0 = \frac{k_1}{\eta}\frac{\partial p}{\partial x}; V_0 = \frac{k_1}{\eta}\frac{\partial p}{\partial y}; W_0 = -\frac{k_1}{\eta}\left(T_1 + \frac{k_2}{k_1}T_2\right)\left(\frac{\partial^2 p}{\partial x^2} + \frac{\partial^2 p}{\partial y^2}\right) \tag{2}$$

where η is the fluid viscosity, and p is the fluid pressure in porous matrix.

Owing to the fluid continuity in the porous bearing, the pressure p satisfies the Laplace equation

$$\frac{\partial^2 p}{\partial x^2} + \frac{\partial^2 p}{\partial y^2} + \frac{\partial^2 p}{\partial z^2} = 0 \tag{3}$$

Integrating the continuity Eq. (3) over the fluid film thickness and using the Eq. (2) as the velocity conditions, the general Reynolds equation can be obtained. By the coordinate transform technology, the Reynolds equation under the polar coordinate shown as

$$\frac{\partial}{\partial r}\left[r\lambda\frac{\partial p}{\partial r}\right] + \frac{\partial}{r\partial\theta}\left[\lambda\frac{\partial p}{\partial\theta}\right] = -6\eta\omega r\frac{dh}{d\theta} \tag{4}$$

where $\lambda = h^3 - 6hk_1 - 12k_1T_1 - 12k_2T_2$. And the surface Darcy flow in the three coordinate directions are all considered.

Similarly, the Reynolds equation without surface Darcy flow shown as

$$\frac{\partial}{\partial r}\left[r\xi\frac{\partial p}{\partial r}\right] + \frac{\partial}{r\partial\theta}\left[\xi\frac{\partial p}{\partial\theta}\right] = -6\eta\omega r\frac{dh}{d\theta} \tag{5}$$

where $\xi = h^3 - 12k_1T_1 - 12k_2T_2$.

As we all know, the internal powder particles are sintered at high temperature during the preparation of the oil bearing by powder metallurgy technology. The pores between the spherical particles are connected with each other to form the porous channels of the oil bearing, which is consistent with the modeling idea of the Kozeny–Carman equation. So the

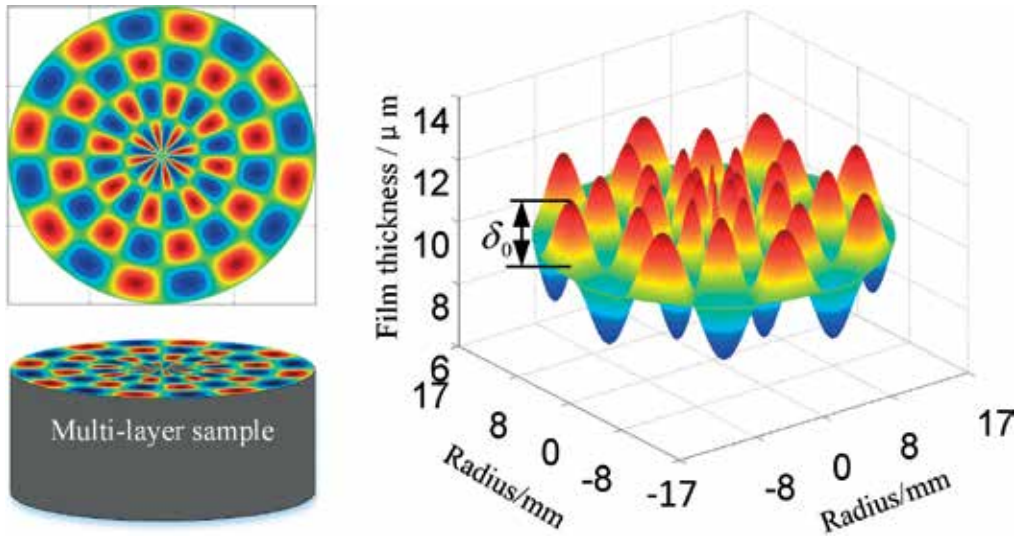

Figure 2. Film thickness.

relationship between pore structure and fluid pressure drop is often represented by Kozeny–Carman equation. Supposing that the porous bearing material is composed of tiny spherical particles with an average diameter of Dc, the permeability of the bearing can be described as

$$k_i = \frac{D_c^2 \varphi_i^3}{180(1-\varphi_i)^2} \tag{6}$$

where φ_i is the porosity of surface and substrate layers of the porous bearing.

The boundary condition shown as.

$$p|_{r=a} = 0; p_{\theta=0} = p_{\theta=2\pi} \tag{7}$$

where a is the outer radius of the disc bearing.

3. Results and analysis

In the present study, the lubrication model of the multi-layer porous bearing under polar coordinate system was established. The combined effects of the roughness, surface Darcy flow and porous structure on the lubrication performance have been studied. The following data given as: $\varphi_i = 8$ or 10%, $D_c = 1 \times 10^{-4} \sim 5 \times 10^{-4}$m, $T_i = 0.002$ m, $\eta = 0.02$ Pa · s.

3.1. Effect of surface Darcy flow on lubrication property

Figure 3 shows the effect of the surface Darcy flow on the hydrodynamic pressure. The pressure distributions with surface Darcy and without surface Darcy flow are shown in **Figure 3(a)** and **(b)**, respectively. The effect of surface Darcy flow on pressure distribution under different speeds are shown in **Figure 3(c)** and **(d)**. As can be seen from **Figure 3**, the

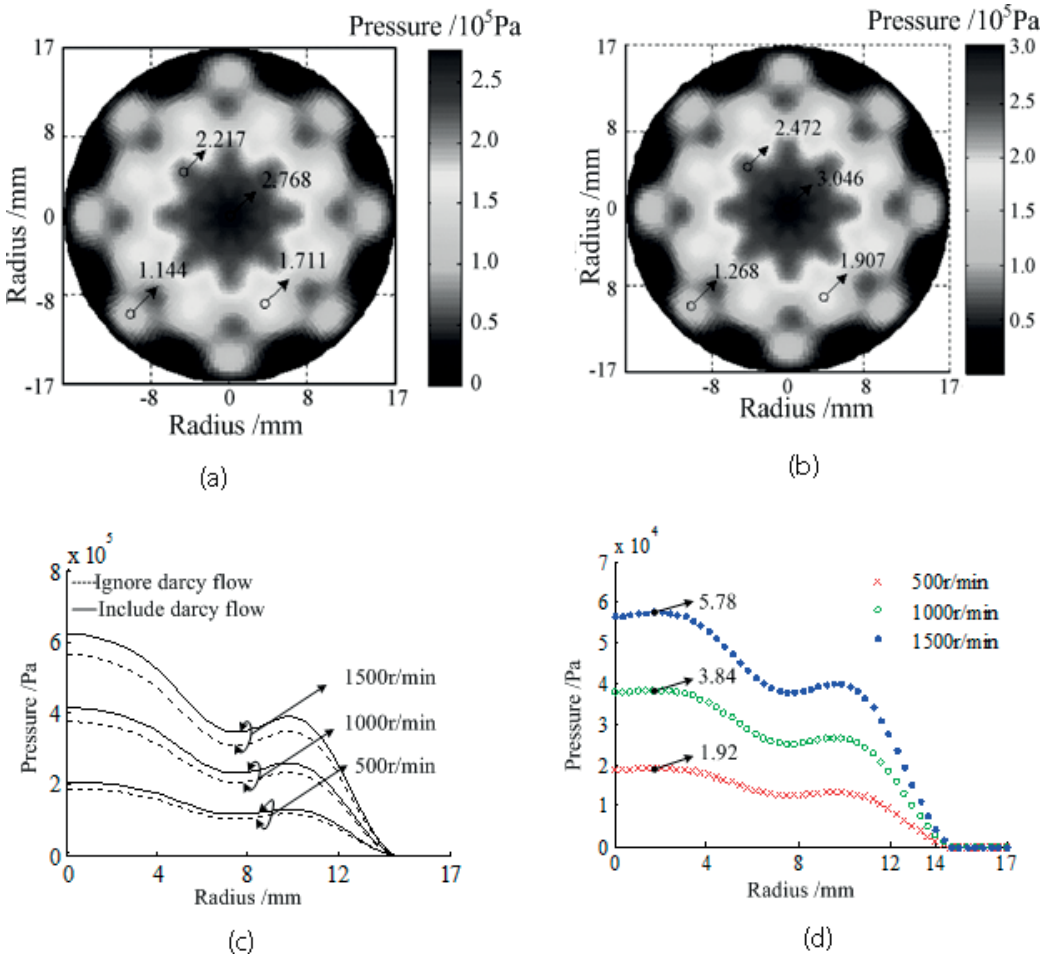

Figure 3. Effect of surface flow on pressure and its amplification in varied speeds. (a) Pressure with no surface flow (b) Pressure with surface flow (c) Pressure distribution (d) The pressure amplification.

pressure also presents a sine form, similarly to the film thickness distribution. The maximum pressure occurs at the center of the porous circle surface, and the minimum occurs at the outer circle. In addition, the oil film pressure increases with the increase of speed, and the pressure is higher if take the rough surface Darcy flow into consideration in every instantaneous speed. As shown in **Figure 3(d)**, the pressure amplification increases with the increase of speed along the radius direction. And it is more obvious that the effect of the surface Darcy flow on the pressure amplification with the increase of speed. The maximum pressure amplifications in three speeds are 1.92×10^4, 3.84×10^4, 5.78×10^4 Pa, respectively.

Figure 4 illustrates the variation of the load capacity and friction coefficient with the speeds. It is observed that the surface Darcy flow has obvious significance to the lubrication property. The property turns better when considering the surface flow. And its effect becomes obvious with the increase of speed. For example, when the speed is 1500 r/min, the load capacity caused by surface Darcy flow increases by 11.64%. Moreover, the lubrication property of single

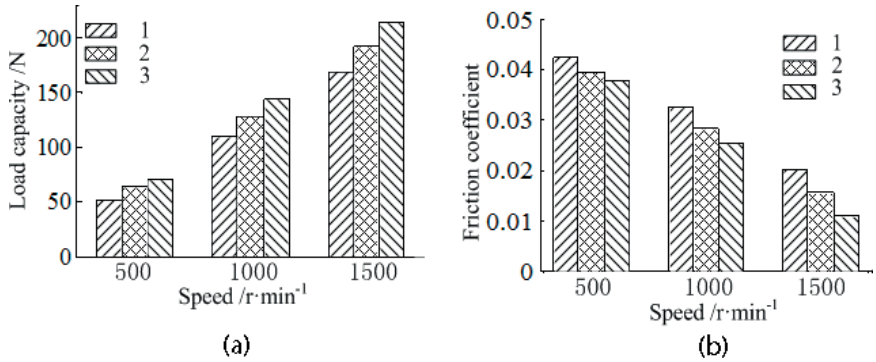

Figure 4. Effect of surface Darcy flow on the friction coefficient in different speeds. (a) Carrying capacity (b) Friction coefficient. Note: 1 denote monolayer material ignored Darcy flow; 2 denote multi-layer material ignored Darcy flow; 3 denote multi-layer material included Darcy flow.

and double layer oil bearings is improved with the increase of velocity. And the property of the multi-layer bearing is better than that of the single layer. In the single layer oil bearing, the oil driven by the hydrodynamic pressure penetrates into the porous medium easily, which weaken the oil thickness and the lubrication property. In the multi-layer oil bearing, the dense surface could prevent the fluid seepage into the porous bearing. Therefore, a thicker lubricant film can be formed between the friction pairs. And the multi-layer bearing with dense surface has better property than that of the single layer bearing.

3.2. The experimental verification

Figure 5 shows the variation of the dimensionless load capacity and friction coefficient with the aperture for different porosities of the two layers. It is observed that negatively increasing values of the dimensionless load capacity increase the aperture of the two layers, whereas positively increasing values of the friction coefficient increase the aperture of the two layers. Thus raising the aperture of the two layers has a negative effect on the lubrication performance. Moreover, the lower surface porosity is beneficial to improve the lubrication performance when the total

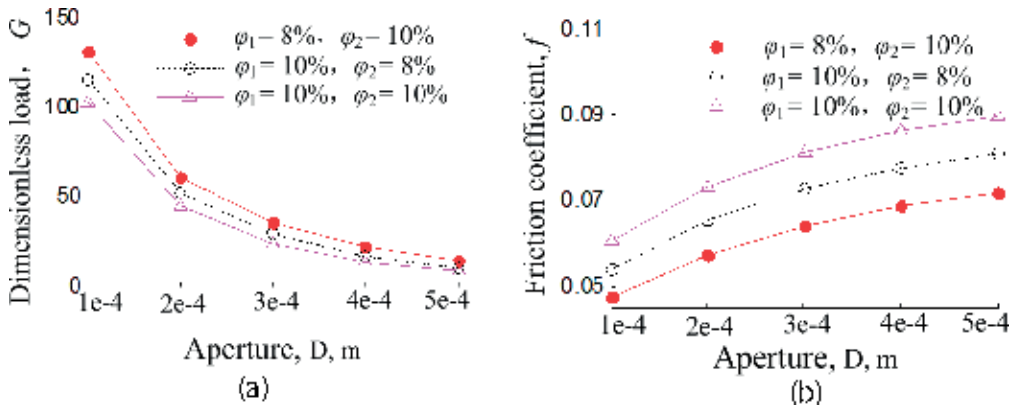

Figure 5. Effect of pore structure on oil slick bear capacity and friction coefficient.

porosities of the bearing are constant. On the one hand, when the total porosities of the bearing are larger, lubricant between the contact surfaces is more likely to seepage into the porous matrix. So that the oil film lubrication performance is poor. On the other hand, when the total porosities of the bearing are constant, the lower surface porosity can prevent the oil leaking into the porous matrix. Therefore the oil will be kept in the contact surfaces and the lubrication performance will be improved.

The Fe-C-Cu-based multi-layer bearing materials were prepared by powder metallurgy method. The wax-based lubricant as a densification agent was added into the surface layer to Increase the density. And an appropriate amount of TiH_2 as a pore-forming agent was added into the bottom layer to increase the oil content properly. The porosities were measured by drainage method. And the porosity of the bottom layer was about 20%, the porosity of surface layer changed within 10–20%. Note that the multi-layer bearing becomes monolayer when the porosities of the two layers are equal.

The tribological properties of the porous samples were tested on a face-to-face contact tribometer under oil lubrication condition. The initial load is 50 N for 10 min as run-in period. And then the load will be added 50 N every 10 min. And the total test time is 30 min. When the experiment tested with sufficient oil supply, the oil bearing materials can work in hydrodynamic lubrication state under the proper speeds and loads. This lubrication state is consistent with the numerical simulation. When the load exceeds a certain limit, the friction coefficient rises sharply. The test machine has a slight noise and vibration, which shows that the oil film cracks. And scratches and adhesion maybe existed in the friction surface. The limit load of the oil film rupture is the load capacity of the oil film.

The results of the friction test are shown in **Figure 6**. As shown in **Figure 6**, the friction coefficients of the multi-layer samples are significantly lower than that of the single layer sample (when the surface porosity is 20%) under the fluid lubrication condition. When the surface porosity is 10%, the friction coefficient of the multilayer material is the smallest. And the friction coefficients gradually increased when the surface porosities changed from 10–20%. The multi-layer materials with dense surface layers have better lubrication property than the single layer materials. The reason is that the dense surface can prevent the oil flow into the

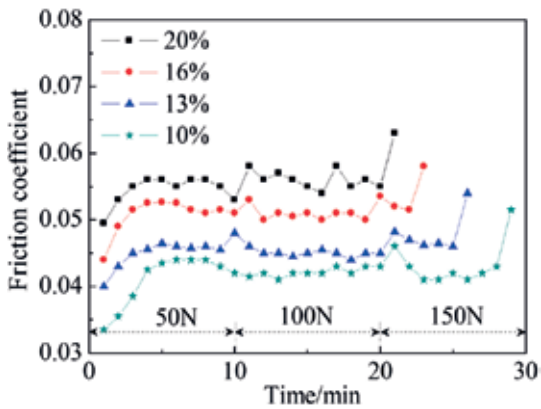

Figure 6. Friction coefficients of samples in variational load under fluid lubrication condition.

porous material, which could ensure a thicker oil film. When the surface layer has a higher porosity, the lubricant is not easy to exist between the friction pairs. So the lubricant is not sufficient. And the lubrication property is poor. In summary, when design the composite sintered material under the condition of fluid lubrication, the low surface porosity can effectively improve the material lubricating property. These experimental results are consistent with the results of the numerical simulation.

4. Conclusions

(1) The lubrication performance of the multi-layer materials is better than that of the single layer materials. Also, it can be significantly improved if considering the surface Darcy flow. Within a certain range, the effects of surface Darcy flow on the lubrication performance are more obviously with higher speed.

(2)The lower permeability surface is beneficial to improve the lubrication property of the multi-layer porous bearing when the total porosity is certain. There is a good agreement between the numerical analysis and the measurement. Therefore, when design the multi-layer oil bearing, the surface porosity should be reduced as far as possible if the oil content is guaranteed. This work is beneficial for the analysis of the tribological property and the structural design of multi-layer bearing.

Acknowledgements

The authors are very grateful for the support of the Natural Science Foundation of China (No. 51575151, No. 50975072), the Anhui Key Scientific and Technological Projects (No. 1501021006). The author also wishes to thank Dr. Li Congmin for his help in translating this paper.

Author details

Yanguo Yin* and Guotao Zhang

*Address all correspondence to: abyin@sina.com

Institute of Tribology, Hefei University of Technology, Hefei, PR China

References

[1] Zhang GT, Yin YG, Li JN. Mint: Tribological properties of lead-free Cu–FeS composites under dry sliding condition. Journal of Materials Research. 2016;**32**:354-362

[2] Zhang GT, Yin YG, Xue L, Zhu GQ, Tian M. Effects of surface roughness and porous structure on the hydrodynamic lubrication of multi-layer oil bearing. Industrial Lubrication and Tribology. 2017;**69**:455-463

[3] Carmeron A, Morgan VT. Critical conditions for hydrodynamic lubrication of porous metal bearings. Proceedings of the Institution of Mechanical Engineers. 1962;**176**:761-770

[4] Zhang G, Yin Y, Liu Z, et al. Lubrication property of multi-layer sintering material under hydrodynamic lubrication. Acta Materiae Compositae Sinica. 2016;**33**:2807-2814

[5] Lin JR, Hwang CC. Lubrication of short porous journal bearings — Use of the Brinkman-extended Darcy model. Wear. 1993;**161**:93-104

[6] Rao PS, Agarwal S. Effect of surface roughness on the hydrodynamic lubrication of porous inclined slider bearing considering slip velocity and squeeze velocity with couple stress fluids. International Journal of Engineering Science and Technology. 2014;**6**:45-64

[7] Chritensen H. Stochastic models for hydrodynamic lubrication of rough surfaces. The Proceedings of the Institution of Mechanical Engineers. 1969;**185**:1013-1026

[8] Prakash J, Tiwari K. Lubrication of a porous bearing with surface corrugations. Journal of Lubrication Technology. 1982;**104**:127-134

[9] Andharia PI, Gupta GL, Deheri GM. Effect of surface roughness on hydrodynamic lubrication of slider bearings. Tribology Transactions. 2001;**44**:291-297

[10] Meurisse MH, Morales G. Reynolds equation, apparent slip, and viscous friction in a three-layered fluid film, engineering. Tribology. 2001;**222**:369-380

[11] Usha R, Naire SA. Thin film on a porous substrate: A two-sided model, dynamics and stability. Chemical Engineering Science. 2013;**89**:72-88

[12] Naduvinamani NB, Patil SB. Numerical solution of finite modified Reynolds equation for couple stress squeeze film lubrication of porous journal bearings. Computers and Structures. 2009;**87**:1287-1295

[13] Rao TVVLN, Rani AMA, Nagarajan T, Hashim FM. Analysis of journal bearing with double-layer porous lubricant film: Influence of surface porous layer configuration. Tribology Transactions. 2013;**56**:841-847

Edited by David W. Johnson

Tribology is an interdisciplinary area that studies the reduction of friction between moving parts combining chemistry, physics and engineering disciplines. Lubricants are typically substances used to reduce friction. This book contains two sections: the first section examines the chemistry of lubricants and additives, while the second section looks at the lubrication of different types of materials.

Published in London, UK

IntechOpen

ISBN 978-1-83881-434-2